INTERFACIAL DYNAMICS OF FERROFLUIDS IN HELE-SHAW CELLS

by

Zongxin Yu

A Dissertation

Submitted to the Faculty of Purdue University

In Partial Fulfillment of the Requirements for the degree of

Doctor of Philosophy

School of Mechanical Engineering

West Lafayette, Indiana

August 2023

THE PURDUE UNIVERSITY GRADUATE SCHOOL
STATEMENT OF COMMITTEE APPROVAL

Dr. Ivan C. Christov, Chair

School of Mechanical Engineering

Dr. Jun Chen

School of Mechanical Engineering

Dr. James M. Gibert

School of Mechanical Engineering

Dr. Steven Dong

Department of Mathematics

Approved by:

Dr. Nicole L. Key

To my parents

ACKNOWLEDGMENTS

First and foremost, I am deeply grateful for the unwavering support, invaluable insights, and infinite patience of my advisor, Dr. Ivan C. Christov. Without his guidance, this thesis would not have reached its completion. I encountered him at a time when I was on the verge of quitting my PhD, but he changed my perspective by showcasing the elegance of mathematics and the genuine passion of a true scientist. Under his mentorship, I have imbibed the principles of rigor and honesty in research, with Dr. Christov serving as an exceptional role model of academic integrity. Through his inspiring story of perseverance, he has taught me the true meaning of the word "persistence." Moreover, Dr. Christov has been a constant source of encouragement, celebrating each of my achievements and bolstering my confidence. Whenever I have faced challenges and moments of hesitation, his support has propelled me forward. Over the past four years of working together, he has trained me into an independent researcher and a resilient individual.

I would also like to thank my committee members, Dr. Jun Chen, Dr. James M. Gibert and Dr. Steven Dong, for being always supportive. Their advice has been very helpful in improving this thesis.

I am immensely grateful for the unconditional love of my parents. Despite their worries and anxieties about my life studying abroad, their concerns have stemmed from a place of deep care and affection. We have had numerous arguments about the future, but I now realize that their words were ultimately conveying their heartfelt "We miss you."

I would like to thank Dr. Prateek Gupta and Dr. Yongkai Chen, who served as both mentors and dear friends, guiding me through the most challenging moments of my PhD journey. Their support helped me navigate through confusion. I would also like to thank Dr. Jixuan Yao, who provided me with the warmest home. Despite the difficulties posed by the Covid period, being her roommate and sister created my happiest time in Purdue. Hanlin Zhang, my undergraduate roommate, may be physically distant in China, but her support and presence have remained steadfast throughout the various challenges I have faced in different stages of life and work.

I am also thankful for being a part of a welcoming and inclusive group at the TMNT-Lab, where I have many friendly and helpful colleagues: Dr. Tanmay C. Shidhore, Dr. Daihui Lu, Dr. Xiaojia Wang, Shrihari Pande, Pranay P. Nagrani, and Jielin Yang.

I must not forget my litter furry friends. Papaya gives me the longest, warmest five-year companies throughout my PhD. Meatball brought me the postdoc offers I desire most. Caicai is sitting on my feet right now, without whom I would have finished my thesis earlier. Doge Melon is my best gift at Purdue, and I am excited, and ready to embrace our bright future. None of them are smart, but I hope they all keep healthy and happy.

My last acknowledgment is made to the U.S. National Science Foundation for support of this research under grant No. CMMI-2029540, as well as the Ross Fellowship and Bilsland Dissertation Fellowship from the Graduate School at Purdue University.

TABLE OF CONTENTS

LIST OF TABLES

LIST OF FIGURES

ABSTRACT

Ferrofluids are remarkable materials composed of magnetic nanoparticles dispersed in a carrier liquid. These suspensions exhibit fluid-like behavior in the absence of a magnetic field, but when exposed to a magnetic field, they can respond and deform into a variety of patterns. This responsive behavior of ferrofluids makes them an excellent material for applications such as drug delivery for targeted therapies and soft robots. In this thesis, we will focus on the interfacial dynamics of ferrofluids in Hele-Shaw cells. The three major objectives of this thesis are: understanding the pattern evolution, unraveling the underlying nonlinear dynamics, and ultimately achieving passive control of ferrofluid interfaces. First, we introduce a novel static magnetic field setup, under which a confined circular ferrofluid droplet will deform and spin steadily like a 'gear', driven by interfacial traveling waves. This study combines sharp-interface numerical simulations with weakly nonlinear theory to explain the wave propagation. Then, to better understand these interfacial traveling waves, we derive a long-wave equation for a ferrofluid thin film subject to an angled magnetic field. Interestingly, the long-wave equation derived, which is a new type of generalized Kuramoto–Sivashinsky equation (KSE), exhibits nonlinear periodic waves as dissipative solitons and reveals fascinating issues about linearly unstable but nonlinearly stable structures, such as transitions between different nonlinear periodic wave states. Next, inspired by the low-dimensional property of the KSE, we simplify the original 2D nonlocal droplet problem using the center manifold method, reducing the shape evolution to an amplitude equation (a single local ODE). We show that the formation of the rotating 'gear' arises from a Hopf bifurcation, which further inspires our work on time-dependent control. By introducing a slowly time-varying magnetic field, we propose strategies to effectively control a ferrofluid droplet's evolution into a targeted shape at a targeted time. The final chapter of this thesis concerns our ongoing research into the interfacial dynamics under the influence of a fast time-varying and rotating magnetic field, which induces a nonsymmetric viscous stress tensor in the ferrofluid, requiring the balance of the angular momentum equation. As a consequence, wave propagation on a ferrofluid interface can be now triggered by magnetic torque. A new thin-film long-wave equation is consistently derived taking magnetic torque into account.

1. INTRODUCTION

1.1 Ferrofluids and applications

Recently, there has been significant interest in the physics of active and responsive fluids [1], [2]. For example, swimming bacteria can take a suspension of microscopic gears out of equilibrium and extract rectified (useful) work out of an otherwise random system [3]. One promising approach to creating active fluids with controllable properties and behaviors is by suspending many mechanical microswimmers made from shape-programmable materials [4] and actuating them with an external magnetic field [5], [6]. This actuation mechanism is particularly enticing for biological applications due to the safe operation of magnetic fields in the medical setting (for, *e.g.*, targeted therapies and drug delivery *in vivo*) [7]. Even simpler than a suspension of magnetically-responsive mechanical microswimmers is a suspension of ferrofluid droplets, which can also respond to an external magnetic field [8], [9]. Ferrofluids are colloidal dispersion of ferromagnetic nanoparticles in a carrier liquid, such as water, which can be immiscible when placed in another liquid. In the absence of a magnetic field, these suspensions behave like Newtonian fluids. However, upon imposing an external magnetic field $\mathbf{H}$, the nanoparticles' magnetic dipoles align with the applied field, and generate a magnetization field $\mathbf{M}$, which further leads into a body force density in the flow, and magnetic normal stress on the interface. These forces can be harnessed for remote manipulation of ferrofluids, offering potential applications a wide range of technological and engineering applications [10]. For instance, the versatility and unique properties of ferrofluids make them a promising candidate for drug delivery systems [11] and mechanical measurement in biological tissues [12], offering potential benefits in the fields of medicine, healthcare, and biological research.

More recently, ferrofluids have also gained attention in the field of soft robotics due to their responsive features. Fan *et al.* [13] report a method to actuate and control ferrofluid droplets as shape-programmable magnetic miniature soft robots, which can navigate in two dimensions through narrow channels. The droplets can also achieve multiple functions, including on-demand splitting and merging for delivering liquid cargo. They can be controlled to split into multiple subdroplets and complete cooperative tasks, such as mixing. Ahmed

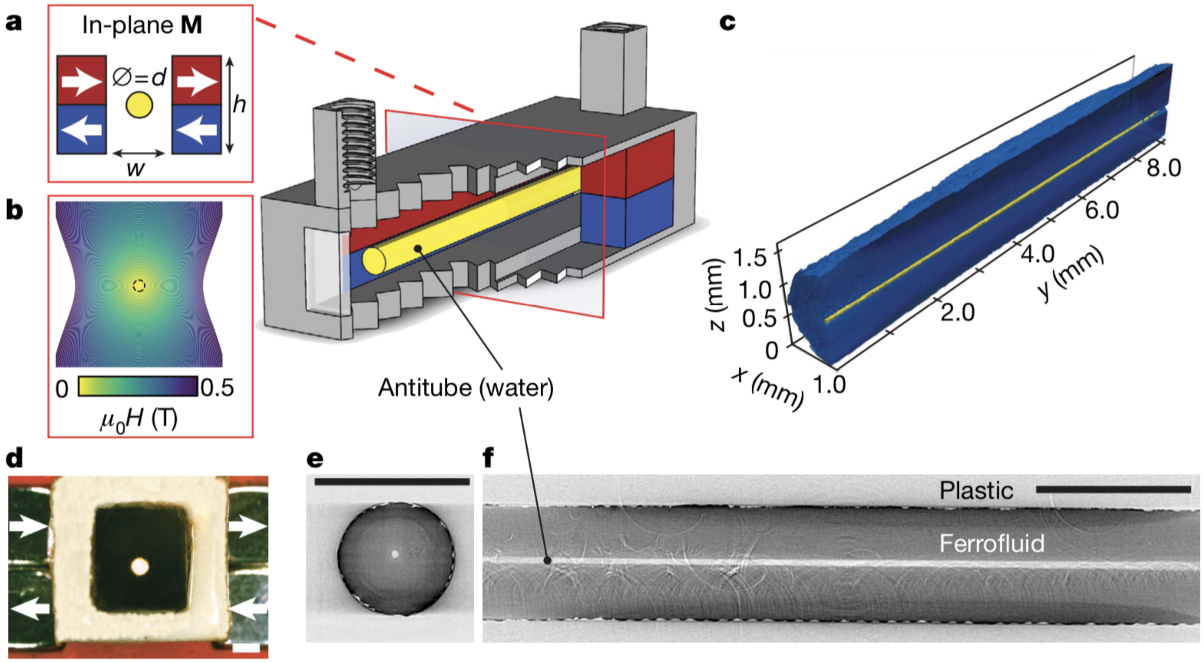

Figure 1.1. Wall-less magnetic confinement in a fluidic channel [15], reprinted from *Nature*, volume 581, P. Dunne, *et al.*, "Liquid flow and control without solid walls," pages 58–62, ©2020, with permission from Springer Nature.

et al. [14] used closed-loop shape control to achieve engulfment of particles, object manipulation, and flow manipulation via ferrofluids. Dunne *et al.* [15] proposed a liquid-in-liquid approach to transport delicate liquids, *i.e.*, human blood with very little damage due to low shear stress of a liquid-walled channel contained in a ferrofluid medium. Specifically, they utilized the interface between an aqueous liquid and an immiscible magnetic liquid as the wall of the channel, as shown in Fig. 1.1. Then, manipulation of the external field provides flow control, such as valving, splitting, merging, and pumping. In these cases, the effective manipulation of ferrofluids offers promising avenues for creating flexible and programmable soft robots adapted to be capable of performing a range of tasks and functions.

However, achieving these technological goals necessitates a deeper theoretical understanding, beyond the scope of recent experiments, to comprehensively reveal the underlying mechanisms governing the behavior of ferrofluids. Furthermore, it is necessary to develop effective control strategies.

1.2 Ferrofluids in Hele-Shaw cells

Immiscible fluid flows confined in Hele-Shaw cells have been investigated extensively during the past several decades [16]. Going back to the classical work by Saffman and Taylor [17], interest has focused on the dynamics of the sharp interface between the fluids [18]. The interface's displacement, when the motion of the fluids is normal to the unperturbed interface (Fig. 1.2(a)), has been of particular interest to most studies, specifically viscous fingering instabilities and finger growth [19]. In contrast, the main flow direction in Hele-Shaw flows is *parallel* to the fluid interface, such as Fig. 1.2(b). This case has received less attention. Early work by Zeybek and Yortsos [20], [21] considered such a parallel flow in a horizontal Hele-Shaw cell, both theoretically and experimentally. They found that, in the limit of large capillary number and under the long-wave assumption, interfacial waves between the two viscous fluids in this setup are governed by a set of coupled Korteweg–de Vries (KdV) and Airy equations. Similarly, Charru and Fabre [22] investigated periodic interfacial waves between two viscous fluid layers in a Couette flow, in which case the long-wave equation was found to be of Kuramoto–Sivashinsky (KS) type. Subsequently, experimental work by Gondret and co-workers [23], [24] demonstrated traveling waves in a parallel flow in a vertical Hele-Shaw cell. In this case, the phenomenon is well-described by a modified Darcy equation accounting for inertial effects, in which context a Kelvin–Helmholtz instability for inviscid fluids was found [25], [26]. These prior studies considered fluids that are not responsive to external stimuli.

When a ferrofluid drop is confined between two closely spaced glass plates, *i.e.*, in a Hele-Shaw cell, and subjected to an external magnetic field, the traditional Saffman–Taylor, viscous fingering instability is modified by magnetic interactions. As a result, the ferrofluid's interface can evolve into a complex structure. The ferrofluid model in a Hele-Shaw cell can be derived by including the magnetic body force density $\mu_0\mathbf{M}\cdot\boldsymbol{\nabla}\mathbf{H}$, so that the confined flow is governed by a modified Darcy's law [27] with gap-averaged velocity given by:

$$\boldsymbol{v} = -\frac{b^2}{12\mu_f}\left(\boldsymbol{\nabla}p - \frac{1}{b}\int_0^b \mu_0\mathbf{M}\cdot\boldsymbol{\nabla}\mathbf{H}\,dz\right), \tag{1.1}$$

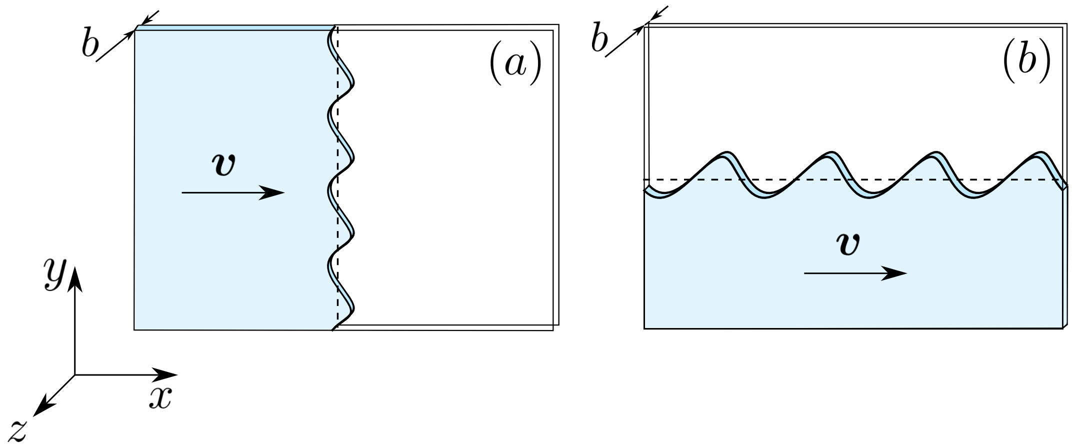

Figure 1.2. Schematic illustration of two types of Hele-Shaw cells (of small gap thickness b) with the main flow direction $\boldsymbol{v}$ being (a) perpendicular and (b) parallel to the unperturbed interface (dashed).

where b is the gap between the two plates, p is the pressure in the ferrofluid, μ_f is the ferrofluid's dynamic viscosity, μ_0 is the free-space permeability. For paramagnetic materials and 'not-too-strong' fields, it is customary to assume a linear magnetization relation [8]:

$$\mathbf{M} = \chi \mathbf{H}, \tag{1.2}$$

where the constant χ is called the magnetic susceptibility. In addition, the magnetic field satisfies the quasistatic Maxwell equations:

$$\boldsymbol{\nabla} \cdot \mathbf{B} = 0, \tag{1.3}$$

$$\boldsymbol{\nabla} \times \mathbf{H} = \mathbf{0}, \tag{1.4}$$

where $\mathbf{B}$ is the magnetic flux given by

$$\mathbf{B} = \mu_0(\mathbf{M} + \mathbf{H}). \tag{1.5}$$

Equations (1.2) and (1.4) allow us to rewrite the magnetic body force as the gradient of a scalar potential $\Psi = \mu_0 \chi |\mathbf{H}|^2/2$, and the gap-averaged velocity (1.1) can also be rewritten as the gradient of a single scalar potential $p - \Psi$:

$$\boldsymbol{v} = -\frac{b^2}{12\mu_f} \boldsymbol{\nabla} (p - \Psi), \tag{1.6}$$

Employing the incompressible condition $\boldsymbol{\nabla} \cdot \boldsymbol{v} = 0$, the governing equation for the flow reduces to Laplace's equation:

$$\nabla^2 (p - \Psi) = 0. \tag{1.7}$$

On the boundary, an application of Gauss's law to Eq. (1.3) yields $\oiint_S \mathbf{B} \cdot d\boldsymbol{S} = 0$ from Eq. (1.3), which requires that the normal component of $\mathbf{B}$ is continuous across the interface. Meanwhile, an application of Green's theorem applied to Eq. (1.4) yields $\oint_l \mathbf{H} \cdot d\boldsymbol{l} = 0$, which requires that the tangential component of $\mathbf{H}$ is continuous across the interface. In other words:

$$[\![\mathbf{B} \cdot \hat{\boldsymbol{n}}]\!] = 0, \tag{1.8a}$$

$$[\![\mathbf{H} \cdot \hat{\boldsymbol{\tau}}]\!] = 0, \tag{1.8b}$$

where $[\![\xi]\!] = \xi_1 - \xi_2$, represents the difference (jump) of a quantity across the interface between the two fluids, while $\hat{\boldsymbol{n}}$ and $\hat{\boldsymbol{\tau}}$ are the normal and tangential unit vectors to the interface, respectively.

The total Cauchy stress $\boldsymbol{T}_{\text{tot}}$ of the ferrofluid can be written as [8]:

$$\boldsymbol{T}_{\text{tot}} = -\underbrace{p\boldsymbol{I}}_{\substack{\text{from hydrodynamic} \\ \text{pressure}}} + \underbrace{\mu_f[\boldsymbol{\nabla}\boldsymbol{v} + (\boldsymbol{\nabla}\boldsymbol{v})^\top]}_{\substack{\text{viscous} \\ \text{stress}}} - \underbrace{\frac{\mu_0 H^2}{2}\boldsymbol{I} + \mathbf{B}\mathbf{H}}_{\substack{\text{magnetic} \\ \text{stress}}}. \tag{1.9}$$

Combining the latter with the continuity conditions from Eq. (1.8b), we have

$$[\![\hat{\boldsymbol{n}} \cdot \boldsymbol{T}_{\text{tot}} \cdot \hat{\boldsymbol{n}}]\!] = -\sigma\kappa \qquad \Rightarrow \qquad p_1 + \frac{\mu_0}{2}(\mathbf{M}_1 \cdot \hat{\boldsymbol{n}})^2 = \sigma\kappa, \tag{1.10}$$

where σ is the surface tension between the fluids, κ is the interface curvature, and we assume $p_2 = 0$, $\mathbf{M}_2 = \mathbf{0}$, so that fluid "2" is nonmagnetic (*e.g.*, air) and fluid "1" is the ferrofluid. The pressure boundary condition in Eq. (1.10) is a modified Young–Laplace law, in which $\mu_0(\mathbf{M}\cdot\hat{\boldsymbol{n}})^2/2$ represents the magnetic normal stress on the interface. This equation, together with the kinematic boundary condition on the normal interface velocity V_n,

$$V_n = -\frac{b^2}{12\mu_f}\boldsymbol{\nabla}\left(p - \Psi\right)\cdot\hat{\boldsymbol{n}}, \tag{1.11}$$

can be used to solve the Laplace Eq. (1.7). In Chapter 2, the vortex-sheet method [28]–[30] is be used to solve this system of equations numerically.

Pattern formation and evolution due to interfacial instability of magnetic fluid interfaces have been investigated intensively [31]–[35]. One remarkable type of pattern emerged from the so-called labyrinthine instability [33]. These highly branched structures are formed when a magnetic fluid drop is confined in a Hele-Shaw cell and subjected to a uniform magnetic field in the direction perpendicular to the Hele-Shaw cell's plates. The different possible configurations and nonuniformity of the magnetic field in this problem have motivated the analysis of a number of pattern formation and stability analyses. For example, the interface of a ferrofluid droplet subject to a radial magnetic field and confined in a Hele-Shaw cell exhibits linear instability and evolves into a stationary starfish-like pattern, as shown analytically in [27], [36]. Interfacial instability of ferrofluid droplets subjected to an azimuthal magnetic field in both rotating [37] and motionless [38] Hele-Shaw cells was also analyzed using weakly nonlinear approximations. Most relevant to the present work, Jackson and Miranda [39] introduced a "crossed" magnetic field (with an azimuthal component and the one perpendicular to the plane) to influence the interfacial mode selection on the interface of a confined ferrofluid drop.

The linear theory of the Kelvin–Helmholtz instability for unconfined ferrofluids was developed by Rosensweig [8]. His work revealed how the strength of the applied magnetic field (in addition to the velocity difference and viscosity contrast between the fluids across the interface) enters the threshold for instability. Miranda and Widom [40] extended this result to a parallel ferrofluid flow in a vertical Hele-Shaw cell under three orientations of the external magnetic field, including tangential and normal to the interface, and perpendicular to the in-plane direction, and deduced that the magnetic field does not affect the propagation speed of waves. Using a perturbative weakly nonlinear analysis, Lira and Miranda [41] further extended the latter analysis by adopting an in-plane tilted magnetic field, showing that the wave speed is sensitive to the inclination angle of the field. Interestingly, this magnetic field configuration was shown to generate nonlinear traveling surface waves on the interface between a ferrofluid and an inviscid, nonmagnetic fluid (such as air).

However, the formulations reviewed in this section are based on the linear magnetization assumption, which enables the magnetic body force density to be written as the gradient of a scalar potential. This assumption fails when the ferrofluid is subjected to a fast-varying time-dependent magnetic field, which will be discussed in Section 1.4. In addition, a model of a two-dimensional ferrofluid thin film subjected to a fast-varying field will be given in Chapter 5.

1.3 Time-dependent interface control in Hele-Shaw cells

The manipulation of the rigid geometry of the Hele-Shaw cell [42], using elastic-walled cells [43], and imposing an electric [44] or magnetic [45] field, are effective strategies for passive control of interface dynamics and stability. Recently, "nonstandard" time-dependent control strategies are also attracting attention [16]. Early theoretical and experimental work by Cardoso and Woods [46] showed that the interfacial instabilities are suppressed if the injection rate in a radial Hele-Shaw flow follows a power law in time. Their idea was refined by Li, Lowengrub, Fontana, *et al.* [47], whose numerical and experimental study manipulated fingering patterns by controlling the injection rate of the less viscous fluid. More recently, Zheng, Kim, and Stone [48] proposed a time-dependent strategy for manipulating the fingering pattern (instability can either be suppressed or a fingering pattern, with a prescribed number of fingers, can be selected and maintained) using a time-varying gap thickness in a lifting Hele-Shaw cell (see also [30]). Meanwhile, Anjos, Zhao, Lowengrub, *et al.* [49] designed control protocols to produce self-similar patterns in electro-osmotic flow by adjusting both the electric current and the flow rate. Similarly, time-varying external forcing is easy to achieve for ferrofluids, without altering the cell geometry. For example, Jackson, Goldstein, and Cebers [34] proposed a simple model using a linearly increasing magnetic field strength to achieve pattern selection.

A universal feature of time-dependent nonlinear dynamical systems is the phenomenon of *bifurcation delay*. Examples include the Eckhaus instability of a stretching spatially periodic pattern [50], [51] and the time-dependent dissipative Swift–Hohenberg model for crown formation during the splashing of a drop onto a liquid film [52]. Finite-time evolution of a dynamic instability is characterized by two instability onset times: (i) the time at which the equilibrium loses its stability, and then (ii) the time at which the solution is repelled from the equilibrium. The nonzero difference between these two times is termed the bifurcation delay. Clearly, this phenomenon is expected to occur for ferrofluid interfaces under time-dependent magnetic fields. However, it has not been discussed previously.

In order to gain insight into dynamical bifurcations exhibited by the governing equations of ferrofluid interfaces, a reduced (approximate) model is needed. For example, a finite-dimensional system of ordinary differential equations (ODEs) can reveal the stable and unstable invariant objects in the phase space, such as steady states and periodic orbits. Canonical examples of how the governing equations (typically, PDEs) can be reduced to finite-dimensional systems of ODEs can be traced back to the development of low-dimensional models of turbulence by Hopf [53] and of atmospheric convection by Lorenz [54]. In a Hele-Shaw cell, the complex behaviors of the droplet's evolution, including symmetry breaking, bistability, and nontrivial transients, were reported by Franco-Gómez, Thompson, Hazel, *et al.* [55]. These dynamics were subsequently investigated theoretically by Keeler, Thompson, Lemoult, *et al.* [56], using a weakly nonlinear analysis in the physical domain, finding that unstable periodic orbits are edge states. Weakly nonlinear analysis can also be applied in the Fourier domain. Such a perturbative, second-order mode-coupling analysis was employed by Miranda and Widom [57] to study the pattern-forming dynamics in a Hele-Shaw cell with fluid injection and then followed by extensive analytical studies of different control strategies (see, *e.g.*, [27], [58], [59]). However, a complete characterization of the dynamics (*i.e.* the stability of the orbits, and the type of bifurcations) is lacking.

1.4 Ferrofluids under fast time-varying fields

In a static magnetic field, the nanoparticles in the ferrofluid tend to align their internal dipole moments in the direction of the field, which is the process of *magnetic relaxation*. The microscopic mechanism underlying the magnetic relaxation is due to either the particle rotation in the carrier liquid or the rotation of the magnetic moments within the particles, characterized by the Brownian τ_B and Néel τ_N relaxation times, respectively. These times are typically on the order of 1 ps to 10 µs [8]. The effective relaxation time τ_{eff} can be defined by considering that both the Brownian and Néel processes act simultaneously:

$$\frac{1}{\tau_{\text{eff}}} = \frac{1}{\tau_B} + \frac{1}{\tau_N} \quad \Rightarrow \quad \tau_{\text{eff}} = \frac{\tau_B \tau_N}{\tau_B + \tau_N}. \tag{1.12}$$

In quasi-equilibrium ferrohydrodynamics, the magnetization field is assumed to instantaneously adjust to changes in the applied magnetic field, so that magnetization relaxation time $\tau = \tau_{\text{eff}}$ is considered to be effectively zero. Then, in this quasi-equilibrium, a linear relationship between the magnetic field and the magnetization is assumed: $\mathbf{M} = \chi \mathbf{H}$. However, the behavior of ferrofluids in alternating and rotating magnetic fields can be vastly different than in direct current fields. When the magnetic field changes on a time scale comparable to τ_{eff}, it will lead to a lag between the magnetization and the applied field such that they are not collinear. If $\mathbf{M} \nparallel \mathbf{H}$, then a body-torque density is generated, given by $\mu_0 \mathbf{M} \times \mathbf{H}$. The existence of body torques results from a nonsymmetric viscous stress tensor, which requires the consideration of the balance of angular momentum equation and further leads to novel flow behaviors, such as the "negative viscosity" phenomenon discussed by Shliomis [60] and Shliomis and Morozov [61] under an alternating magnetic field. Another example is ferrofluid pumping as a function of magnetic field amplitude, frequency, and direction, as discussed by Zahn and Greer [62]. In pipe flows, Krekhov and Shliomis [63] predicted a transition from an initially axial flow to steady swirling, revealing spontaneous core rotation. Even without a time-dependent magnetic field, considerable vorticity in the flow can also cause $\mathbf{M}$ to misalign from $\mathbf{H}$, which gives rise to the magnetic torque. An example in which the latter occurs is cavity flows [64]. The misalignment suppresses the vorticity field in the cav-

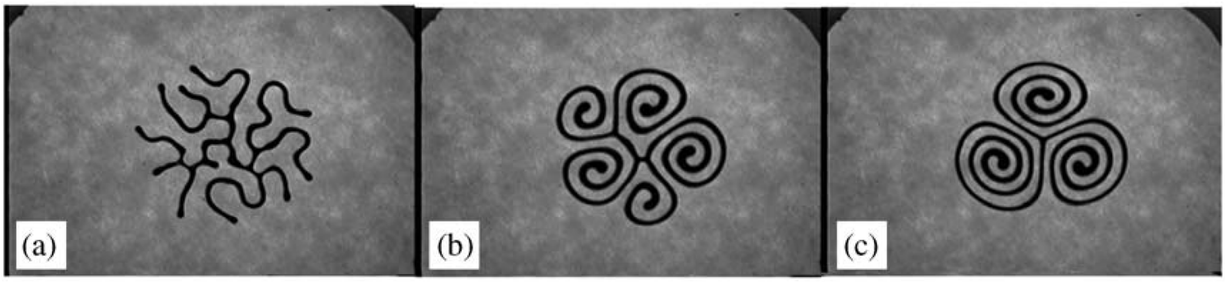

Figure 1.3. Spiral pattern emerging from a labyrinthine instability of a ferrofluid droplet in a Hele-Shaw subjected to an in-plane rotating magnetic field [66], reprinted from *Journal of Magnetism and Magnetic Materials*, volume 289, S. Rhodes, J. Perez, S. Elborai, S.-H. Lee, and M. Zahn, “Ferrofluid spiral formations and continuous-to-discrete phase transitions under simultaneously applied DC axial and AC in-plane rotating magnetic fields,” pages 353–355, ©2005, with permission from Elsevier.

ity and reduces the average shear stress at the boundaries. In a Taylor-–Couette geometry, the effect of the magnetic field frequency modulation on nonlinear ferrofluidic wavy vortex dynamics was investigated via direct numerical simulations in [65], focusing on the resonance phenomena characterized by period doubling and inverse period doubling.

A rotating magnetic field can induce rotation in a stationary fluid, and the earliest study on this spin-up phenomenon can be dated back to 1967 when Moskowitz and Rosensweig [67] reported the relation between the fluid rotation rate as a function of the applied field strength. They were followed by Zaitsev and Shliomis’ theoretical work [68]. While Rosensweig, Popplewell, and Johnston [69] found a connection between the direction of rotation of the fluid and the shape of its free surface and concluded that “surface stress rather than volumetric stress is responsible,” Chaves, Rinaldi, Elborai, *et al.* [70] experimentally showed the existence of bulk flow. The mechanism governing the spin-up flow is still being debated. Recently, Shliomis [71] developed a theory linking the rotation of a free surface layer to the shape of the meniscus and linked the bulk flow with the release of heat in microvortices generated by rotating magnetic particles. Another intriguing phenomenon caused by an in-plane rotating magnetic field is pattern formation on the interface of a ferrofluid droplet confined in a Hele-Shaw cell [66], [72]–[74]. After applying the rotating magnetic field, the labyrinthine pattern, previously formed in response to a normal field, evolves into a spiral pattern as shown in Fig. 1.3. However, a deeper understanding of this interfacial evolution (either from the point of view of theory or simulation) is still lacking.

Despite these complex dynamics observed in experiments, some interfacial models incorporating asymmetric stress have been proposed and investigated in different configurations. Rannacher and Engel [75] found the Rayleigh–Taylor instability of a magnetic fluid superimposed on a less dense nonmagnetic liquid can be suppressed by a uniform magnetic field rotating in the plane of the undisturbed three-dimensional interface. More recently, Soni, Bililign, Magkiriadou, *et al.* [76] incorporated the asymmetric stress into a generalized Navier–Stokes equation and derived a model that can accurately capture the surface waves observed in experimental studies of spinning colloidal magnets. Reynolds, Monteiro, and Ganeshan [77] used the concept of the so-called "odd viscosity," which breaks the symmetry of the stress tensor, to predict how to stabilize the Saffman–Taylor instability of an interface in a Hele-Shaw cell. Kirkinis [78] derived a long-wave thin-film equation and concluded that the magnetic torque can suppress the van-der-Waals-driven thin-film rupture. In this case, the surface torque is approximated as being constant, based on the conclusion of one study focusing on the ferrofluid pumping in a planar duct [62]. Thus, the effect of the surface deformation on the torque is neglected in [78]. While the long-wave equation serves as a powerful model tool for these systems featuring wave propagation, so far none of these long-wave equations have been derived from a consistent scaling, and perturbative reduction, of the governing equations.

1.5 Knowledge gaps and organization of the thesis

Having summarized the basic types of ferrofluid problems that will be considered in this thesis, the knowledge gaps identified by the above literature survey, which will be addressed in different chapters in this report, are as follows:

- Previous work has addressed the linear stability of fluid–fluid interfaces [34], [79], including stationary shapes [59], but not a ferrofluid droplet's fully nonlinear dynamics and controllable rotational motion. We demonstrate, using theory and nonlinear simulation, that it is possible to "grow" linearly unstable ferrofluid interfaces into well-defined permanent shapes. These permanent shapes, which cannot be further deformed without changing the forcing of the system, can then be considered as *solitary waves*, in the sense of a "localized wave that propagates along one space direction only, with undeformed shape" [80, p. 11]. In Chapter 2, we show that the resulting coherent droplet shapes are reproducible and controllable via an external magnetic field. These droplets can be set into rotational motion with velocities predictable by the proposed theory, leading to the possibility of an externally-actuated active fluid suspension.

- In Chapter 2, the investigation of the nonlinear droplet evolution primarily relied on simulations. However, to gain a comprehensive understanding of interfacial waves, it is essential to adopt a wave mechanics perspective. This motivates us to derive a long-wave equation model to approximate the current system, and such a reduced-order model would provide deeper insights into the nonlinear wave dynamics and the underlying mechanisms that sustain them [81]. Despite the recent works and interest on how a tilted magnetic field generates nonlinear waves on a ferrofluid interface, a model long-wave equation, to describe these phenomena is still lacking. Thus, a knowledge gap can be framed by the following research questions: *How can we derive a long-wave equation model to effectively reduce the complexity of the physical system in Chapter 2, while capturing the main physics such as periodic traveling waves? Will these traveling wave solutions exhibit similar wave characters, including stability and propagation speed, as observed in Chapter 2? Will the long-wave equation mathematically explain how the nonlinearity arrests linear instability, as well as shed light on why the system is able to sustain solitary waves?* These questions are addressed in Chapter 3.

- A striking feature of pattern formation in confined ferrofluids, especially near the threshold of linear instability, is the apparent low dimensionality of the dynamics as shown in both Chapters 2 and 3. This observation suggests the possibility of describing the complicated fluid dynamics (in principle, infinite-dimensional) by a finite-dimensional system of ODEs. Enabling such an approximation offers great potential in revealing and characterizing stable and unstable invariant objects within the phase space. Another observation is the similarity between the Hopf bifurcation and the rotating behavior of the droplet described in Chapter 2. In both the Hopf bifurcation and the droplet, the rotation occurs beyond the threshold of linear instability. These intriguing findings prompted us to explore the following questions: *How can we leverage the apparent low dimensionality of the ferrofluid interfacial dynamics to further reduce the problem to a finite set of ODEs? How are these ODEs related to the Hopf bifurcation? Do these features persist under a time-dependent magnetic field? If so, could we utilize techniques from the theory of* dynamic bifurcations *to achieve time-dependent control of magnetic fluid interfaces?* These questions are addressed in Chapter 4.

- While Chapter 4 provides insights into the time-dependent control of ferrofluid interfacial dynamics, its focus is primarily on slowly time-varying magnetic fields, where the linear magnetization assumption remains valid. However, a deeper understanding of the effects of fast time-varying fields, in which case the linear magnetization assumption fails, is necessary, particularly for control applications in the field of soft robotics. Extensive simulations and theoretical work have been conducted on bulk flows of ferrofluids subjected to rotating magnetic fields [67], [68] (such as spin-up flow in cylindrical containers, Couette flow [63], and pipe flow [82]). Despite these efforts, a model for ferrofluid interfacial dynamics that accounts for the phase lag between magnetization and the applied rotating field is still absent. In particular, it is not understood how the resulting nonsymmetric stress tensor and the existence of magnetic torques affect the interfacial dynamics. To address this knowledge gap, several questions must be answered: *How can we derive a simplified model (such as a long-wave equation, as in Chapter 3) that incorporates the effect of magnetic torque (at the continuum level) on the ferrofluid interface? How does a magnetic torque on the interface affect its stability characteristics, compared to the results from Chapter 2? Will the magnetic surface and body torque induce nonlinear wave propagation on the interface as in Chapter 3, or prevent it? If nonlinear waves still exist, are they stable? Do they propagate and interact predictably or is there a possibility of using the magnetic torque* *to drive complex, even chaotic, dynamics as in the traditional KSE?* These questions will be addressed in Chapter 5 of this thesis.

1.6 Parameter tables

Tables 1.1 and 1.2 list, respectively, relevant physical quantities arising in ferrohydrodynamics and certain dimensionless numbers introduced in this thesis.

Table 1.1. The definition of dimensional physical quantities that arise in ferrohydrodynamics.

Variable	Name	SI Unit
ρ	ferrofluid's mass density	kg/m^3
μ_f	ferrofluid's dynamic viscosity	$N\ s/m^2$
$\mathcal{I}$	moment of inertia density	kg/m
σ	surface tension	N/m
μ_b	ferrofluid's bulk viscosity	$N\ s/m^2$
μ_v	ferrofluid's vortex viscosity	$N\ s/m^2$
μ'_f	shear coefficient of spin viscosity	N s
μ'_b	bulk coefficient of spin viscosity	N s
χ	magnetic susceptibility	–
μ_0	free-space permeability	H/m
Ω	magnetic field rotating frequency	1/s
τ	magnetic relaxation time	s
p	hydrodynamic pressure	N/m^2
$\boldsymbol{v}$	translation velocity	m/s
$\boldsymbol{\omega}$	spin velocity	1/s
$\mathbf{H}$	magnetic field density	A/m
$\mathbf{M}$	magnetization	A/m
$\mathbf{B}$	magnetic flux density	T

Table 1.2. The definition of dimensionless quantities.

Dimensionless number	Name
$\mathrm{N_{Br}}$	Magnetic Bond number for radial component field
$\mathrm{N_{Ba}}$	Magnetic Bond number for azimuthal component field
$\mathrm{N_{Bx}}$	Magnetic Bond number for x-component field
$\mathrm{N_{By}}$	Magnetic Bond number for y-component field
$\mathrm{N_{B}}$	Magnetic Bond number for rotating field
Re	Reynolds number
Re_I	Rotational Reynolds number
Sr_M	Magnetization Strouhal number
Ca	Capillary number

2. INTERFACIAL WAVES ON A FERROFLUID DROPLET: ANALYSIS AND SIMULATION

SUMMARY

Two-dimensional free surface flows in Hele-Shaw configurations are a fertile ground for exploring nonlinear physics. Since Saffman and Taylor's work on linear instability of fluid–fluid interfaces, significant effort has been expended to determining the physics and forcing that set the linear growth rate. However, linear stability does not always imply nonlinear stability. We demonstrate how the combination of a radial and an azimuthal external magnetic field can manipulate the interfacial shape of a linearly unstable ferrofluid droplet in a Hele-Shaw configuration. We show that weakly nonlinear theory can be used to tune the initial unstable growth. Then, nonlinearity arrests the instability, and leads to a permanent deformed droplet shape. Specifically, we show that the deformed droplet can be set into motion with a predictable rotation speed, demonstrating nonlinear traveling waves on the fluid-fluid interface. The most linearly unstable wavenumber and the combined strength of the applied external magnetic fields determine the traveling wave shape, which can be asymmetric.

The material in this chapter was published as [Z. Yu, I.C. Christov, "Tuning a magnetic field to generate spinning ferrofluid droplets with controllable speed via nonlinear periodic interfacial waves," *Phys. Rev. E*, vol. 103, art. 013103, 2021] [83] (authors retain rights to reproduce article in a thesis or dissertation). Both authors contributed to the analysis of the problem and the derivation of the mathematical model, which was led by Z.Y. Z.Y. wrote the Python scripts and conducted all the case studies and data analysis. Z.Y. and I.C.C. jointly discussed the results, drafted and revised the manuscript for publication.

2.1 Governing equations

We study the dynamics of an initially circular ferrofluid droplet (radius R) confined in a Hele-Shaw cell with gap thickness b and surrounded by air (negligible viscosity), as shown in Fig. 2.1, because "[i]f any [ferro]fluid mechanics problem is likely to be accessible to theory and to direct comparison of theory and experiment it should be this one" [18]. Both fluids are considered incompressible. We propose to apply the radially-varying external magnetic field

$$\mathbf{H} = \underbrace{\frac{I}{2\pi r}\,\hat{\boldsymbol{e}}_\theta}_{\mathbf{H}_a} + \underbrace{\frac{H_0}{L} r\,\hat{\boldsymbol{e}}_r}_{\mathbf{H}_r}. \tag{2.1}$$

A long wire through the origin, carrying an electric current I, produces the azimuthal component $\mathbf{H}_a$. Anti-Helmholtz coils produce the radial component $\mathbf{H}_r$, where H_0 is a constant and L is a length scale [27], [59]. The combined magnetic field $\mathbf{H} = \mathbf{H}_a + \mathbf{H}_r$ forms an angle with the initially undisturbed interface [58]. The droplet experiences a body force $\propto |\mathbf{M}|\boldsymbol{\nabla}|\mathbf{H}|$, where $\mathbf{M}$ is the magnetization. To study shape dynamics, we assume the ferrofluid is uniformly magnetized, $\mathbf{M} = \chi\mathbf{H}$, where χ is its constant magnetic susceptibility. So, $\boldsymbol{\nabla}|\mathbf{H}| \neq \mathbf{0}$ is the main contribution to the body force, and the demagnetizing field is negligible, as shown in previous work [27], [58], [84], [85].

Enforcing no-slip on the confining boundaries and neglecting inertial terms, the confined flow is governed by a modified Darcy's law [27] with gap-averaged velocity:

$$\boldsymbol{v} = -\frac{b^2}{12\mu_f}\boldsymbol{\nabla}\left(p - \Psi\right), \qquad \boldsymbol{\nabla}\cdot\boldsymbol{v} = 0, \tag{2.2}$$

where p is the pressure in the droplet, μ_f is the ferrofluid's viscosity, $\Psi = \mu_0\chi|\mathbf{H}|^2/2$ is a scalar potential accounting for the magnetic body force, and μ_0 is the free-space permeability. Here, $\mathbf{v}$ is the velocity field of the "inner" ferrofluid, while the viscosity of the "outer" fluid is considered negligible (*i.e.*, it is considered inviscid), so the flow exterior to the droplet is neglected. The resulting model is thus, essentially, a one-phase model.

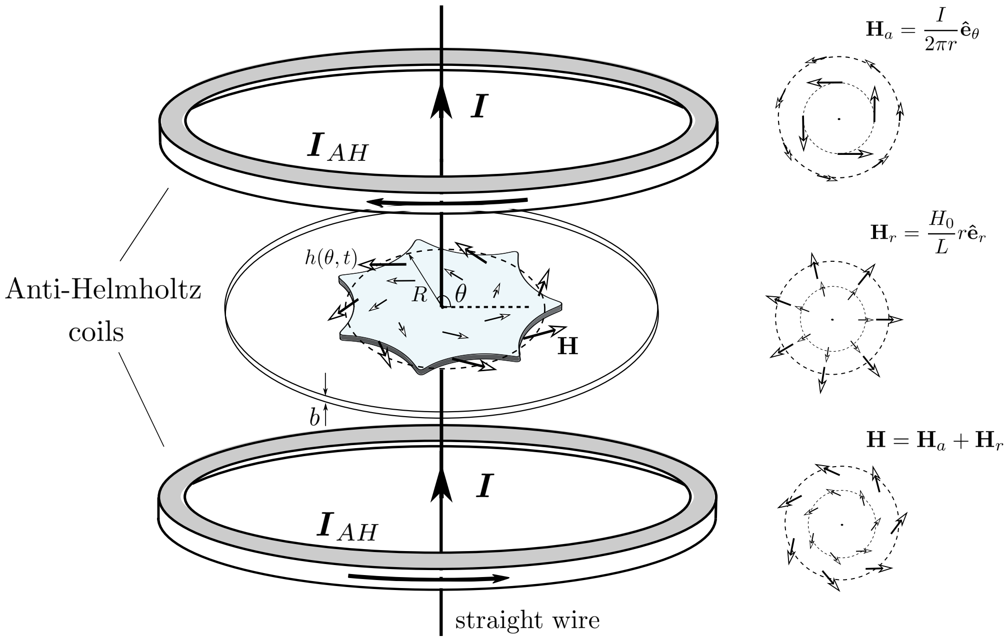

Figure 2.1. Schematic illustration of a Hele-Shaw cell confining a ferrofluid droplet, initially circular with radius R. The azimuthal magnetic field $\mathbf{H}_a$ is produced by a long wire conveying an electric current I. The radial magnetic field $\mathbf{H}_r$ is produced by a pair of anti-Helmholtz coils with equal currents I_{AH} in opposite directions. The combined external magnetic field $\mathbf{H}$ deforms the droplet, and its interface is given by $h(\theta, t)$. In comparison, the fluid exterior to the droplet (*e.g.*, air) is assumed to have negligible viscosity and velocity.

At the boundary of the droplet, the pressure is given by a modified Young–Laplace law [8], [9]:

$$p = \sigma\kappa - \frac{\mu_0}{2}(\mathbf{M} \cdot \hat{\boldsymbol{n}})^2, \tag{2.3}$$

where σ is the constant surface tension, and κ is the curvature of the droplet shape, given by

$$\kappa = \frac{h^2 + 2h_\theta^2 - h_{\theta\theta}h}{(h^2 + h_\theta^2)^{3/2}}. \tag{2.4}$$

The second term on the right-hand side of Eq. (2.3) is the magnetic normal traction [8], [9], where

$$\hat{\boldsymbol{n}} = \frac{h}{\sqrt{h^2 + h_\theta^2}}\hat{\boldsymbol{e}}_r - \frac{h_\theta}{\sqrt{h^2 + h_\theta^2}}\hat{\boldsymbol{e}}_\theta \tag{2.5}$$

denotes the outward unit normal vector at the interface. This contribution breaks the symmetry of the initial droplet interface, due to the projection of $\mathbf{M}$ onto $\hat{\boldsymbol{n}}$, and causes the droplet to rotate. The kinematic boundary condition

$$V_n = -\frac{b^2}{12\mu_f}\boldsymbol{\nabla}\left(p - \Psi\right) \cdot \hat{\boldsymbol{n}} \tag{2.6}$$

requires that the droplet boundary is a material surface.

2.2 Weakly nonlinear analysis

2.2.1 Formulation

We employ the weakly nonlinear approach [57] previously adapted to ferrofluid interfacial dynamics (*e.g.*, [27], [58], [59]). The droplet interface is written as $h(\theta, t) = R + \eta(\theta, t)$, where

$$\eta(\theta, t) = \sum_{k=-\infty}^{+\infty} \eta_k(t) e^{ik\theta} \tag{2.7}$$

represents the perturbation of the initially circular interface, with complex Fourier amplitudes $\eta_k(t) \in \mathbb{C}$ and azimuthal wavenumbers $k \in \mathbb{Z}$. The velocity potential $\phi = p - \Psi$ is then expanded into a Fourier series as

$$\phi(r, \theta, t) = \sum_{k \neq 0} \phi_k(t) \left(\frac{r}{R}\right)^{|k|} e^{ik\theta}. \tag{2.8}$$

In polar coordinates (r, θ), the kinematic boundary condition can be written as

$$h_t = -(\phi_r)_{r=h} + \left(\frac{1}{r^2}\phi_\theta h_\theta\right)_{r=h}, \tag{2.9}$$

which can be expanded to second order in η and then Fourier transform gives η_k that can be related with ϕ_k as:

$$\phi_k(t) = -\frac{R}{|k|}\dot{\eta}_k + \sum_{k' \neq 0} \left(\operatorname{sgn}(kk') - \frac{1}{|k|}\right) \dot{\eta}_{k'}' \eta_{k-k'}, \tag{2.10}$$

where $\mathrm{sgn}(x) = x/|x|$ for $x \neq 0$ and $\mathrm{sgn}(0) = 0$. Substituting Eqs. (2.10) into (2.3), to replace the velocity potential ϕ with perturbation η and $\dot{\eta}$, keeping only terms up to second order in η, we find the dimensionless equations of motion ($k \neq 0$):

$$\dot{\eta}_k = \Lambda(k)\eta_k + \sum_{k'\neq 0} F(k,k')\eta_{k'}\eta_{k-k'} + G(k,k')\dot{\eta}_{k'}\eta_{k-k'}. \tag{2.11}$$

The mode-coupling functions in Eq. (2.11) are given by

$$\begin{aligned} F(k,k') = \frac{|k|}{R}\Bigg\{ &\frac{\mathrm{N_{Ba}}}{R^4}[3-\chi k'(k-k')] + \mathrm{N_{Br}}\{1+\chi[k'(k-k')+1]\} \\ &- \frac{1}{R^3}\left[1 - \frac{k'}{2}(3k'+k)\right] + \frac{2\chi\sqrt{\mathrm{N_{Ba}N_{Br}}}}{R^2}ik'\Bigg\}, \end{aligned} \tag{2.12a}$$

$$G(k,k') = \frac{1}{R}[(\mathrm{sgn}(kk')-1)|k|-1]. \tag{2.12b}$$

From mass conservation, $\eta_0 = -\sum_{k>0}|\eta_k|^2/R \ \forall t \geq 0$. Here,

$$\Lambda(k) = \underbrace{\frac{|k|}{R^3}(1-k^2)}_{\text{surface tension}} - \frac{2\mathrm{N_{Ba}}}{R^4}|k| + 2(1+\chi)\mathrm{N_{Br}}|k| - \frac{2\chi\sqrt{\mathrm{N_{Ba}N_{Br}}}}{R^2}ik|k| \tag{2.13}$$

denotes the (complex) linear growth rate, and

$$\mathrm{N_{Ba}} = \frac{\mu_0\chi I^2}{8\pi^2\sigma L}, \qquad \mathrm{N_{Br}} = \frac{\mu_0\chi H_0^2 L}{2\sigma} \tag{2.14}$$

are the magnetic Bond numbers quantifying the ratio of azimuthal and radial magnetic forces to the capillary force, respectively. Terms multiplied by χ arise from the magnetic normal stress. The time and length scales used in the nondimensionalization are $12\mu_f L^3/\sigma b^2$ and L, respectively.

2.2.2 Linear regime

First, consider Eq. (2.11), neglecting quadratic terms in η_k, then $\mathrm{Re}\,[\Lambda(k)] = \lambda(k)$ governs the exponential growth or decay of infinitesimal perturbations. For $\lambda(k) > 0$, the interface is unstable. Specifically, Eq. (2.13) indicates that the radial magnetic field term $\propto (1+\chi)\mathrm{N_{Br}}$ is destabilizing, while the azimuthal term $\propto \mathrm{N_{Ba}}$ and surface tension are stabilizing. The most unstable mode k_m solves $d\lambda(k)/dk = 0$:

$$k_m = \sqrt{\frac{1}{3}\left[1 - \frac{2\mathrm{N_{Ba}}}{R} + 2(1+\chi)\mathrm{N_{Br}}R^3\right]}. \tag{2.15}$$

This wavenumber characterizes the dominant $\lfloor k_m \rfloor$-fold symmetry of a pattern. Note that the normal stress from the azimuthal magnetic field does not contribute to the linear dynamics.

The phase velocity of each mode,

$$v_p = -\operatorname{Im}[\Lambda(k)]/k = 2\chi\sqrt{\mathrm{N_{Ba}}\mathrm{N_{Br}}}k/R^2 \tag{2.16}$$

in the linear regime, is set by $\operatorname{Im}[\Lambda(k)]$. A periodic shape on $[0, 2\pi]$ forms a closed curve, meaning wave propagation is manifested as rotation of the droplet. Motion is caused by the magnetic normal stresses arising from the combined magnetic field. Intuitively, from vector projection, we observe that only the combined azimuthal and radial magnetic field can break the symmetry and cause a force imbalance leading to motion. This linear analysis indicates that perturbations of the droplet interface can propagate (and, since $v_p = v_p(k)$, they also experience dispersion). Such wavepackets will either decay or blow-up exponentially according to the sign of $\lambda(k)$. However, this is not the whole story, and *nonlinearly stable* traveling shapes exist, as we now show.

2.2.3 Nonlinear regime

To demonstrate the possibility of nonlinear traveling waves in this system, we numerically solve the weakly nonlinear mode-coupling equations (2.11) for five modes (*i.e.*, $k, 2k, \ldots, 5k$). The fundamental mode $k = 7$ is chosen to allow propagating solutions over a wider swath of the $(\mathrm{N_{Ba}}, \mathrm{N_{Br}}, k_m)$ space (compared to choosing $k < 7$), while only requiring modest spatial resolution for simulations (compared to $k > 7$). We verified that the amplitudes $|c_n|$ and phases $\angle[c_n]$ of modes saturate at late times, leading to permanent propagating profiles with $\eta_{nk}(t) = c_n e^{in\omega(k)t}$ (see below).

2.3 Vortex-sheet Lagrangian numerical method

2.3.1 Formulation

Next, we perform fully nonlinear simulations to validate the weakly nonlinear predictions. The vortex sheet method is a standard sharp-interface technique for simulating dynamics of Hele-Shaw flows [86]. It is based on a boundary integral formulation in which the interface is formally replaced by a generalized vortex sheet [28], as shown in Fig. 2.2, with a distribution of vortex strengths $\gamma(s,t) = (\boldsymbol{v}_1 - \boldsymbol{v}_2)\cdot\hat{\boldsymbol{s}}$, where s is the arclength coordinate. We adapt this approach to handle ferrofluids under imposed magnetic fields. First, we express the velocity of the interface solely in terms of the interface position. To do so, it is convenient to identify the position vector in $\mathbb{R}^2$ with a scalar $z(s,t) \in \mathbb{C}$ (* denotes complex conjugate) [28]–[30]. Second, to advance the interface, we solve the dimensionless equations

$$z_t^* = -\frac{\gamma}{2z_s} + \frac{1}{2\pi i}\mathcal{P}\oint \frac{\gamma(s',t)}{z(s,t)-z(s',t)}ds', \tag{2.17a}$$

$$\frac{\gamma}{2} = \mathrm{Re}\left\{\frac{z_s}{2\pi i}\mathcal{P}\oint \frac{\gamma(s',t)}{z(s,t)-z(s',t)}ds'\right\} + \Big[\kappa(s,t) - (\mathbf{M}\cdot\hat{\boldsymbol{n}})^2 - \Psi\Big]_s, \tag{2.17b}$$

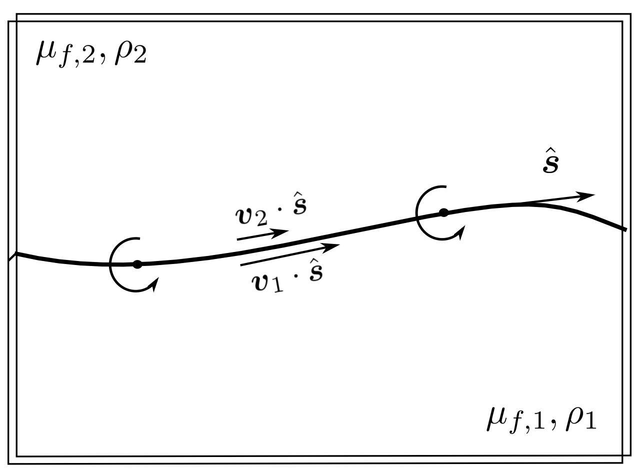

Figure 2.2. Schematic of a vortex-sheet representation of a fluid–fluid interface.

iteratively for the velocity z_t, where $(\cdot)_t \equiv \partial(\cdot)/\partial t$, $(\cdot)_s \equiv \partial(\cdot)/\partial s$, $i = \sqrt{-1}$, and $\mathcal{P}$ represents principal value integration. Here,

$$\Psi = \mathrm{N_{Ba}} r^{-2} + \mathrm{N_{Br}} r^2, \quad \text{and} \quad (\mathbf{M} \cdot \hat{\boldsymbol{n}})^2 = \chi \left[\sqrt{\mathrm{N_{Ba}}} r^{-1} (\hat{\boldsymbol{e}}_\theta \cdot \hat{\boldsymbol{n}}) + \sqrt{\mathrm{N_{Br}}} r (\hat{\boldsymbol{e}}_r \cdot \hat{\boldsymbol{n}}) \right]^2 \tag{2.18}$$

are the dimensionless magnetic scalar potential and normal stress.

The principal value integration in Eqs. (2.17) is performed numerically by a spectrally accurate spatial scheme [29]:

$$PV_j = \frac{2\Delta s}{2\pi i} \sum_{j+k \text{ odd}} \frac{\gamma_k}{z_j - z_k}, \tag{2.19}$$

where a j subscript denotes the evaluation of a quantity at the jth Lagrangian grid point $j\Delta s$ with $\Delta s = L/N$, $L = \oint ds$, and N is the number of grid points. The parametrization of the interface via its arclength reduces the stiffness of the numerical problem caused by the presence of third-order spatial derivatives. A rearrangement of the grid points is conducted with cubic interpolation, after each time step, to maintain uniform grid spacing Δs. The uniform arclength spacing then allows the use of the second-order central differentiation formulæ for all derivatives. A fixed-point iteration scheme is used to resolve the implicit Eq. (2.17b) to obtain γ_j at each interface point z_j, as shown schematically in Fig. 2.3. In current study, the spatial discretization is implemented on an array of Lagrangian points ($N = 1024$) with uniform Δs.

Time advancement (superscripts denote the time step number) is accomplished with a Crank–Nicolson scheme:

$$z^{*n+1} = z^{*n} - \frac{\Delta t}{2} \left[\frac{\gamma^{n+1}}{2z_s^{n+1}} + \frac{\gamma^n}{2z_s^n} \right] + \frac{\Delta t}{2} \left[PV^{n+1} + PV^n \right], \tag{2.20}$$

where both of the nonlinear terms $\gamma^{n+1}/2z_s^{n+1}$ and PV^{n+1} are obtained by subiteration with index m, as shown schematically in Fig. 2.3. Equation (2.20) converges and $z^{n+1} = z^{m+1}$ when $\|z^{m+1} - z^m\| < \mathrm{tol}_z$ with $\mathrm{tol}_z = 0.1 \max|z_t^n| \Delta t$.

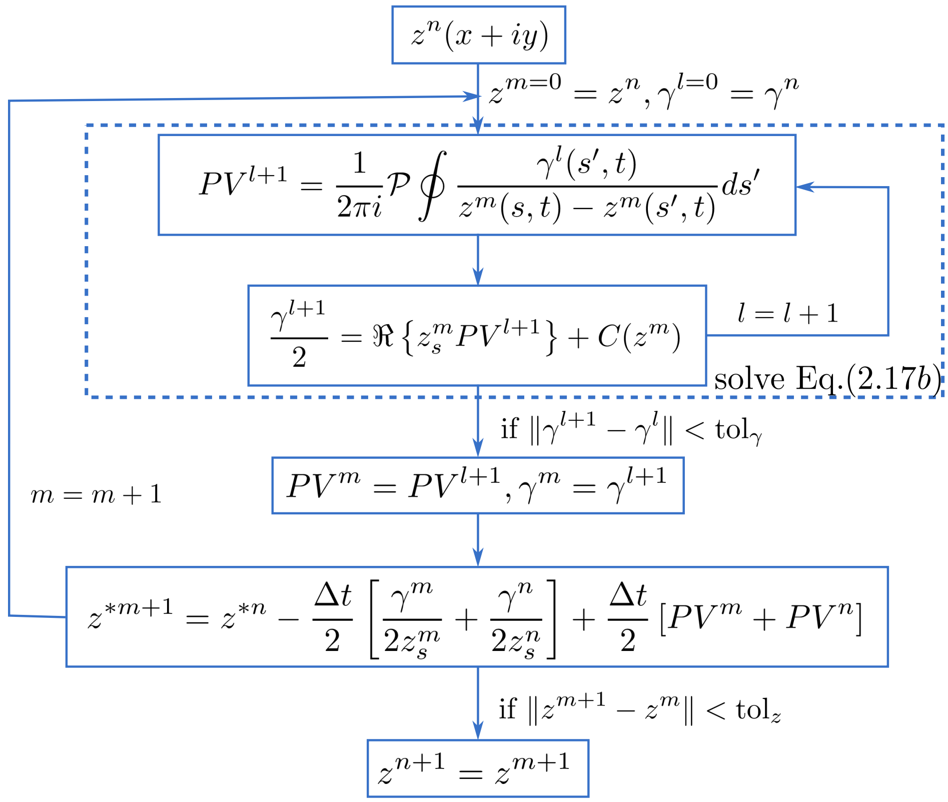

Figure 2.3. Flow chart of the vortex-sheet algorithm using Crank–Nicolson for time advancement and fixed-point iteration for resolving the implicit non-linear terms.

2.3.2 Grid convergence study

A grid convergence study with 4 levels of the grid resolution was conducted for two cases: $k_m = 7$ and $k_m = 9$ with $\mathrm{N_{Ba}} = 1$. The most frequently used case is $k_m = 7$, while the sharper peaks for $k_m = 9$ demand on the highest grid resolution. Figure 2.4(a) shows the spectral energy content of harmonic modes (k, $2k$, $3k$, $\ldots$) of the propagating waveform, where the "piling up" near the tail on the finest grid ($N = 2048$) is numerical noise. This plot supports our decision to consider the $N = 1024$ grid as offering sufficient resolution. Figure 2.4(b) shows the root-mean-squared error in the shape z itself, taking $\hat{z}$ as the "reference shape" on the $N = 2048$ grid. The error decreases with grid refinement. The error at $N = 256$ for $k_m = 9$ is not shown for the propagating shape because the scheme is not even stable on such a coarse mesh for this case.

Figure 2.4 further shows the evolution of (c) the skewness Sk and (d) the asymmetry As. The skewness matches well on all grids used, showing it is a well-converged quantity, while the asymmetry is seen to be more sensitive to the grid resolution. The differences between $N = 1024$ and $N = 2048$ are small enough so that it is safe to use $N = 1024$ for the simulations in this study, considering the significantly higher computational cost incurred by using finer grids.

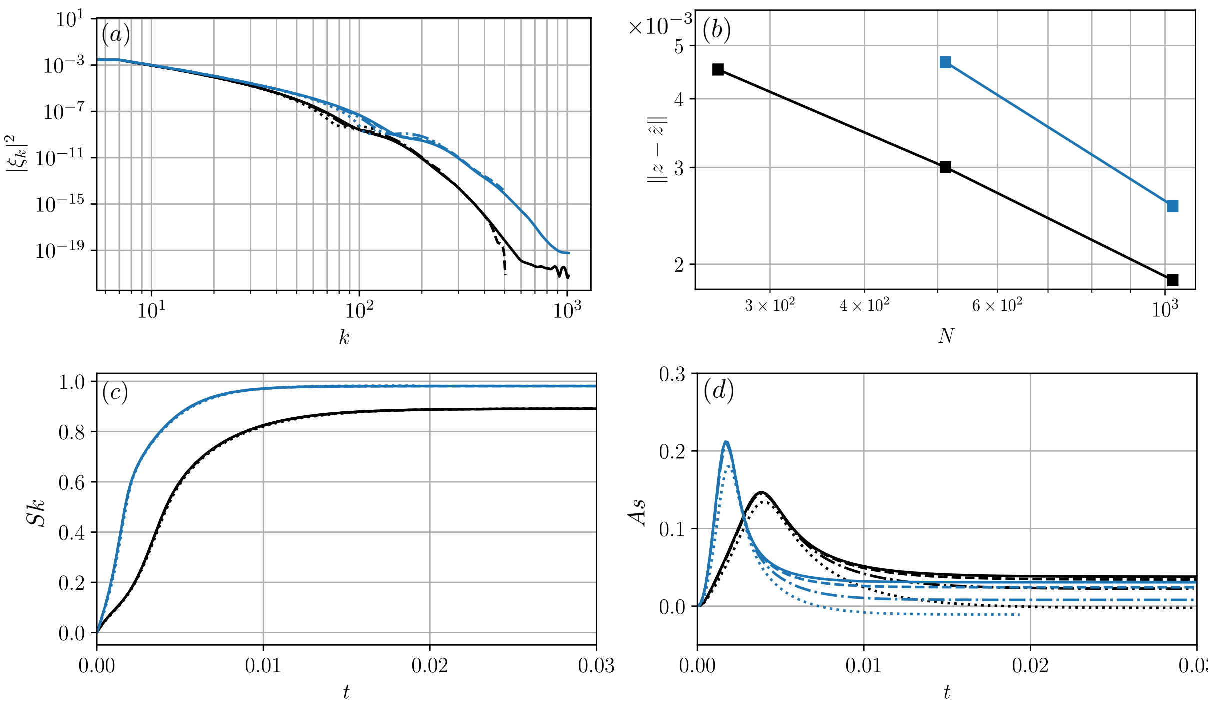

Figure 2.4. Grid convergence study for fundamental modes $k_m = 7$ (black) and $k_m = 9$ (blue) with $\mathrm{N_{Ba}} = 1$ and $N = 256$ (dotted), $N = 512$ (dot-dashed), $N = 1024$ (dashed), and $N = 2048$ (solid). (a) Spectral energy of harmonic modes (k, $2k$, $3k$, $\ldots$). (b) The root-mean-square error taking the $N = 2048$ solution $\hat{z}$ as "exact". (c) Grid convergence of the evolution of the skewness $Sk(t)$. (d) Grid convergence of the evolution of the asymmetry $As(t)$.

2.4 Evolutionary dynamics

The evolution of perturbed harmonic modes η_k under the fully nonlinear simulation and the weakly nonlinear approximation are shown in Fig. 2.5(a). Starting from small initial values ($\eta_k|_{k=7}$= 0.002, $\eta_{nk} = 0$ for $n > 1$) with $\mathrm{N_{Ba}}, \mathrm{N_{Br}}, R, \chi$ set so that the most unstable mode is equal to the fundamental mode ($k_m = k = 7$), they saturate at late times. The perturbed circular interface grows exponentially in the linear regime and then matches the weakly nonlinear approximation at intermediate times ($t \in [0, t_w]$). The nonlinear simulations take longer to saturate ($t \in [t_w, t_e]$) and do so at higher final amplitudes compared to the weakly nonlinear result. The time-domain evolution is also shown in Fig. 2.5(b), evolving from a nearly flat (unwound circular) interface into a permanent propagating profile.

The rotating droplet, shown in Fig. 2.5(c), has a polygonal shape with the symmetry set by the fundamental mode, $k = 7$. The fully nonlinear profile has a sharper peak compared to the weakly nonlinear approximation, which is otherwise in good agreement. The key discovery of the present work is the *stable rotating shape*, which we now seek to analyze as a nonlinear wave phenomenon [80].

2.4.1 Stability diagram based on the first two harmonic modes

A deficiency of linear and weakly nonlinear analyses is that they do *not* provide sufficient conditions for stability. Linearly stable base states can be nonlinearly unstable [87], and *vice versa*. Importantly, however, our nonlinear traveling wave solution is a local *attractor* (following the terminology from [47]); see Fig. 2.5(d).

Shapes in a neighborhood of the propagating profile, subject to small ($\eta_{k,2k}/\eta^f_{k,2k} \ll 1$) or intermediate ($\eta_{k,2k}/\eta^f_{k,2k} = \mathcal{O}(1)$) initial perturbations, converge to it. Larger perturbations (shaded region) lead to *nonlinear* instability of the weakly nonlinearly stable profiles; "fingers" continue to rotate and grow without bound under the effect of the radial magnetic field $\propto \mathrm{N_{Br}}$, which increases with distance to the center of the droplet. Convergence to the attractor is sensitive to the initial amplitude of the first harmonic mode η_k. For the chosen parameters, $\lambda(k) > 0$ and $\lambda(2k) < 0$: high wavenumbers decay and the fundamental wavenumber grow in the linear stage. Consequently, for low η_k/η^f_k and high η_{2k}/η^f_{2k}, the low wavenumber modes grow and saturate, as high wavenumber modes decay exponentially in the linear regime. With higher initial η_k/η^f_k, the perturbed droplet will not go through the linear regime, and the amplitudes of both modes will rapidly increase to create a skewed shape, with multivalued $h(\theta, t)$, for which harmonic modes can no longer be defined. Note

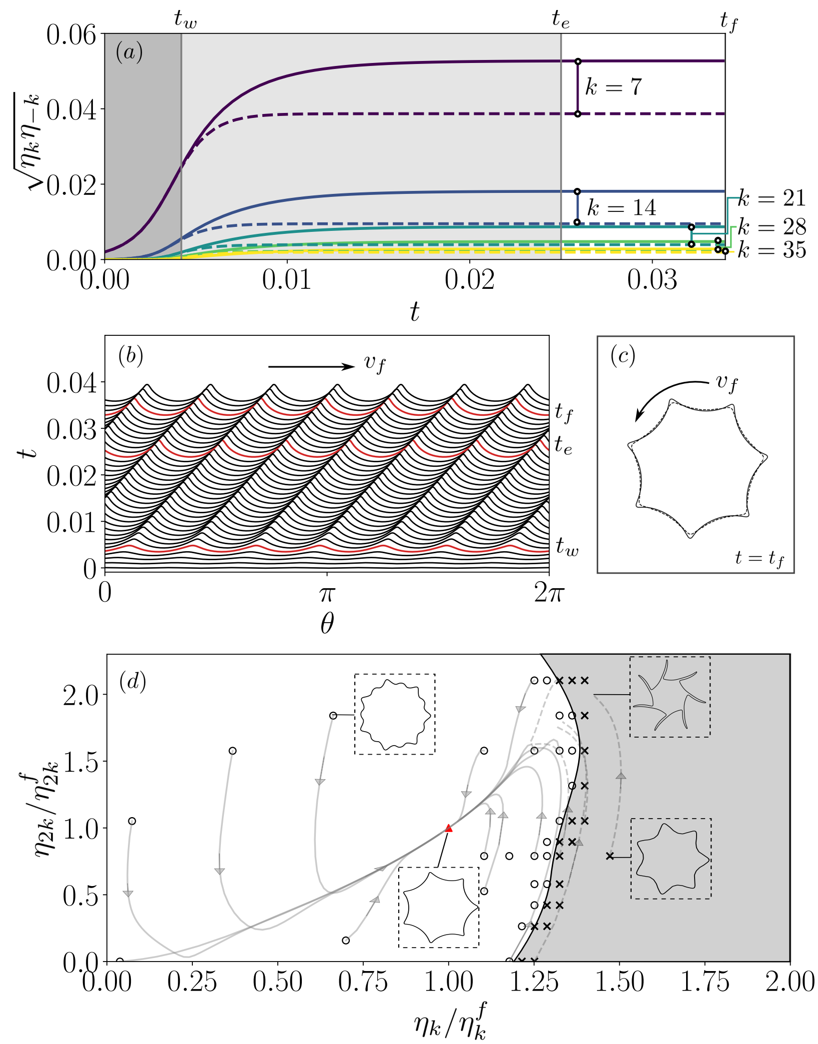

Figure 2.5. (a) The evolution of the first 5 harmonic modes from fully nonlinear simulation (solid) and weakly nonlinear approximation (dashed), for $\mathrm{N_{Ba}} = 1.0$, $\mathrm{N_{Br}} = 37$, $R = 1$, and $\chi = 1$ (same parameters for (b), (c) and (d)). (b) The fully nonlinear evolution of the interface from a small perturbation of the flat base state into a permanent traveling wave (rotating droplet). (c) Comparison between the final shape from fully nonlinear simulation (solid) and weakly nonlinear approximation (dashed); (d) Stability diagram based on the first two harmonic modes of the final shape (marked with ▲) shown in (b); ∘ (resp. ×) denotes the stable (resp. unstable) initial conditions, solid (resp. dashed) curves tract the stable (resp. unstable) evolution trajectories. The unstable region is shaded, and the 'f' superscript represents the final harmonic mode amplitude.

that Fig. 2.5(d) is a projection in the (η_k, η_{2k}) plane, where the initial values of η_{3k}, η_{4k}, η_{5k} are set as the final amplitudes (and phases) from the weakly nonlinear equations. A fast Fourier transform was used to decompose the nonlinear profile into normal modes that we plot in this figure. Note that even though Fig. 2.5(a) indicates η_{3k} makes a non-trivial contribution to the final shape, while η_{4k}, η_{5k} play a smaller role, the projection is sufficient to conclude that the propagating wave profile is an attractor.

2.4.2 Propagation velocity

A permanent traveling wave profile takes the form $\eta(x,t) = \Theta(kx - \omega t)$, where $v_f = \omega/k$ is its propagation (phase) velocity. The modes' complex amplitudes can be expressed as $\eta_k(t) = c_k e^{-i\omega(k)t}$, with constant $c_k \in \mathbb{C}$ accounting for their relative phases. A nonlinear traveling wave profile would consist of a fundamental mode k_f and its harmonics nk_f ($n \in \mathbb{Z}^+$), with $\omega(nk_f) = n\omega(k_f)$, so that the phase velocity can be evaluated as $v_p(nk_f, t) = n\omega(k_f)/nk_f = v_f$. The average v_p of the first five harmonics is used to calculate v_f^N for the nonlinear simulation.

The Fourier modes comprising the nonlinear traveling wave profile are given by $\eta_{nk}(t) = c_n e^{-in\omega(k)t}$, with constant $c_n \in \mathbb{C}$ that account for their relative phases. The phase $\psi(t;k) = \angle\eta_{nk} = \angle c_n - n\omega(k)t$ can be computed trough a Fourier transform, as shown in Fig. 2.6(a). Its rate of change, $-d\psi/dt = n\omega(k)$, is shown in Fig. 2.6(b). The phase velocity $v_p = n\omega(k)/nk$ becomes independent of k when the permanent traveling wave solution is attained upon nonlinear saturation of the unstable small-perturbation initial condition. In other words, all modes propagate at the same velocity, as shown in Fig. 2.6(c), in the final state. The mean final phase velocities of first five harmonics are used to evaluate the propagation velocity as $v_f = \frac{1}{5}\sum_{n=1}^{5} v_p(nk)$. Note that this approach can only be applied for the permanent traveling wave solution; the initial transition time period in Fig. 2.6 (before the permanent profile is attained) is a meaningless transient.

Meanwhile, $v_f^L = v_p$ as given by Eq. (2.16).For a quantitative comparison, three sets of parameters are considered, fixing $\chi = 1$. Two sets (i) and (ii) are for $k_m = 7$, and the variation of $\mathrm{N_{Br}}$ is according to Eq. (2.15). A third set (iii) explores the effect of k_m under the same linear propagation velocity v_f^L. Figure 2.7(a) compares the final propagating velocity predictions. Both v_f^L and v_f^W are in relatively good agreement with v_f^F for small velocities.

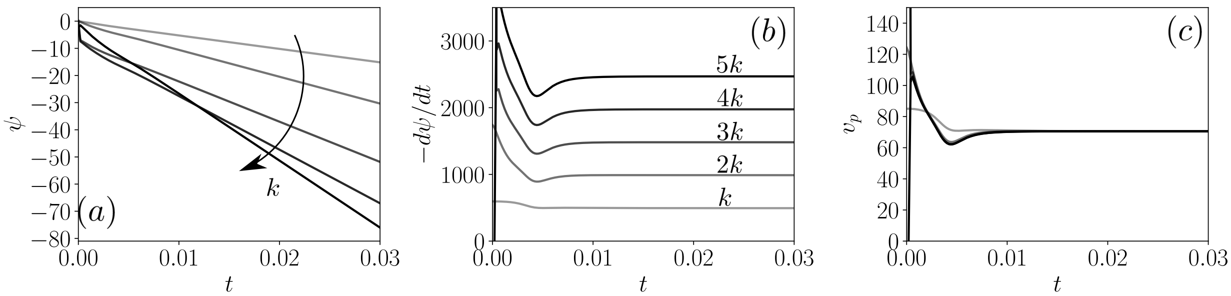

Figure 2.6. (a) Evolution of the modes' phases computed via a Fourier transform. (b) The time-rate-of-change of the phases. (c) Evolution of the phase velocities of the first five harmonic modes.

When $\mathrm{N_{Ba}} \to 0$ (the magnetic field becomes radial), only a stationary (non-rotating) droplet ($v_f = 0$) exists [59]. For higher v_f, the larger deviation in the predictions highlights the importance of nonlinearity. Nevertheless, the linear and weakly nonlinear results follow a similar trend. Importantly, v_f^L and v_f^W help identify the key control factors: the coupled magnetic field strength $\sqrt{\mathrm{N_{Ba}N_{Br}}}$ and the radius of the initial droplet R. The salient physics uncovered is that the propagating velocity can be non-invasively tuned.

2.4.3 Traveling wave shape

The most unstable mode k_m sets the propagating profile, which has a sharper peak for higher k_m [Fig. 2.7(c)]. To quantify the shape change, we introduce the skewness

$$Sk(t) = \frac{\langle \eta^3 \rangle}{\langle \eta^2 \rangle^{3/2}}, \tag{2.21}$$

which is used to define the vertical asymmetry of nonlinear surface water waves [88], [89]; $Sk > 0$ corresponds to narrow crests and flat troughs. Here, $\langle \cdot \rangle = \frac{1}{2}\pi \int_0^{2\pi} (\,\cdot\,)\, d\theta$. Figure 2.7($b$) shows that Sk (for the fully nonlinear propagation) increases with k_m, as expected from the sharper peaks in Fig. 2.7(c). This observation also explains why v_f^L becomes a worse approximation of v_f^F as k_m increases [inset of Fig. 2.7(a)]: smoother peaks (lower k_m) are better captured by the linear theory based on harmonic modes.

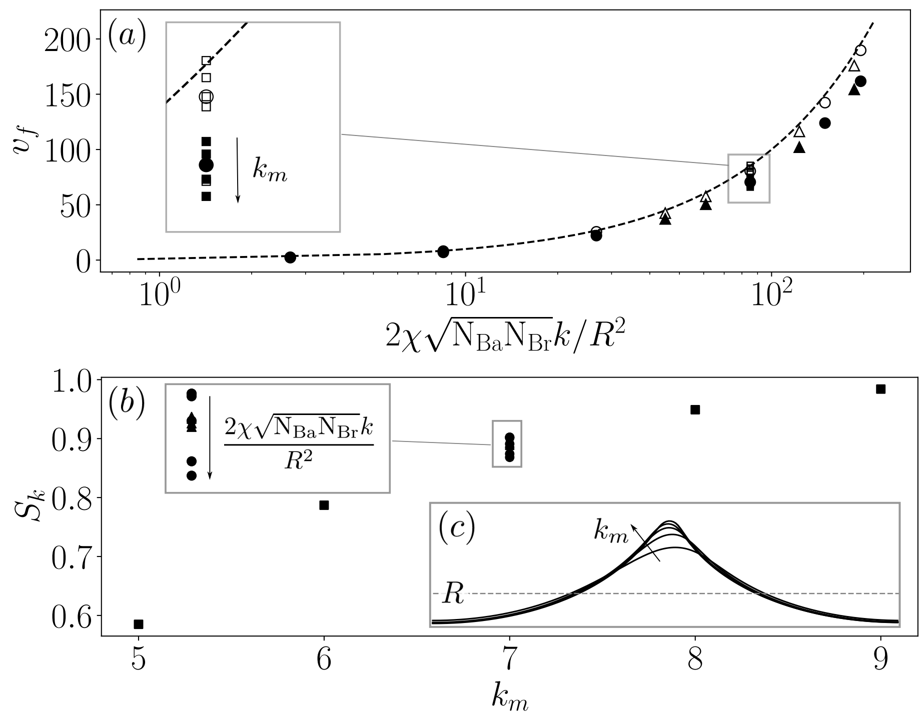

Figure 2.7. (a) Comparison of the propagation velocity predicted by linear theory v_f^L (dashed), weakly nonlinear theory v_f^W (empty symbols), and fully nonlinear simulation v_f^F (filled symbols). The circles represent results for case (i) $R = 1$ fixed and $\mathrm{N_{Ba}} \in [0, 10^{-3}, 10^{-2}, 10^{-1}, 1, 3, 5]$, the triangles represent results for case (ii) $\mathrm{N_{Ba}} = 1$ fixed with $\mathrm{N_{Br}}$ varying according to $R \in [0.8, 0.9, 1.1, 1.2]$, and the squares represent case (iii) $k_m \in [5, 6, 7, 8, 9]$, $R = 1$ and $\mathrm{N_{Ba}}, \mathrm{N_{Br}}$ determined so that $v_f^L = 85.16$. (b) The skewness Sk of the fully nonlinear profile. (c) The permanent wave shape (only one wavelength shown).

Figure 2.7(c) reveals that the wave profile for $k_m = 5$ ($\mathrm{N_{Ba}} = 1.9$, $\mathrm{N_{Br}} = 19.5$) is more asymmetric than the one for $k_m = 9$ ($\mathrm{N_{Ba}} = 0.60$, $\mathrm{N_{Br}} = 60.8$). Under a purely radial magnetic field ($\mathrm{N_{Ba}} = 0$), the stationary shape has azimuthal symmetry [59]. For the combined magnetic field, on the other hand, the dimensionless governing Eq. (2.2) and pressure boundary condition in Eq. (2.3) can be rewritten as

$$\mathbf{v} = -\boldsymbol{\nabla}\left(p - \mathrm{N_{Ba}}\frac{1}{r^2} - \mathrm{N_{Br}}r^2\right), \tag{2.22}$$

$$p = \kappa - \left[\chi\frac{\mathrm{N_{Ba}}}{r^2}(\hat{\boldsymbol{e}}_\theta \cdot \hat{\boldsymbol{n}})^2 + \chi\mathrm{N_{Br}}r^2(\hat{\boldsymbol{e}}_r \cdot \hat{\boldsymbol{n}})^2 + 2\chi\sqrt{\mathrm{N_{Ba}N_{Br}}}(\hat{\boldsymbol{e}}_\theta \cdot \hat{\boldsymbol{n}})(\hat{\boldsymbol{e}}_r \cdot \hat{\boldsymbol{n}})\right], \tag{2.23}$$

where

$$\hat{\boldsymbol{e}}_\theta \cdot \hat{\boldsymbol{n}} = \frac{-h_\theta}{h^2 + h_\theta^2}, \qquad \hat{\boldsymbol{e}}_r \cdot \hat{\boldsymbol{n}} = \frac{h}{h^2 + h_\theta^2}, \tag{2.24}$$

and $h_\theta = \partial h/\partial\theta$. The magnetic scalar potential in Eq. (2.22) results from the body force, and the terms pre-multiplied by χ in Eq. (2.23) represent the magnetic normal stress. For a droplet with symmetric azimuthal perturbation, the body force alone cannot break the symmetry. Therefore, the asymmetry of shapes discussed is to be attributed to the magnetic normal stress. This observation can be intuitively understood by considering one wavelength of a symmetric waveform. The first three terms on the right-hand side of Eq. (2.23) are equal on both sides of the peak, while the fourth term changes at the peak due to the sign of h_θ, which requires different curvatures on either side of the peak to remain balanced. Therefore, $\sqrt{\mathrm{N_{Ba}N_{Br}}}$ can be taken as the measure of the coupling effect between the magnetic field components.

To further understand the asymmetry of propagating shapes induced by the combined magnetic field, we extend the parameters of case (i) to a new case (iv): $k_m = 7$, $R = 1$ and $\mathrm{N_{Br}}$ varying according to $\mathrm{N_{Ba}}$ (see Fig. 2.8 caption). To quantify the fore-aft asymmetry of the shape [88], [89], we introduce

$$As(t) = \frac{\langle \mathcal{H}[\eta]^3 \rangle}{\langle \eta^2 \rangle^{3/2}}, \tag{2.25}$$

where $\mathcal{H}[\ \cdot\ ]$ is the Hilbert transform. For $As > 0$, waves tilt "forward" (*i.e.*, counter-clockwise). Figure 2.8(a) shows $As(t)$ for different $\sqrt{\mathrm{N_{Ba}N_{Br}}}$, which quantifies the coupled field effect, starting with small symmetric perturbations. For a stable case, $As(t)$ reaches a maximum value ($t \approx t_1$) during the initial unstable weakly nonlinear growth (dark shadow region), and asymptotes to a value close to zero ($t \geq t_6$). The differences in the final propagating profile (under the same k_m) shown in Fig. 2.8(b) are hard to capture, which is consistent with the observation in Fig. 2.7(b). For the unstable cases, "wave breaking" occurs, which is highlighted by a change of sign of As. Also, now, $As(t)$ no longer saturates at late t. Instead $As(t)$ crosses zero (at $t \gtrsim t_3$) and approaches a singularity. This unstable example is shown in the second row of Fig. 2.8(c). As its amplitude first grows, the wave tilts

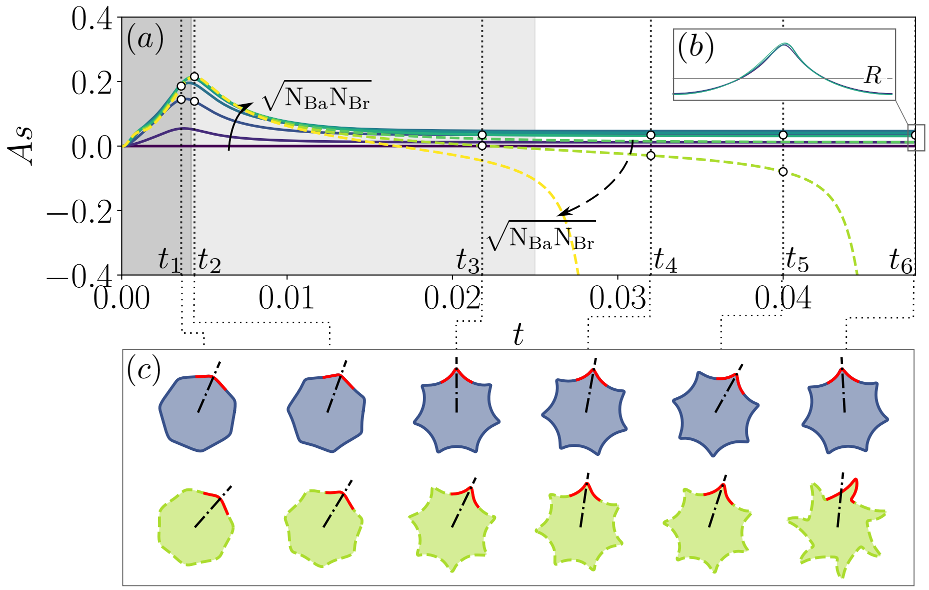

Figure 2.8. (a) Time evolution of the wave profile asymmetry for different combination of $\mathrm{N_{Ba}} \in [0, 0.1, 1, 3, 5, 6, 7, 8, 9]$ and $\mathrm{N_{Br}}$ varying so that $k_m = 7$ for $R = 1$. Solid curves represent stable cases yielding a propagating profile; dashed curves represent unstable cases in which the profile distorts and grows without bound. (b) Permanent wave profiles that emerge and propagate in a stable manner. (c) Stable (top, with $\mathrm{N_{Ba}} = 1, \mathrm{N_{Br}} = 37$) and unstable (bottom, $\mathrm{N_{Ba}} = 8, \mathrm{N_{Br}} = 41$) evolution of the profile. The instants of time (at which the shapes in (c) are shown) are marked with white dots in (a), superimposed on the asymmetry profiles.

forward ($t = t_2$), but nonlinear effects restore its symmetry ($t = t_3$). Subsequently, the wave tilts backwards ($t = t_4, t_5$) and its amplitude continues to grow ($t = t_6$). The calculation of As then fails because $\mathcal{H}$ requires the perturbation $\eta(\theta, t)$ to be single-valued in θ. The distorted wave has a wider base and evolves into long unstable fingers.

Note that $\mathrm{N_{Ba}}/\mathrm{N_{Br}}$ also increases with $\sqrt{\mathrm{N_{Ba}}\mathrm{N_{Br}}}$ for our choices of $\mathrm{N_{Ba}}$ and $\mathrm{N_{Br}}$. Equation (2.13) shows that the radial magnetic field is destabilizing, while surface tension ($k > 2$ here) and the azimuthal field are stabilizing. However, the nonlinear simulations indicate that, for the same k_m, increasing $\mathrm{N_{Ba}}/\mathrm{N_{Br}}$ can induce instability because it engenders a larger v_f (and As), leading to a global bifurcation with Fig. 2.5(d) as one stable slice. This result has an analogy to solitary waves in equations of the Kortweg–de Vries (KdV) type. Specifically, initial perturbations grow, deforming a shape until nonlinearity is balanced by dispersion, when a permanent wave emerges [90]. However, depending on the form of the nonlinearity, not all such permanent waves are stable attractors, and conditions must be placed on the wave speed [91].

2.5 Discussion

Although the manipulation of the linear growth rate of interfacial perturbations in Hele-Shaw cells is well studied [16], including extensions based on the weakly nonlinear expansion from Eq. (2.11) [92], the *control* of the dynamic, *fully nonlinear*, patterns is not. Our approach harnesses the magnitude and the direction of coupled magnetic fields to generate ferrofluid droplets, with well-characterized shapes and rotational speeds, by purely *external* means.

Open questions remain: *e.g.*, which fundamental modes evolve into propagating shapes? Work on the stationary problem [27], [93] gives a hint, however, for a propagating shape the Birkhoff integral equation [94] must be solved, making an extension of [27], [93] challenging. Interestingly, our simulations also reveal that patterns predicted as stable by weakly nonlinear analysis can be unstable. Figure 2.9, shows an example of a perturbation with $k = 4$ that will not evolve into either a stationary or a propagating shape (although both are predicted to exist by weakly nonlinear analysis).

Additionally, does this system accommodate more than one propagating wave? If so, do such waves keep their shapes upon collision, as with soliton interactions [90], [95]? Previous studies derived KdV equations for unidirectional small-amplitude, long-wavelength disturbances on fluid–fluid interfaces in Hele-Shaw [20] and axisymmetric ferrofluid configurations [84], [96], demonstrating the celebrated "sech^2" solitary wave. Instead, in our study without such restrictions, we discovered *periodic* traveling nonlinear waves, which are akin to the *cnoidal* solutions of periodic KdV, *i.e.*, the fundamental nonlinear modes ("soliton basis states") [97]. Additionally, we observed wave breaking [Fig. 2.8(c,bottom)].

Finally, it would be of interest to verify the proposed shape manipulation strategies by laboratory experiments. Previous theoretical studies [27], [37], [98], [99] suggest that many exact stationary droplet shapes are unstable, thus their relevance to experimental studies is

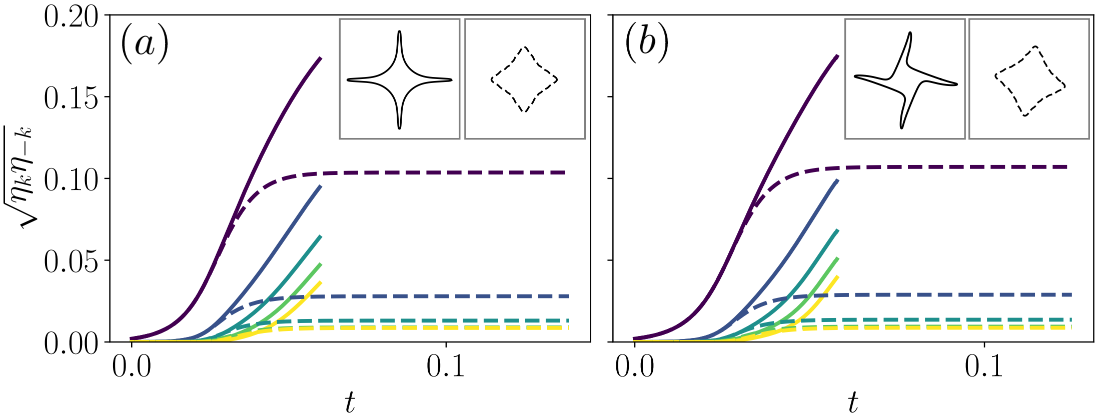

Figure 2.9. The unstable evolution of the first five harmonic modes ($k = 4, 8, 12, 16, 20$) from fully nonlinear simulation (solid) and their stable evolution from weakly nonlinear approximation (dashed) for (a) nonrotating ($k_m = 4$, $\mathrm{N_{Ba}} = 0$) and (b) rotating ($k_m = 4$, $\mathrm{N_{Ba}} = 1$) shapes.

limited. On the other hand, the nonlinear simulations in our study, showing stable rotation, pave the way for future experimental realizations.

3. LONG-WAVE EQUATION FOR A CONFINED FERROFLUID THIN FILM INTERFACE

SUMMARY

We study the dynamics of a ferrofluid thin film confined in a Hele-Shaw cell, and subjected to a tilted nonuniform magnetic field. It is shown that the interface between the ferrofluid and an inviscid outer fluid (air) supports traveling waves, governed by a novel modified Kuramoto–Sivashinsky-type equation derived under the long-wave approximation. The balance between energy production and dissipation in this long-wave equations allows for the existence of dissipative solitons. These permanent traveling wave's propagation velocity and profile shape are shown to be tunable via the external magnetic field. A multiple-scale analysis is performed to obtain the correction to the linear prediction of the propagation velocity, and to reveal how the nonlinearity arrests the linear instability. The traveling periodic interfacial waves discovered are identified as fixed points in an energy phase plane. It is shown that transitions between states (wave profiles) occur. These transitions are explained via the spectral stability of the traveling waves. Interestingly, multiperiodic waves, which are a non-integrable analog of the double cnoidal wave, also found to propagate under the model long-wave equation. These multiperiodic solutions are investigated numerically, and they are found to be long-lived transients, but ultimately abruptly transition to one of the stable periodic states identified above.

The material in this chapter was published as [Z. Yu and I.C. Christov, "Long-wave equation for a confined ferrofluid interface: Periodic interfacial waves as dissipative solitons," *Proc. R. Soc. A*, vol. 477, art. 20210550, 2021] [100] (authors retain rights to reproduce article in a thesis or dissertation). Both authors contributed to the analysis of the problem and the derivation of the mathematical model, which was led by Z.Y. Z.Y. wrote the Python scripts and conducted all the case studies and data analysis. Z.Y. and I.C.C. jointly discussed the results, drafted and revised the manuscript for publication.

3.1 Mathematical model and governing equations

Building on the work in Chapter 2, we study the dynamics of interfacial waves on a thin ferrofluid film, confined in the transverse direction within a Hele-Shaw cell with gap thickness b, as shown in Fig. 3.1. In the reference configuration, the unperturbed interface is at $r = R_0 + h_0$. The entire cell is subjected to a radially-varying external magnetic field via a long wire carrying an electric current I through the origin. This current produces an azimuthal magnetic field component $\mathbf{H}_a = \frac{I}{2\pi}\frac{1}{r}\hat{\boldsymbol{e}}_\theta$. Then, anti-Helmholtz coils can be used to produce a radial magnetic field component $\mathbf{H}_r = \frac{H_0}{R_0} r \hat{\boldsymbol{e}}_r$, where H_0 is strength of the magnetic field at $r = R_0$ [27], [59]. Now assume that $R_0 \gg h_0$, where h_0 is a characteristic 'depth' of the ferrofluid film at rest. Under this "small film curvature" assumption [101], the nonuniform magnetic field $\mathbf{H} = \mathbf{H}_a + \mathbf{H}_r$ can be approximated in locally Cartesian coordinates as:

$$\mathbf{H} \simeq \frac{I}{2\pi}\frac{1}{(R_0 + y)}\hat{\boldsymbol{e}}_x + \frac{H_0}{R_0}(R_0 + y)\hat{\boldsymbol{e}}_y. \tag{3.1}$$

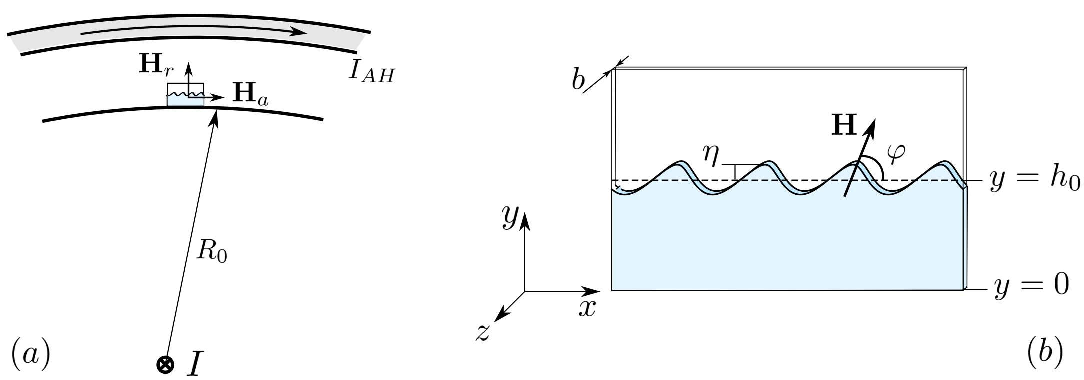

Figure 3.1. (a) Schematic illustration of a Hele-Shaw cell (width b) confining a thin ferrofluid film, with unperturbed depth h_0. An azimuthal magnetic field $\mathbf{H}_a$ can be produced by a long wire conveying an electric current I. A radial magnetic field $\mathbf{H}_r$ can be produced by a pair of anti-Helmholtz coils with equal currents I_{AH} in opposite directions. (In this schematic, the second coil would be under the one shown.) (b) The external magnetic field $\mathbf{H}$ approximated in the local Cartesian coordinates is tilted at angle φ with respect to the x-axis, and it acts to deforms the interface at $y = f(x,t) = h_0 + \eta(x,t)$. The fluid exterior to the thin film is assumed to have negligible viscosity and velocity ($e.g.$, air).

From Eq. (3.1), we understand that a magnetic body force $\propto |\mathbf{M}|\boldsymbol{\nabla}|\mathbf{H}|$ acts on the thin film, where $\mathbf{M}$ is the magnetization vector of the ferrofluid. For the purposes of studying the interface and shape dynamics [27], [58], [84], [85], we assume that the ferrofluid is uniformly magnetized, and the magnetization is collinear with the external field, *i.e.*, $\mathbf{M} = \chi\mathbf{H}$, where χ is the constant magnetic susceptibility. Since the applied field is spatially varying, *i.e.*, $\boldsymbol{\nabla}|\mathbf{H}| \neq \mathbf{0}$, then $\boldsymbol{\nabla}|\mathbf{H}|$ becomes the main contribution to the magnetic body force. According to the prior literature, this observation leads us to neglect the effect of the demagnetizing field in comparison.

It is straightforward to show by standard methods (see, *e.g.*, [27] and the references therein) that neglecting inertial hydrodynamic terms, enforcing the no-slip condition on the confining boundaries (transverse to the flow) of the Hele-Shaw cell, and averaging across the gap (*i.e.*, over z) yields a modified "Darcy's law" that governs this flow [27]:

$$\boldsymbol{v} = -\frac{b^2}{12\mu_f}\boldsymbol{\nabla}\left(p - \Psi\right), \qquad \boldsymbol{\nabla}\cdot\boldsymbol{v} = 0, \qquad -\infty < x < \infty, \quad 0 \leq y \leq f(x,t). \tag{3.2}$$

Here, p is the hydrodynamic pressure in the film, μ_f is the ferrofluid's dynamic viscosity, $\Psi = \mu_0\chi|\mathbf{H}|^2/2$ is a scalar potential accounting for the magnetic body force (such that $p-\Psi$ is a modified pressure), and μ_0 is the free-space permeability. Both fluids at the interface are considered incompressible. The viscosity of the "upper" fluid is considered negligible (*i.e.*, it is considered inviscid, as would be the case with air), so the flow outside the ferrofluid film is not considered. We denote by $\boldsymbol{v} = u(x,y,t)\hat{\mathbf{e}}_x + v(x,y,t)\hat{\mathbf{e}}_y$ the z-averaged velocity field in the "lower" fluid (the ferrofluid).

At the interface, having neglected the dynamics of the upper fluid, the pressure is given by a modified Young–Laplace law [8], [9]:

$$p = \sigma\kappa - \frac{\mu_0}{2}(\mathbf{M}\cdot\hat{\boldsymbol{n}})^2 \quad \text{on} \quad y = f(x,t), \tag{3.3}$$

where σ is the constant surface tension, and $\kappa \equiv -f_{xx}/(1+f_x^2)^{2/3}$ is the curvature of the surface $y = f(x,t)$ (x and t subscripts denote partial derivatives). The second term on the right-hand side of Eq. (3.3) is the magnetic normal traction [8], [9], where $\hat{\boldsymbol{n}} = (-f_x, 1)/\sqrt{1+f_x^2}$

denotes the upward unit normal vector to the interface. This contribution, due to the projection of $\mathbf{M}$ onto $\hat{\boldsymbol{n}}$, induces unequal normal stress on either side of the profile's peaks on the perturbed interface, thus breaking the initial equilibrium and leading to wave propagation, as discussed in Chapter 2.

A kinematic boundary condition is also imposed at the interface:

$$v = f_t + u f_x \quad \text{on} \quad y = f(x,t), \tag{3.4}$$

which requires that the film boundary is a material surface. The no-penetration condition

$$v = 0 \quad \text{on} \quad y = 0 \tag{3.5}$$

is imposed at the "bottom" of the layer, which is the material surface at $r = R_0$ in the original radial coordinates (Fig. 3.1), that maps to $y = 0$. Introducing the potential $\phi = p - \Psi - \Psi_0$, where the constant

$$\Psi_0 = -\frac{\mu_0}{2}\chi\frac{H_0^2}{R_0^2}(R_0+h_0)^2(1+\chi) - \frac{\mu_0}{2}\chi\frac{I^2}{4\pi^2}\frac{1}{(R_0+h_0)^2} \tag{3.6}$$

accommodates the trivial solution, and combining the two equations in (3.2) together, the governing equation becomes Laplace's equation:

$$\nabla^2\phi = 0, \tag{3.7}$$

From Eqs. (3.3) and (3.4), Eq. (3.7) is subject to the following boundary conditions on $y = f(x,t)$:

$$\begin{aligned}
&\phi + \frac{\mu_0\chi}{2}\frac{H_0^2(R_0+y)^2}{R_0^2} + \frac{\mu_0\chi}{2}\frac{I^2}{4\pi^2(R_0+y)^2} + d && (3.8)\\
&\quad = \sigma\kappa - \frac{\mu_0\chi^2}{2}\left[\frac{I^2}{4\pi^2(R_0+y)^2}\frac{f_x^2}{1+f_x^2} + \frac{H_0^2(R_0+y)^2}{R_0^2}\frac{1}{1+f_x^2} - \frac{IH_0}{\pi R_0}\frac{f_x}{1+f_x^2}\right], &&\\
&v = f_t + u f_x. && (3.9)
\end{aligned}$$

3.2 Derivation of the long-wave equation

3.2.1 Expansion of the potential and non-dimensionalization

To reduce the governing equations to a single partial differential equation (PDE) for the surface deformation η, we expand ϕ in a power series in y, a standard approach for small amplitude surface deformations (see, *e.g.*, [102]):

$$\phi(x, y, t) = \sum_{n=0}^{\infty} y^n \phi_n(x, t). \tag{3.10}$$

Substituting this expansion into Laplace's equation (3.7) generates a recursion relation $\phi_{n,xx} + (n+2)(n+1)\phi_{n+2} = 0$. On the other hand, since $\phi_y = \sum_{n=1}^{\infty} n y^{n-1}\phi_n(x,t)$, the constraint at the bottom (*i.e.*, Eq. (3.5)) requires that $\phi_1 = 0$, which eliminates the odd terms from the expansion. Hence, we can simplify Eq. (3.10) as:

$$\phi(x, y, t) = \sum_{m=0}^{\infty} \frac{(-1)^m y^{2m}}{(2m)!} g^{(2m)}(x, t), \qquad g^{(2m)}(x,t) \equiv \frac{\partial^{2m}}{\partial x^{2m}}\phi_0(x,t). \tag{3.11}$$

Let a be the typical amplitude scale for the surface deformation $\eta(x, t)$. Now, we introduce the following non-dimensionalization:

$$\begin{aligned} &x \mapsto \ell x, && y \mapsto h_0 y, && t \mapsto \frac{12\mu_f \ell^3}{\sigma b^2} t, && \eta \mapsto a\eta, \\ &u \mapsto \left(\frac{a}{h_0}\right) \frac{\sigma b^2}{12\mu_f \ell^2} u, && v \mapsto \left(\frac{a}{h_0}\right)\left(\frac{h_0}{\ell}\right) \frac{\sigma b^2}{12\mu_f \ell^2} v, && \phi \mapsto \left(\frac{a}{h_0}\right)\frac{\sigma}{\ell}\phi, && g \mapsto \left(\frac{a}{h_0}\right)\frac{\sigma}{\ell} g, \end{aligned} \tag{3.12}$$

where ℓ is the characteristic wavelength of the surface wave. Next, we define the small parameters of the model

$$\delta := \frac{h_0}{\ell}, \qquad \epsilon := \frac{a}{h_0}, \qquad \varepsilon := \frac{h_0}{R_0}, \tag{3.13}$$

corresponding to a wavelength parameter, an amplitude parameter, and a magnetic field gradient parameter, respectively. To implement the upcoming asymptotic expansion, a long wavelength $\delta \ll 1$ and small amplitude $\epsilon \ll 1$ approximation is made [103]. (Although it is possible to also derive arbitrary-amplitude long-wave equations [103], [104], Homsy

[105] argued that the distinguished limit of $\epsilon \ll 1$ leads to the *model* equations capturing the essential physics.) Note that $\varepsilon \ll 1$ is determined by the geometric configuration; specifically, R_0 is chosen sufficiently large to allow the Cartesian approximation, but small enough to ensure that $\boldsymbol{\nabla}|\mathbf{H}|$ is still the dominant term in the magnetic body force [27], [58], [84]. Note that demagnetization can still be neglected because it can be made arbitrarily small via the thickness b [85].

The scaled potential obeys:

$$\phi_{xx} + \frac{1}{\delta^2}\phi_{yy} = 0, \qquad u = -\phi_x, \qquad v = -\frac{1}{\delta^2}\phi_y, \tag{3.14}$$

and, to $\mathcal{O}(\delta^2)$, scaled and truncated Eq. (3.11) yields:

$$\phi = g - \delta^2 \frac{1}{2} y^2 g_{xx}, \tag{3.15a}$$

$$u = -g_x + \frac{1}{2}\delta^2 y^2 g_{xxx}, \tag{3.15b}$$

$$v = y g_{xx} - \frac{1}{6} y^3 \delta^2 g_{xxxx}, \tag{3.15c}$$

consistent with Eq. (3.14).

3.2.2 Boundary conditions and reduction of the governing equations

Keeping only terms up to $\mathcal{O}(\epsilon, \varepsilon^2, \delta^2)$, the corresponding kinematic and dynamic boundary conditions on the fluid–fluid interface become:

$$v = \eta_t + \epsilon u \eta_x \qquad \text{on} \quad y = 1 + \epsilon\eta(x,t), \tag{3.16a}$$

$$\phi = B_1\eta - \delta\eta_{xx} + \delta B_2 \eta_x + \epsilon\delta^2 B_3 \eta_x^2 - B_4 \epsilon \eta^2 \qquad \text{on} \quad y = 1 + \epsilon\eta(x,t), \tag{3.16b}$$

where B_n are constants given by

$$B_1 = 2\varepsilon[-\mathrm{N_{By}}(1+\chi) + \mathrm{N_{Bx}}] - 2\varepsilon^2[(1+\chi)\mathrm{N_{By}} + 3\mathrm{N_{Bx}}], \tag{3.17a}$$

$$B_2 = 2\chi\sqrt{\mathrm{N_{Bx}}\mathrm{N_{By}}}, \tag{3.17b}$$

$$B_3 = \chi[\mathrm{N_{By}}(1+2\varepsilon) - \mathrm{N_{Bx}}(1-2\varepsilon) + (\mathrm{N_{By}} - 3\mathrm{N_{Bx}})\varepsilon^2], \tag{3.17c}$$

$$B_4 = \varepsilon^2[(1+\chi)\mathrm{N_{By}} + 3\mathrm{N_{Bx}}]. \tag{3.17d}$$

Importantly, the constants are functions of the magnetic Bond numbers:

$$\mathrm{N_{Bx}} = \frac{\mu_0\chi}{2}\frac{I^2}{4\pi^2}\frac{1}{R_0^2}\frac{\ell}{\sigma}, \qquad \mathrm{N_{By}} = \frac{\mu_0\chi}{2}H_0^2\frac{\ell}{\sigma}, \tag{3.18}$$

which quantify the ratios of the magnitudes of the x and y components of the magnetic body force to the surface tension force. Before proceeding further in the analysis, we rewrite the boundary conditions from Eqs. (3.16) to hold at $y = 1$ through a Taylor series expansion of u, v, and ϕ:

$$v + v_y\epsilon\eta = \eta_t + \epsilon(u + u_y\epsilon\eta)\eta_x \qquad \text{on} \quad y = 1, \tag{3.19a}$$

$$\phi + \phi_y\epsilon\eta = B_1\eta - \delta\eta_{xx} + \delta B_2\eta_x + \epsilon\delta^2 B_3\eta_x^2 - B_4\epsilon\eta^2 \quad \text{on} \quad y = 1. \tag{3.19b}$$

With the relations in Eq. (3.14), Eqs. (3.19) can be rewritten, within the assumed order, as

$$v = \eta_t - \epsilon\left\{[B_1\eta_x + \delta(B_2\eta_{xx} - \eta_{xxx})]\eta\right\}_x \qquad \text{on} \quad y = 1, \tag{3.20a}$$

$$\phi = B_1\eta + \delta(B_2\eta_x - \eta_{xx}) - B_4\epsilon\eta^2 + \epsilon\delta^2(B_3\eta_x^2 + \eta\eta_t) \quad \text{on} \quad y = 1. \tag{3.20b}$$

Combining Eqs. (3.15), evaluated at $y = 1$, and Eqs. (3.20) allows us to eliminate $g(x,t)$, and the dynamics of the interface $\eta(x,t)$, up to $\mathcal{O}(\epsilon, \delta^2, \varepsilon^2)$, is governed by

$$\begin{aligned}\eta_t = {} & (-\varepsilon\alpha - \varepsilon^2\vartheta)\eta_{xx} + \delta(\beta\eta_{xxx} - \eta_{xxxx}) \\ & + \epsilon\left\{[(-\varepsilon\alpha - \varepsilon^2\vartheta)\eta_x + \delta(\beta\eta_{xx} - \eta_{xxx})]\eta\right\}_x - \epsilon\frac{1}{2}\varepsilon^2\vartheta(\eta^2)_{xx} \\ & + \frac{1}{2}\delta^2\left[\eta_{xxt} - \frac{1}{3}(-\varepsilon\alpha - \varepsilon^2\vartheta)\eta_{xxxx}\right] \\ & + \epsilon\delta^2\left[(\gamma\eta_x^2 + \eta\eta_t)_{xx} - \frac{1}{4}(-\varepsilon\alpha - \varepsilon^2\vartheta)(\eta^2)_{xxxx} + \frac{1}{12}\varepsilon^2\vartheta(\eta^2)_{xx}\right],\end{aligned} \tag{3.21}$$

where

$$\alpha = 2[\mathrm{N_{By}}(1+\chi) - \mathrm{N_{Bx}}], \tag{3.22a}$$

$$\beta = 2\chi\sqrt{\mathrm{N_{Bx}}\mathrm{N_{By}}}, \tag{3.22b}$$

$$\gamma = \chi(\mathrm{N_{By}} - \mathrm{N_{Bx}}), \tag{3.22c}$$

$$\vartheta = 2[(1+\chi)\mathrm{N_{By}} + 3\mathrm{N_{Bx}}], \tag{3.22d}$$

are now the governing dimensionless parameters of the model, beyond the previously defined small quantities in Eq. (3.13). Note that Eq. (3.21) is a general expression of the interface dynamics without any assumption about the relation between the (three) small parameters ϵ, δ, and ε. To obtain a *model* equation, in sense of [105], we must consider the relevant distinguished (asymptotic) limit.

3.2.3 The model long-wave equation

Next, we seek to simplify the governing Eq. (3.21) in the distinguished asymptotic limit(s) of interest. For $\varepsilon = \mathcal{O}(\delta^2)$, without loss of generality, we let $\varepsilon = \delta^2$ and conduct another rescaling:

$$\eta \mapsto \eta/\epsilon, \qquad t \mapsto t/\delta \tag{3.23}$$

to describe the long-time evolution (as expected, since we focus on traveling wave solutions). From Eq. (3.21), the interface evolution equation for $\varepsilon = \mathcal{O}(\delta^2)$ can be written as:

$$\eta_t = -\delta\alpha\eta_{xx} + \beta\eta_{xxx} - \eta_{xxxx} + [(-\delta\alpha\eta_x + \beta\eta_{xx} - \eta_{xxx})\eta]_x + \delta(\gamma\eta_x^2)_{xx}. \tag{3.24}$$

Setting $\varepsilon = \delta$ and performing the same re-scaling as given in Eq. (3.23), the interface evolution Eq. (3.21) for $\varepsilon = \mathcal{O}(\delta)$ reads:

$$\eta_t = (-\alpha - \delta\vartheta)\eta_{xx} + \beta\eta_{xxx} - \eta_{xxxx} + \{[(-\alpha - 2\delta\vartheta)\eta_x + \beta\eta_{xx} - \eta_{xxx}]\eta\}_x + \delta\gamma(\eta_x^2)_{xx}. \tag{3.25}$$

Observe that, whether $\varepsilon = \mathcal{O}(\delta)$ or $\varepsilon = \mathcal{O}(\delta^2)$, the resulting nonlinear evolution equation has a similar structure, since terms multiplied by $\delta\vartheta$ are small in comparison with the dominant α terms in Eq. (3.25) ($\alpha \approx \vartheta$ in the small-$\mathrm{N_{Bx}}$ regime within the scope of this study).

The main difference between the two scalings is the magnitude of individual terms, *e.g.*, terms multiplied by α in Eq. (3.25) can be compared to those multiplied by $\delta\alpha$ in Eq. (3.24). In this study, we are interested in traveling wave solutions, so that the coefficients α in Eq. (3.25) (and $\delta\alpha$ in Eq. (3.24)) are kept within a certain range. Therefore, since α, β and γ are expressed in terms of $\mathrm{N_{Bx}}$ and $\mathrm{N_{By}}$ (via Eq. (3.22)), then the different ranges for α in Eq. (3.25) and Eq. (3.24) necessarily leads to different ranges for β and γ in these equations (for given $\mathrm{N_{Bx}}$ and $\mathrm{N_{By}}$).

For example, in Eq. (3.24), the periodic wave with $k_m = 4$ requires $\alpha = 320$ in Eq. (3.24) and $\alpha = 32$ in Eq. (3.25). If we stay within the small tilt angle assumption, *i.e.*, $q = 0.01$ according to Eq. (3.32), then to maintain similar stability, the system where $\varepsilon = \mathcal{O}(\delta^2)$ requires a stronger magnetic field, *i.e.*, $\rho|_{\varepsilon=\mathcal{O}(\delta^2)} = (1/\delta)\rho|_{\varepsilon=\mathcal{O}(\delta)}$. Correspondingly, $\beta|_{\varepsilon=\mathcal{O}(\delta^2)} \approx 16.1$, while $\beta|_{\varepsilon=\mathcal{O}(\delta)} \approx 16.1\delta$. That means Eq. (3.25) is subjected to weaker dispersion, if we require that the base states under Eq. (3.24) and Eq. (3.25) both have the same linear stability properties.

Without losing generality, in this study we will focus on Eq. (3.24), which is a modified generalized KS equation. The main difference lies in the dispersion and nonlinear terms. Whereas the KS equation features the Hopf nonliterary $\eta\eta_x$ (as do the KdV and Burgers equations), Eq. (3.24) does not. Instead, the last two terms on the right-hand side of Eq. (3.24) depict a more complicated nonlinearity introduced *almost entirely* by the magnetic forces. One of the latter terms, $\propto (\eta_x\eta)_x$, is similar to the term due to the Maragoni effect in the so-called Korteweg–de Vries–Kuramoto–Sivashinsky–Velarde equation [106, Eq. (6)]. We note in passing that this term, together with the term $\propto (\eta_{xxx}\eta)_x$ and $\eta\eta_x$, also appear in the nonlinear terms of the model equation for interfacial periodic waves in [22, Eq. (9)]. As in present study, the $(\eta_{xxx}\eta)_x$ nonlinearity arises from surface tension. However, while $(\eta_x\eta)_x$ in [22, Eq. (9)] comes about from inertia, in our model equation this term arises from magnetic forces. Meanwhile, the role of the linear terms is well known, as in KS: η_{xx} is responsible for the instability at large scales, while η_{xxxx} term provides dissipation at small scales. As in the generalized KS equation (and in KdV), the η_{xxx} term in Eq. (3.24) leads to dispersion.

3.3 Stability of the flat state and nonlinear energy budget

3.3.1 Linear growth rate and weakly nonlinear mode coupling

Let $\eta(x,t) = \sum_{k=-\infty}^{\infty} \eta_k(t)e^{ikx}$ be the Fourier decomposition of the surface elevation on the periodic domain $x \in [0, 2\pi]$. Then, substituting the Fourier series into Eq. (3.24), we immediately obtain:

$$\dot{\eta_k} = \Lambda(k)\eta_k + \sum_{k'} F(k,k')\eta_{k'}\eta_{k-k'}, \tag{3.26}$$

where the overdot denotes a time derivative, $k \neq 0$, $k' \neq 0$, $\eta_{k=0} = 0$, $i = \sqrt{-1}$, and

$$\Lambda(k) = \delta\alpha k^2 - k^4 - i\beta k^3, \tag{3.27a}$$

$$F(k,k') = \delta\alpha kk' - i\beta kk'^2 - kk'^3 + 2\delta\gamma(k^2k'^2 - kk'^3). \tag{3.27b}$$

Recalling the definition of α from Eq. (3.22a), the real part of the linear growth rate $\mathrm{Re}\,[\Lambda(k)]$ indicates that the y-component of the magnetic field $\propto (1+\chi)\mathrm{N_{By}}$ is destabilizing, while the x-component $\propto \mathrm{N_{Bx}}$ and surface tension are stabilizing. Weakly-nonlinear mode coupling at the second-order is accounted for by the function F. Note that the terms in $\mathrm{Re}\,[\Lambda(k)]$ from

Eq. (3.27a) above are quite similar to Eq. (2.13) in Chapter 2 for a radial geometry, apart from being multiplied by an additional power of k.

The most unstable mode k_m satisfies:

$$\left.\frac{d\,\mathrm{Re}\,[\Lambda(k)]}{dk}\right|_{k=k_m} = 0 \qquad \Longleftrightarrow \qquad 2k_m^2 = \delta\alpha, \tag{3.28}$$

which implies the important role of $\delta\alpha$ on stability. Figure 3.2(a) shows examples of how $\delta\alpha$ controls the most unstable mode and determines the range of linearly unstable modes (for which $\mathrm{Re}\,[\Lambda(k)] > 0$). We will show that k_m (and $\delta\alpha$) can be used to predict the possible states (period of the nonlinear interfacial wave), and it is helpful for selecting suitable initial conditions that evolve into (nonlinear) traveling wave solutions.

The imaginary part of the linear growth $\mathrm{Im}\,[\Lambda(k)]$ rate reveals the phase velocity of each mode:

$$v_p(k) = -\,\mathrm{Im}\,[\Lambda(k)]/k = \beta k^2. \tag{3.29}$$

Perturbations to the flat base state of the film can propagate with velocity controlled by the coupling term $\beta = \chi\sqrt{\mathrm{N_{Bx}}\mathrm{N_{By}}}$ (and, since $v_p = v_p(k)$, they also experience dispersion). Here, β results from the magnetic normal stress due to the asymmetric projection of the x- and y-components of the magnetic force onto the interface. Changing the direction of the x-component of $\mathbf{H}$ will reverse the sign of these terms, *i.e.*, $\beta \mapsto -\beta$. The linear analysis indicates that such wavepackets will either decay or blow-up exponentially according to the sign of $\mathrm{Re}\,[\Lambda(k)]$. However, below we will show, through simulations of the governing PDE, that this linear instability is arrested by nonlinearity.

3.3.2 Nonlinear energy balance and the dissipative soliton concept

The energy method [107] can be applied to any PDE to understand the stability of its solutions. For example, the energy method was used to establish stability and uniqueness of generic ferrofluid flows [108]. Here, we employ this approach to understand the stability of the traveling wave in our model long-wave equation, which features both damping and

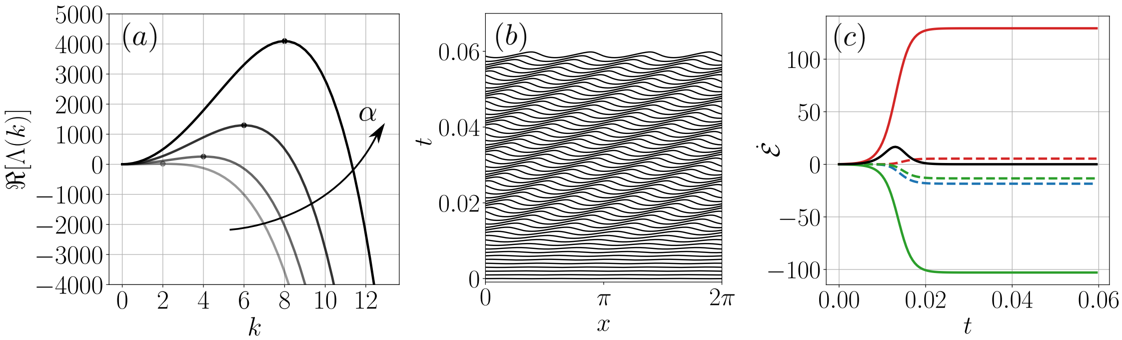

Figure 3.2. (a) Real part of the linear growth rate $\mathrm{Re}\,[\Lambda(k)]$ as a function of the wavenumber k for $\delta\alpha = 8$, 32, 72 and 128; the markers denote the most unstable mode k_m. (b) The nonlinear evolution of the interface from a small perturbation of the flat base state $[\eta(x,0) = 0.01\sin(4x)]$ into a permanent traveling wave with $\delta\alpha = 32$, $\beta = 16$, and γ determined by Eq. (3.22) accordingly. (c) Energy budget of the nonlinear traveling generation process shown in (b); the red curve represents the $\delta\alpha$ term, the green line represents the surface tension term, and the blue curve represents the β term from the PDE (3.24). The contribution of the linear term is denoted by the solid curves while the dashed curves represent the nonlinear term(s). The black curve in (c) shows the sum of these components, which is seen to approach zero as the wave evolves into a dissipative soliton.

gain. Multiplying Eq. (3.24) by η, and integrating by parts over $x \in [0, 2\pi]$, yields an energy balance:

$$\dot{\mathcal{E}} = \int_0^{2\pi} \delta\alpha\eta_x^2 - \eta_{xx}^2 + \delta\alpha\eta_x^2\eta + \frac{1}{2}\beta\eta_x^3 - \eta\eta_{xx}^2\, dx, \tag{3.30}$$

where $\mathcal{E}(t) \equiv \frac{1}{2}\int_0^{2\pi} \eta(x,t)^2\, dx$ denotes the total energy of the wave field. The $\delta\alpha\eta_x^2$ term on the right-hand side of Eq. (3.30) produces energy, while the surface tension term $-\eta_{xx}^2$ acts as a sink. This result matches well with the observation regarding the linear growth rate, *i.e.*, that the destabilizing $\delta\alpha$ term is balanced by the (stabilizing) surface tension ($\delta\alpha k^2 > 0$ and $-k^4 < 0$ in Eq. (3.27a)). The linear dispersion term conserves energy and thus drops out of Eq. (3.30). Meanwhile the sign of the three remaining terms is indeterminate *a priori*. Figure 3.2(c) show the evolution of the various terms on the right-hand side of Eq. (3.30) for the solution $\eta(x,t)$ shown in Fig. 3.2(b).

Eventually, all curves in Fig. 3.2(c) become independent of time. In general, we expect that, for some distinguished solutions $\eta(x,t)$, $\dot{\mathcal{E}} = 0$ holds exactly. If this is the case for one of the traveling wave solutions, then they are classified as *dissipative solitons* in the sense of [106]. Dissipative solitons are expected to be long-lived stable structures. We wish to address if such structures arise in our model of a ferrofluid interface subjected to a magnetic field.

From the energy analysis in Eq. (3.30), we can conclude that α, β, and γ are the three key parameters controlling the wave propagation and existence of the dissipative soliton. Recall that these three parameters, which show up in Eq. (3.24), are given as combinations of the physical parameters (*i.e.*, χ, $\mathrm{N_{Bx}}$, $\mathrm{N_{By}}$), as per Eq. (3.22). In particular, α and β in the linear terms of Eq. (3.24) are expected to strongly affect the stability and the characteristics of the traveling wave profile. We explore this issue next through numerical simulations.

3.3.3 Numerical simulation strategy for the governing long-wave PDE

To understand the nonlinear interfacial wave dynamics, in the upcoming sections below, we solve Eq. (3.24) numerically using the pseudospectral method [109]. For the linear terms, the spatial derivatives are evaluated using the fast Fourier transform (FFT) with $N = 512$, while the nonlinear terms are inverted back to the physical domain (via the inverse FFT), evaluated, and then transformed back to Fourier space. The modified exponential time-differencing fourth-order Runge–Kutta (ETDRK4) scheme [110], which is stable and accurate for stiff systems [109], is adopted for the time advancement. Figure 3.2(b) shows an example evolution from the infinitesimal perturbation of the flat state, to the formation of a nonlinear traveling wave.

A grid convergence study with three levels of the grid resolution was conducted to validate the pseudospectral method with ETDRK4 time stepping introduced in Section 3.3.3 for our model PDE (3.24). We demonstrate the grid convergence for the period-period traveling wave at $k_m = 4$, which is the most frequently discussed case. Figure 3.3(a) shows that the energy of harmonic modes decays with the wavenumber, and “piling up” occurs near the “tail” on the grids with $N = 512$ and $N = 1024$. This phenomenon is due to hitting the limit of double precision floating point arithmetic, which is indicative of spectral convergence. Additionally, the results on the grid with $N = 512$ match well with those of $N = 1024$. Actually, the

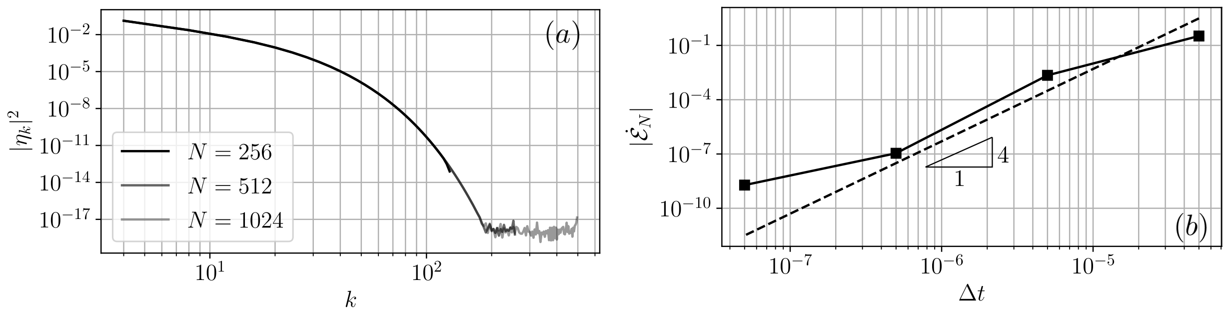

Figure 3.3. (a) Spectral energy of harmonic modes ($k = k_0, 2k_0, 3k_0, \ldots$, connected as a curve to "guide the eye") for the period-four traveling wave with $k_0 = 4$ at $k_m = 4$, $q = 0.01$, and $\Delta t = 5 \times 10^{-8}$. (b) The numerically computed dissipation rate error $\dot{\mathcal{E}}_N$ decreases with time step refinement for the same physical parameters as (a) and $N = 512$.

grid with $N = 256$ also provides a satisfactory result for the large scales ($k \in [4, 128]$) but the grid with $N = 512$ can resolve smaller scales better. Therefore, Fig. 3.3(a) supports our decision to use $N = 512$ for our simulations.

When the traveling wave solution is obtained, the energy change rate is supposed to reach a steady state, *i.e.*, $\dot{\mathcal{E}} = 0$, and the right-hand side of Eq. (3.30) vanishes as well. However, due to the numerical truncation, the sum of all the energy production/dissipation terms on the right-hand side actually changes with the time step Δt. Specifically, denote as $\dot{\mathcal{E}}_N = \dot{\mathcal{E}} - \int_0^{2\pi} \delta\alpha\eta_x^2 - \eta_{xx}^2 + \delta\alpha\eta_x^2\eta + \frac{1}{2}\beta\eta_x^3 - \eta\eta_{xx}^2 \, dx$ the error in the numerically computed dissipation rate. Four time steps $\Delta t = 5{\times}10^{-5}$, $5{\times}10^{-6}$, $5{\times}10^{-7}$, $5{\times}10^{-8}$ were considered for verification, and all give qualitatively consistent results. It is noteworthy that the time step spans two orders of magnitude, while the ETDRK4 scheme is still stable for this fourth-order stiff PDE. The dissipation rate error $\dot{\mathcal{E}}_N$ is shown in Fig. 3.3(b), and it exhibits fourth-order convergence with respect to Δt. Since time-step-convergence has been demonstrated, for this study, we use the intermediate time step size $\Delta t = 5 \times 10^{-8}$, which commits a dissipation rate error of $\dot{\mathcal{E}}_N = 1.91 \times 10^{-9}$, as a compromise between numerical accuracy and computational cost.

3.4 Nonlinear periodic interfacial waves: propagation velocity and shape

As discussed in Section 3.3.2, α and β play an important role in the energy balance. In this section, we will investigate their effects on the traveling wave's propagation velocity and the wave profile (shape). Before we start, it is helpful to discuss the physical meaning of these parameters, which can be useful in designing control strategies in practice.

First, as explained above, β is the coupling term resulting from the asymmetry of the surface force on the perturbed interface. This parameter is also closely related to the orientation of the magnetic field. To understand this point better, let

$$\rho = \mathrm{N_{Bx}} + \mathrm{N_{By}}, \qquad q = \mathrm{N_{Bx}}/\rho. \tag{3.31}$$

Here, $\rho \propto |\mathbf{H}|^2$ relates to the magnitude of the magnetic field at R_0, and $q = \cos^2\varphi$, where φ is the angle of $\mathbf{H}$ with respect to the flat interface (recall Fig. 3.1). With $\chi = 1$, the main parameters can be rewritten as:

$$\alpha = 2\rho(2 - 3q), \qquad \beta = 2\rho\sqrt{q(1-q)}, \qquad \gamma = \rho(1 - 2q). \tag{3.32}$$

In this study, we restrict ourselves to magnetic fields with small x-component magnitude, with $q \in [0, 0.06]$, *i.e.*, $\varphi \in [0.42\pi, \pi/2]$. For this choice, $\alpha \approx 4\rho$, $\beta \approx 2\rho\sqrt{q}$, and $\gamma \approx \rho$. Hence, controlling α is equivalent to controlling the magnitude of the magnetic field, while β is sensitive to the orientation. Note that two independent variables will set the dynamics, and in this section we will control α and β, with γ determined by Eq. (3.32). Furthermore, in the numerical studies below, we will use one initial condition, $\eta(x, t = 0) = 0.01\sin(k_0 x)$, with an initial perturbation wavenumber $k_0 = 4$, and we will only consider $\delta = 0.1$. These perturbations will first grow, then become arrested by saturating nonlinearity [111], and finally lead to a permanent traveling wave. The latter is of interest in this section.

3.4.1 Propagation velocity

Linear prediction and nonlinear expression

Lira and Miranda [41] reported that the propagation velocity of interfacial ferrofluid waves in a Cartesian configuration in a vertical Hele-Shaw cell is sensitive to the magnetic field's angle. Chapter 2 further showed that this velocity can be well predicted by the linear phase velocity, which is determined by the coupling term of azimuthal and radial magnetic field components in that work. In this study, we examine how this coupling term, which is captured by our parameter β (and closely related to the angle φ of the magnetic field), controls the nonlinear wave propagation velocity.

A permanent traveling wave profile takes the form $\eta(x,t) = \Theta(kx-\omega t)$, where $v_f = \omega/k$ is its propagation (phase) velocity. The modes' complex amplitudes can be expressed as $\eta_k(t) = c_k e^{-i\omega(k)t}$, with constant $c_k \in \mathbb{C}$ accounting for their relative phases. A nonlinear traveling wave profile would consist of a fundamental mode k_f and its harmonics nk_f ($n \in \mathbb{Z}^+$), with $\omega(nk_f) = n\omega(k_f)$, so that the phase velocity can be evaluated as $v_p(nk_f,t) = n\omega(k_f)/nk_f = v_f$. The average v_p of the first five harmonics is used to calculate v_f^N for the nonlinear simulation (same method as in Section 2.4.2). Meanwhile, the linear phase velocity $v_f^L = v_p$ is given by Eq. (3.29).

Figure 3.4(a) shows the comparison of the nonlinear propagation velocity and the linear prediction for $\delta\alpha = 32$. The fundamental mode, computed as $k_f = 4$ from the simulation, sets the linear propagation velocity as $v_f^L = \beta k^2 = 16\beta$. It is surprising to see that the actual nonlinear propagation velocity can be well fit by the straight line $v_f^N = 14.05\beta$ with small variance $\sigma^2 = 0.005$, even if the wave profiles changes with β dramatically, as shown in Fig. 3.4(c). This curious correction is not as trivial as it looks, as the nonlinear phase velocity can be evaluated *a posteriori* through Eqs. (3.27) as:

$$v_f^N = \beta \left\{ k^2 + \sum_{k'} k'^2 \,\mathrm{Re}\left[\frac{\eta_{k'}\eta_{k-k'}}{\eta_k}\right] - \frac{k}{\beta}\sum_{k'} [\delta\alpha k' - k'^3 + 2\delta\gamma(kk'^2 - k'^3)]\,\mathrm{Im}\left[\frac{\eta_{k'}\eta_{k-k'}}{\eta_k}\right] \right\}, \tag{3.33}$$

where the summation terms over k' represent the nonlinear effects. When a traveling wave solution is obtained, $\eta_{k'}\eta_{k-k'}/\eta_k = c_{k'}c_{k-k'}/c_k$ becomes independent of time, and the nonlinear phase velocity can be evaluated from Eq. (3.33), knowing c_k from the propagation profile's Fourier decomposition. (This is equivalent to our approach in Section 2.4.2). That approach is simpler, therefore the results hereafter follow the approach in Section 2.4.2 for simplicity and clarity.)

The correction in Eq. (3.33) is an *a posteriori* result, and it is accurate but not obvious how it changes the pre-factor $k^2 = 16$ into 14.05. Nevertheless, the strong, linear correlation between v_f^N and β for the chosen parameters of interest is the key point.

Multiple-scale analysis and velocity correction

To better understand the linear correlation between v_f^N and β, an analytical approximation can be obtained via a multiple-scale analysis of the harmonic wave [112]. However, when subject to the current parameters (*i.e.*, $k_m = 4$ as the most unstable mode), the linear instability poses difficulties when using a standard travailing wave ansatz. We introduce the critical wave number k_c so that $\mathrm{Re}\,[\Lambda(k_c)] = 0 \Rightarrow k_c^2 = \delta\alpha$. The linear theory predicts that all $k < k_c$ are unstable. Thus, we assume that the $\delta\alpha$ in the linear term is slightly larger than k_f^2, thereby making $k_f = 4$ marginally unstable, and also the unique unstable mode. In other words:

$$\delta\alpha = k_f^2 + \mathfrak{e}^2\varkappa, \tag{3.34}$$

where $\mathfrak{e} \ll 1$ is small perturbation parameter and $\varkappa > 0$ is independent of $\mathfrak{e}$. We first scale Eq. (3.24) to a weakly nonlinear problem by introducing $\eta = \mathfrak{e}\mathcal{Y}$:

$$\mathcal{Y}_t + \left(k_f^2 + \mathfrak{e}^2\varkappa\right)\mathcal{Y}_{xx} - \beta\mathcal{Y}_{xxx} + \mathcal{Y}_{xxxx} = \mathfrak{e}\left\{[(-\delta\alpha\mathcal{Y}_x + \beta\mathcal{Y}_{xx} - \mathcal{Y}_{xxx})\mathcal{Y}]_x + (\delta\gamma\mathcal{Y}_x^2)_{xx}\right\}. \tag{3.35}$$

Next, we introduce the traveling wave coordinate $\xi = kx - \omega_p t$ of a harmonic wave, where $\omega_p = k^3\beta$ by the linear dispersion relation. We assume that $\mathcal{Y}$ has a multiple-scale expansion of the form

$$\mathcal{Y} = \mathcal{Y}_0(\xi, t_2) + \mathfrak{e}\mathcal{Y}_1(\xi, t_2) + \mathfrak{e}^2\mathcal{Y}_2(\xi, t_2) + \mathcal{O}(\mathfrak{e}^3), \tag{3.36}$$

where the slow time is $t_2 = \mathfrak{e}^2 t$, and we obtain the following transformations of partial derivatives:

$$\partial_t = -\omega_p \partial_\xi + \mathfrak{e}^2 \partial_{t_2}, \qquad \partial_x = \partial_\xi. \tag{3.37}$$

Next, substituting the derivative transformations from Eq. (3.37) and the dependent variable expansion from Eq. (3.36) into the weakly nonlinear equation (3.35) gives rise to a series of problems at each order of $\mathfrak{e} \ll 1$.

- $\mathcal{O}(1)$:

  Denoting the linear operator as $\mathbb{L}$, the leading-order equation is given as:

$$\mathbb{L}[\mathcal{Y}_0] = \left(-\omega_p \partial_\xi + k_f^2 k^2 \partial_\xi^2 - \beta k^3 \partial_\xi^3 + k^4 \partial_\xi^4\right) \mathcal{Y}_0 = 0. \tag{3.38}$$

In this study, we are interested in the phase velocity of a single harmonic wave with wavenumber k, which is also subjected to weak linear instability if $\varkappa > 0$. So, we set $k_f = k$ and $\omega_p = k^3 \beta$. Then, the general solution of Eq. (3.38) is

$$\mathcal{Y}_0(\xi, t_2) = A_0(t_2) e^{i\xi} + c.c., \tag{3.39}$$

where $c.c.$ stands for complex conjugate.

- $\mathcal{O}(\mathfrak{e})$:

  At this order, we obtain an inhomogeneous PDE:

$$\mathbb{L}[\mathcal{Y}_1] = [(-\delta\alpha \mathcal{Y}_{0,\xi} + \beta \mathcal{Y}_{0,\xi\xi} - \mathcal{Y}_{0,\xi\xi\xi}) \mathcal{Y}_0]_\xi + \delta(\gamma \mathcal{Y}_{0,\xi}^2)_{\xi\xi}. \tag{3.40}$$

Substituting Eq. (3.39) into Eq. (3.40) we have:

$$\mathbb{L}[\mathcal{Y}_1] = 2[\delta\alpha k^2 - i\beta k^3 + (2\delta\gamma - 1)k^4] A_0^2 e^{2i\xi} + c.c. \tag{3.41}$$

The general solution of this PDE, denoted $\mathcal{Y}_1$, can be written as

$$\mathcal{Y}_1(\xi, t_2) = A_1(t_2)e^{i\xi} + A_{1p}(t_2)e^{i2\xi} + c.c., \tag{3.42}$$

where $\mathcal{Y}_{1p} = A_{1p}e^{i2\xi} + c.c.$ is the particular solution. Substituting $\mathcal{Y}_{1p}$ into Eq. (3.41), we obtain

$$A_{1p} = pA_0^2, \quad \text{with} \quad p = \frac{[\delta\alpha - i\beta k + (2\delta\gamma - 1)k^2]}{6k^2 + 3i\beta k}. \tag{3.43}$$

- $\mathcal{O}(\mathfrak{e}^2)$:

  At this order we obtain

$$\begin{aligned}\mathbb{L}[\mathcal{Y}_2] = &-(\mathcal{Y}_{0,t_2} + \varkappa k^2\mathcal{Y}_{0,\xi\xi}) \\ &-\delta\alpha k^2(\mathcal{Y}_{1,\xi\xi}\mathcal{Y}_0 + \mathcal{Y}_{0,\xi\xi}\mathcal{Y}_1 + 2\mathcal{Y}_{1,\xi}\mathcal{Y}_{0,\xi}) \\ &+\beta k^3(\mathcal{Y}_{1,\xi\xi\xi}\mathcal{Y}_0 + \mathcal{Y}_{0,\xi\xi\xi}\mathcal{Y}_1 + \mathcal{Y}_{1,\xi\xi}\mathcal{Y}_{0,\xi} + \mathcal{Y}_{0,\xi\xi}\mathcal{Y}_{1,\xi}) \\ &-k^4(\mathcal{Y}_{1,\xi\xi\xi\xi}\mathcal{Y}_0 + \mathcal{Y}_{0,\xi\xi\xi\xi}\mathcal{Y}_1 + \mathcal{Y}_{1,\xi\xi\xi}\mathcal{Y}_{0,\xi} + \mathcal{Y}_{0,\xi\xi\xi}\mathcal{Y}_{1,\xi}) \\ &+2\delta\gamma k^4(\mathcal{Y}_{1,\xi\xi\xi}\mathcal{Y}_{0,\xi} + \mathcal{Y}_{0,\xi\xi\xi}\mathcal{Y}_{1,\xi} + 2\mathcal{Y}_{1,\xi\xi}\mathcal{Y}_{0,\xi\xi})\end{aligned} \tag{3.44}$$

Substituting the previously obtained solutions $\mathcal{Y}_0$ and $\mathcal{Y}_1$ into Eq. (3.44), we have

$$\begin{aligned}\mathbb{L}[\mathcal{Y}_2] = &-(A_{0,t_2} - \varkappa k^2 A_0)e^{i\xi} \\ &+ d_0 A_1 A_0^* + d_1 A_{1p} A_0^* e^{i\xi} + d_2 A_1 A_0 e^{2i\xi} + d_3 A_{1p} A_0 e^{3i\xi} + c.c,\end{aligned} \tag{3.45}$$

where d_i are complex constant coefficients. We are only concerned with $d_1 = [\delta\alpha k^2 - 5i\beta k^3 - (7 + 4\delta\gamma)k^4]$.

To eliminate the secular term in Eq. (3.45), we require that

$$-(A_{0,t_2} - \varkappa k^2 A_0) + d_1 A_{1p} A_0^* = 0, \tag{3.46}$$

which gives rise to the amplitude equation

$$A_{0,t_2} = \varkappa k^2 A_0 - Q|A_0|^2 A_0, \tag{3.47}$$

which is known as the Landau equation, with $Q = -d_1 p$. Let $A_0 = \mathfrak{a} e^{i\mathfrak{b}}$, where $\mathfrak{a}$ and $\mathfrak{b}$ are real numbers. Then, the balance of the real and imaginary parts of Eq. (3.47) gives:

$$\frac{d\mathfrak{a}}{dt_2} = \varkappa k^2 \mathfrak{a} - \operatorname{Re}[Q]\mathfrak{a}^3, \tag{3.48}$$

$$\frac{d\mathfrak{b}}{dt_2} = -\operatorname{Im}[Q]\mathfrak{a}^2. \tag{3.49}$$

If $\operatorname{Re}[Q] > 0$, which is true after substituting the simulation parameters, three fixed point can be identified, with $\mathfrak{a} = 0$ being an unstable equilibrium point and $\mathfrak{a} = \pm\sqrt{\varkappa k^2 / \operatorname{Re}[Q]}$ being stable. The long-time behavior, as $t_2 \to \infty$, is that $\mathfrak{a}$ converges to these equilibrium points, and

$$\mathfrak{b}(t_2) \sim -\operatorname{Im}[Q]\frac{\varkappa k^2}{\operatorname{Re}[Q]} t_2 + \mathfrak{b}_0 \quad \text{as} \quad t_2 \to \infty. \tag{3.50}$$

Recall that $\mathcal{Y}_0(\xi, t_2) = A_0(t_2)e^{i\xi} + c.c. = \mathfrak{a}(t_2)e^{i(\xi + \mathfrak{b}(t_2))} + c.c. = 2\mathfrak{a}(t_2)\cos\Big(\xi + \mathfrak{b}(t_2)\Big)$, with $t_2 = \mathfrak{e}^2 t$, then the solution at the leading order can be obtained as:

$$\mathcal{Y}_0 = 2\mathfrak{a}\cos\left(kx - \omega_p t - k^2\frac{\operatorname{Im}[Q]}{\operatorname{Re}[Q]}\mathfrak{e}^2\varkappa t + \mathfrak{b}_0\right), \tag{3.51}$$

which gives the phase velocity with the multiple-scales correction as

$$v_f^{MS} = \beta k^2 + \frac{\operatorname{Im}[Q]}{\operatorname{Re}[Q]} k\mathfrak{e}^2\varkappa, \tag{3.52}$$

where $\mathfrak{a} = \sqrt{\varkappa k^2 / \operatorname{Re}[Q]}$ is the equilibrium amplitude, $\mathfrak{b}_0$ is an integration constant, and

$$Q = \frac{[\delta\alpha - i\beta k + (2\delta\gamma - 1)k^2]}{6k^2 + 3i\beta k}[-\delta\alpha k^2 + 5i\beta k^3 + (7 + 4\delta\gamma)k^4]. \tag{3.53}$$

Equation (3.52) predicts the propagation velocity of the traveling wave solution when $k_f = 4$ is subjected to weak linear instability. The weak linear instability is important to emphasize in this multiple-scales derivation because we assumed $\mathfrak{e}^2\varkappa \ll 1$. However, the results of this analysis appear to hold even for stronger linear instability. As $\delta\alpha$ in the original formulation increases from $k_f^2 = 16$, $\mathfrak{e}^2\varkappa$ increases correspondingly. In Fig. 3.4(a), we show two cases with $\delta\alpha = 18$ ($\mathfrak{e}^2\varkappa = 2$) and $\delta\alpha = 32$ ($\mathfrak{e}^2\varkappa = 16$). For the weakly linearly unstable case ($\delta\alpha = 18$), the propagation velocity v_f^{MS} predicted by the multi-scale expansion matches well with the nonlinear velocity v_f^N, with error less than 0.5%. For stronger linear instability, *i.e.*, $\delta\alpha = 32$, v_f^{MS} is still qualitatively corrected, but the error is now less than 26% for smaller β, while the agreement improves for larger β, with the error reducing to about 5%.

Another message obtained from Fig. 3.4 is that, even if the nonlinear propagation velocity v_f^N shows a linear correlation with β, it is not necessarily linearly related to β due to the nonlinearities of the PDE. However, this note will not change the fact that such linear correlation enables both v_f^L and v_f^{MS} to be good predictors for the wave dynamics (and their possible control via the imposed magnetic field). In this respect, another reason that v_f^L is a good quantitative prediction is the lack of "inertia" in this system. In the classical model equations, such as the KS, KdV, and Burgers, the $\eta\eta_x$ term accounts for nonlinear advection, and thus the initial "mass" ($\int_0^{2\pi} \eta\, dx$) sets the velocity. In our system, the nonlinear terms have a similar effect, while the initial "mass" $\int_0^{2\pi} \eta\, dx = 0$ due to the definition of η as a periodic perturbation. Thus, the propagation velocity is well predicted directly by the dispersion parameter β.

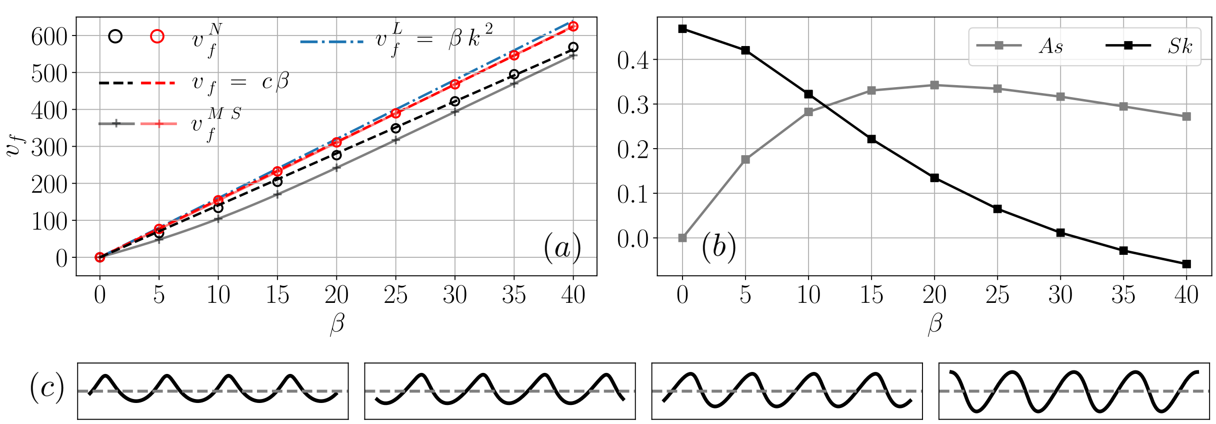

Figure 3.4. The dependence of (a) the propagation velocity, (b) the asymmetry and skewness on β for $\delta\alpha = 32$ and γ determined by Eq. (3.32), (c) example traveling wave profiles for $\beta = 0$, 10, 20, 40 for $\delta\alpha = 32$. In (a), the "$\circ$" denotes the nonlinear velocity evaluated from the simulation; the dashed line fits the nonlinear velocity with slope "c", and the solid line marked with "+" is the velocity prediction from the multiple-scales expansion. Black sets represent results with $\delta\alpha = 32$, while red ones are from $\delta\alpha = 18$.

3.4.2 Traveling wave profile

In addition to setting the propagation velocity, the coupling term β (as the source of asymmetry of the magnetic traction force) also strongly affects the shape of the traveling wave. To explore the shape change, as in Section 2.4.3, we introduce the skewness Sk and asymmetry As.

Figure 3.4(b) shows the effect of β on the wave profile for $k_m = 4$ (*i.e.*, for $\delta\alpha = 32$). The asymmetry is a concave function of β with a maximum around $\beta \approx 20$. This implies the existence of an "optimum" magnetic field angle that allows tuning of the wave profile shape. For the parameters used in Fig. 3.4(c), *i.e.*, $\delta\alpha = 32$ and $\beta = 0$, 10, 20, 40, correspondingly we have $q = 0, 3.9 \times 10^{-3}$, 0.015, 0.056, spanning two orders of magnitude of the magnetic field angle parameter. For $\beta = 0$ ($q = 0$), the profile is symmetric, and we observe that even a small angle of the magnetic field, breaks the fore-aft asymmetry of the wave profile. The skewness, on the other hand, monotonically decreases with the angle, becoming negative beyond $\beta \approx 30$.

Figure 3.5 shows how k_m (or, equivalently, α since δ is fixed) affects the wave profile. When the initial perturbation wavenumber $k_0 = 4$ is close to the most unstable mode k_m, the traveling wave profile maintains the same period as the initial condition. For larger k_m, the wave profile exhibits a sharper peak. This sharpening was also observed in Fig. 2.7(b,c) in Chapter 2, wherein the skewness increases with k_m, and the profiles saturate for large values of k_m. In Chapter 2, the possibly unstable evolution for k_m was not discussed, while the wave studied therein shows "wave breaking" for large values of the dispersion parameter. Therefore, an open problem that can be addressed with the present long-wave model is the "asymptotic" behavior of the steepening wave profile (As and Sk) with k_m. This leads us to a new question: is the range of k_m that allows such period-four waves bounded, or will the shape eventually become unstable (and/or "break")? Or, we can reframe the question as: given k_m, which states (period of the traveling wave) exist in this system? What about their stability? In the next section, we perform numerical investigations to shed light on these questions.

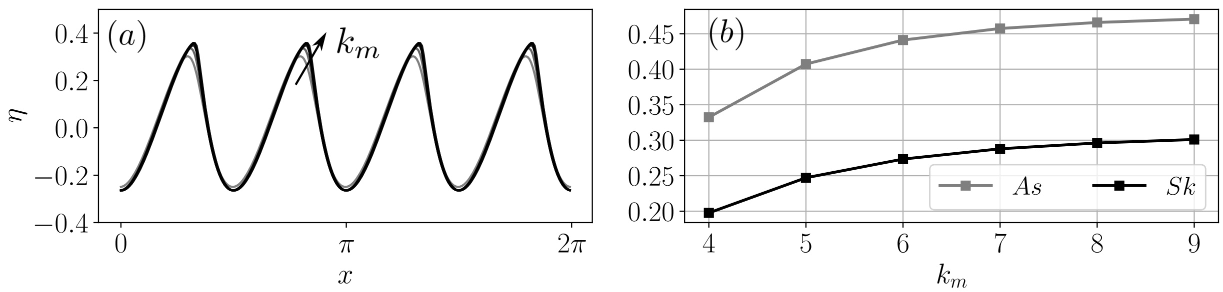

Figure 3.5. (a) The propagating wave profile with $k_m = 4, 5, \ldots, 9$, $q = 0.01$, with the initial perturbation wavenumber $k_0 = 4$, and β, γ determined by Eq. (3.22). (b) The corresponding asymmetry and skewness.

3.5 State transition and stability of traveling waves

The KS equation is well known for the chaotic behavior of its solutions. It has been thoroughly investigated within the scope of instability and bifurcation theory [113]–[116], yielding a wealth of results on how different dynamical states can be "reached" from given initial data, and the transition between such states. Specifically, as the ratio of coefficients of the second- and fourth-order derivative terms (*i.e.*, their relative importance, quantified by $\delta\alpha$ in our model (3.24)) increases, the KS equation's steady profile exhibits more complexity and dynamical possibilities, and finally the dynamics becomes chaotic. This feature can be understood intuitively from Fig. 3.2(a), wherein higher $\delta\alpha$ allows a wider unstable band for the long waves in the system.

Considering some of the similarities between our long-wave equation (3.24) and the generalized KS equation, a thorough examination of all the parametric dependencies of the wave (including chaotic) dynamics is not of interest herein. Instead, we focus on showing that the dissipative solitons emerging from perturbations in the linearly unstable band are fixed points in an energy phase plane. Then, we analyze the state transitions via this phase plane, and explain the stability of fixed points via the spectral stability of the wave profiles. Finally, we highlight multiperiodic profiles analogous to "double cnoidal waves" of the KdV equation.

3.5.1 Fixed points in the energy phase plane

To reduce the parameter space exploration, in this section we fix $q = 0.01$, with q defined in Eq. (3.31), and focus on the dynamics for different k_m only, by controlling the magnitude $\rho = 5, 20, 45, 80$. Recall that (as discussed at the beginning of Section 3.4) there are two independent physical dimensionless groups (*i.e.*, $\mathrm{N_{Bx}}$ and $\mathrm{N_{By}}$), so that fixing q and ρ determines all other parameters (*i.e.*, α, which sets k_m, β, and γ). In this subsection, the energy phase plane $(\mathcal{E}, \dot{\mathcal{E}})$ (see, *e.g.*, [116]) will be used to identify the traveling wave solutions, which emerge as fixed points with finite $\mathcal{E}$ and $\dot{\mathcal{E}} = 0$ (*i.e.*, they are dissipative solitons).

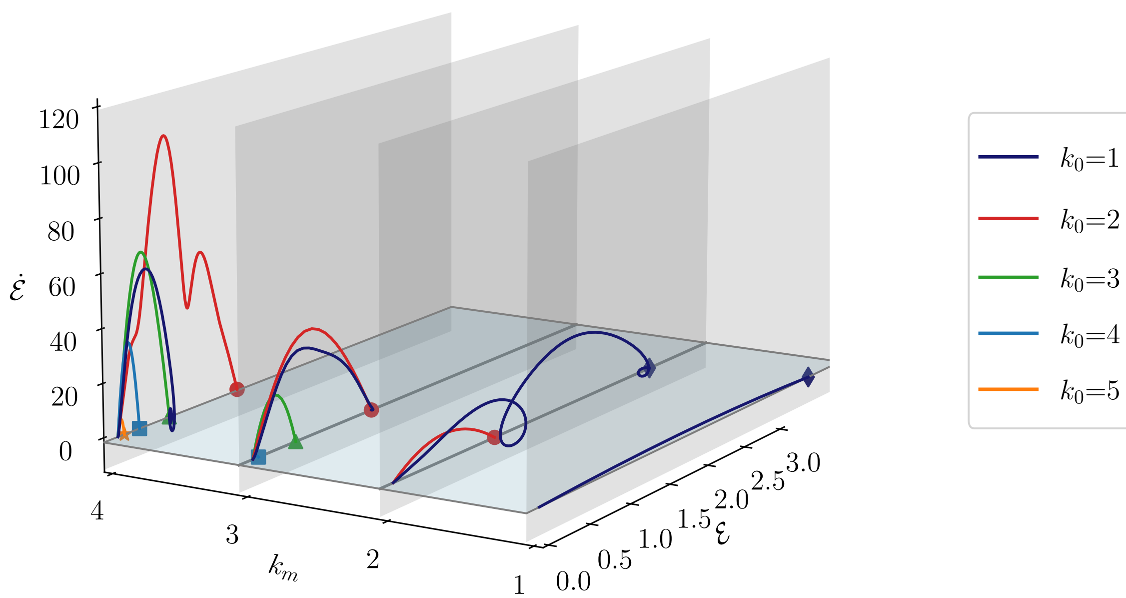

Figure 3.6. The energy phase plane $(\mathcal{E}, \dot{\mathcal{E}})$, showing dynamics in slices corresponding to most unstable wavenumbers $k_m \approx 1, 2, 3, 4$ ($\rho = 5, 20, 45, 80$) and, within each slice, the trajectories emerging from initial perturbations with wavenumbers $k_0 = 1, 2, 3, 4, 5$.

The wavenumber range, $k \in (0, k_c]$, of linearly unstable modes can be obtained by solving $\mathrm{Re}\,[\Lambda(k_c)] = 0$ to obtain $k_c = \sqrt{2}k_m$. Figure 3.6 shows four slices of the energy phase plane at $k_m = 1, 2, 3, 4$. The corresponding maximal linearly unstable modes have wavenumbers are $\lfloor k_c \rfloor = 1, 2, 4, 5$. As before, the initial condition is selected as a small-amplitude single-mode perturbation: $\eta(x, t = 0) = 0.01 \sin(k_0 x)$ with $k_0 = 1, 2, 3, 4, 5$ as the initial wavenumbers.

From the nonlinear growth rate in Eq. (3.27b), we know that a nonlinear interaction exists only between harmonic modes nk_0 ($n \in \mathbb{Z}$) when initializing with the single mode k_0. These interacting modes will grow or decay and finally become balanced harmonic components of the permanent traveling wave profile that emerges.

The fundamental mode k_f contains the highest energy, $\eta_{k_f}\eta^*_{k_f}$, in the system. Physically, the wave will exhibit a period-k_f profile, or a "k_f-state." For a period-k_f traveling profile, only the harmonic modes nk_f exist in the system. Therefore, the fixed points identified in Fig. 3.6 are of different periods for a given k_m. In Fig. 3.6, $k_0 \neq k_f$ when $k_0 = 1$, $k_m = 3, 4$.

For $k_m = 1$, only one initial mode, $k_0 = 1$, is linearly unstable, so that an initial perturbation with $k_0 > 1$ will decay exponentially back to base state (flat interface). On the other hand, the linearly unstable mode $k_0 = 1$ will first grow, then saturate to a traveling wave profile, and thus one fixed point can be identified in the $(\mathcal{E}, \dot{\mathcal{E}})$ phase plane. Similarly, picking $k_m = 2$ allows two linearly unstable modes, thus two fixed points in the energy phase plane. One fixed point is a period-one state, and the other is a period-two state.

However, while four unstable modes exists for $k_m = 3$, only three fixed points are identified with periods two, three and four. When initialized with $k_0 = 1$, the period-one perturbation evolves and converges to a period-two traveling wave, as can be seen from Fig. 3.6. Note that $k_0 = 1$ is a special case in terms of the nonlinear interaction. For $k_0 = 1$, all normal modes in the system are harmonic components, so that $k = 2, 3, 4$ will gain energy from $k_0 = 1$ also. A similar phenomenon can be observed in the $k_m = 4$ slice of the energy phase plane. The initial perturbations with modes $k_0 = 2, 3, 4, 5$ will evolve into states with corresponding $k_f = k_0$, while $k_0 = 1$ evolves into the period-three state.

Note that Fig. 3.6 shows only four slices at integer k_m, but k_m does not necessarily have to be an intege r (because it is set by the non-integer system parameter α via Eq. (3.28)). Thus, our discussion only provides a representative view of the rich higher-dimensional dynamics. It is evident, from the four slices in Fig. 3.6, that bifurcations of fixed points occur as the parameter k_m is varied. The number of fixed points increases with k_m, or more accurately, with the number of linearly unstable modes. Some fixed points move along the $\mathcal{E}$ axis with increasing k_m, such as the period-two and period-three states, while some disappear, like the period-one state. This observation partially answers the question of whether the number of traveling wave states will increase with k_m, and whether for certain states there is a possibly bounded ranged of k_m allowing them. However, what exactly is this bound for each state, or each k_m, is beyond of the scope of this study. This question would be challenging, since as k_m increases, more and more linearly unstable mode participate in the competition for setting the fundamental mode, and likely the system approaches a chaotic state.

3.5.2 Spectral stability of the traveling wave

The tendency of a system to prefer a narrow set of states out of many possible ones is known as wavenumber selection [117], [118]. In this section, we study this phenomenon by addressing the stability of these fixed points in the energy phase plane, focusing on the case of $k_m = 4$.

To this end, we perturb the traveling wave profile, and numerically track the evolution of the perturbation via direct simulation of the PDE. We find that period-two and period-three states behave like local attractors, while period-four and period-five states are saddle points. We verify the type of fixed points through spectral (in)stability analysis [119], [120]. Specifically, we rewrite Eq. (3.24) in the moving frame with $\zeta = x - v_f t$, $\tau = t$ as:

$$\eta_\tau - v_f \eta_\zeta = -\delta\alpha\eta_{\zeta\zeta} + \beta\eta_{\zeta\zeta\zeta} - \eta_{\zeta\zeta\zeta\zeta} + [(-\delta\alpha\eta_\zeta + \beta\eta_{\zeta\zeta} - \eta_{\zeta\zeta\zeta})\eta]_\zeta + \delta(\gamma\eta_\zeta^2)_{\zeta\zeta}, \tag{3.54}$$

with the propagation velocity v_f calculated numerically. The perturbed traveling wave solution is written as $\eta(\zeta, \tau) = \Xi(\zeta) + \mathfrak{d}W(\zeta)e^{\lambda\tau}$, where $\Xi(\zeta)$ is the stationary solution of Eq. (3.54) (hence, the traveling wave solution of Eq. (3.24)), and $\mathfrak{d} \ll 1$ is an arbitrary perturbation parameter. Substituting the perturbed $\eta(\zeta, \tau)$ into Eq. (3.54), and neglecting nonlinear terms, we obtain a linear eigenvalue problem

$$\lambda W = \mathcal{L}W, \qquad \mathcal{L} := \sum_{n=0}^{4} \mathcal{C}_n D_n. \tag{3.55}$$

Here, the $\mathcal{C}_n = \mathcal{C}_n(D_0\Xi, \ldots, D_4\Xi, v_f)$ are vector-valued functions of the traveling wave profile $\Xi(\zeta)$ and its gradients:

$$\begin{aligned} &\mathcal{C}_0 = \delta\alpha\Xi_{\zeta\zeta} + \beta\Xi_{\zeta\zeta\zeta} - \Xi_{\zeta\zeta\zeta\zeta}, \qquad \mathcal{C}_1 = v_f + 2\delta\alpha\Xi_\zeta + \beta\Xi_{\zeta\zeta} - \Xi_{\zeta\zeta\zeta} + 2\delta\gamma, \\ &\mathcal{C}_2 = \delta\alpha(1+\Xi) + \beta\Xi_\zeta + 4\delta\gamma\Xi_{\zeta\zeta}, \quad \mathcal{C}_3 = \beta(1+\Xi) - \Xi_\zeta + 2\delta\gamma\Xi_\zeta, \qquad \mathcal{C}_4 = -(1+\Xi). \end{aligned} \tag{3.56}$$

The differentiation matrices D_n are discretizations of $\partial^n/\partial\zeta^n$ ($D_0 = \mathbf{I}$ is the $N \times N$ identity matrix) evaluated by the Fourier spectral approach [109]. The eigenvalue problem Eq. (3.55) is solved numerically with `linalg.eig` from the NumPy stack in Python [121]. The spectrum was validated via a grid-independence study using grids with $N = 256$, 512, and 1024 points.

Next, we use this numerical spectral stability approach to understand the state transitions and the stability of fixed points in the energy phase plane introduced in Section 3.5.1.

3.5.3 The state transition process

Figure 3.7(a,b) shows that the period-three and period-two fixed points, respectively, in the $(\mathcal{E}, \dot{\mathcal{E}})$ phase plane are attractors. Small perturbations about them will decay, and the evolution will converge back to the corresponding periodic traveling wave profiles. This observation can be confirmed by the spectral stability calculation, its results shown in Fig. 3.7(f), which shows that all eigenvalues have negative real part, except for the zero eigenvalue, which represents the translational invariance of the traveling wave solution.

On the other hand, Fig. 3.7(c,d) show that the period-five and period-four fixed points, respectively, are saddles. A small perturbation around the period-four fixed point will grow and oscillate away, till the evolution converges to the period-three fixed point (an attractor), black curve in Fig. 3.7(d). For a different perturbation, gray curve in Fig. 3.7(d), this process can lead to convergence to the period-two attractor. The perturbation evolution around the period-five fixed point, black curve Fig. 3.7(c), is more interesting. It is featured by a two-stage transition process. First, the perturbation will first oscillate and grow rapidly, attracted to the neighborhood of the period-four fixed point. Then, it will oscillate away again, until finally converging to the period-three attractor. These saddle point behaviors can be confirmed from the linear eigenspectra shown in Fig. 3.7(f) as well. The period-four

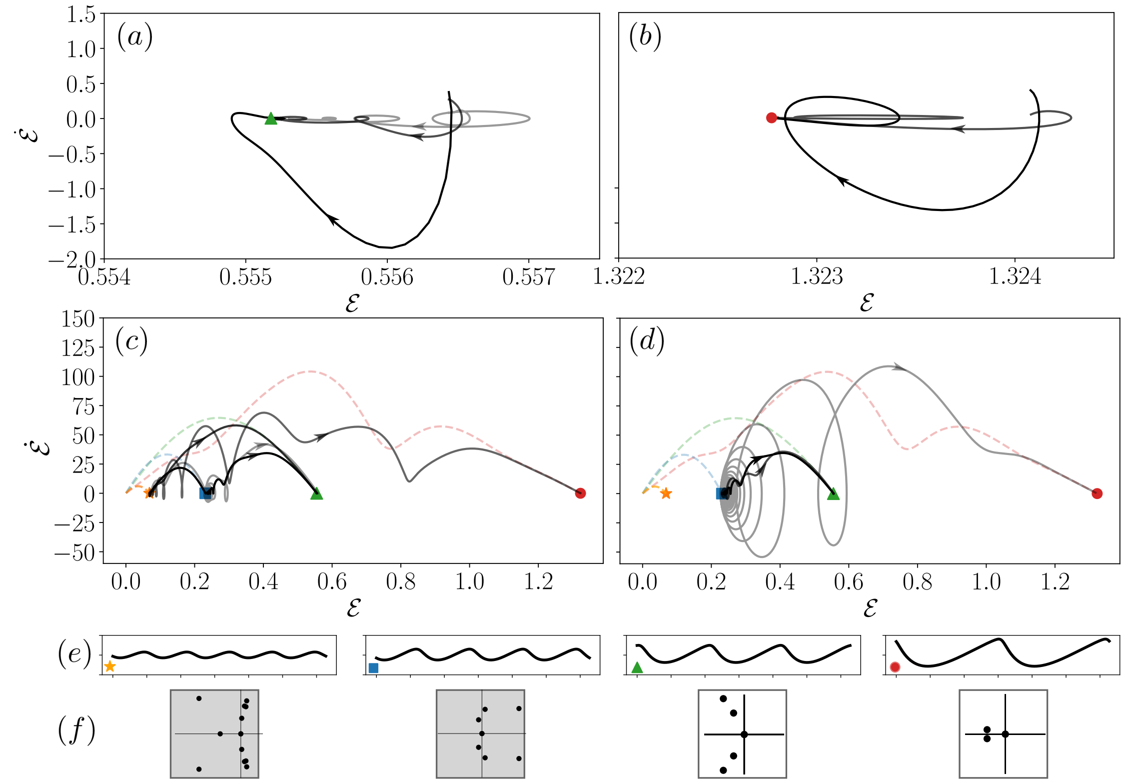

Figure 3.7. Stability diagram based on the energy phase plane. Perturbations around the attractors corresponding to (a) the period-three and (b) the period-two traveling wave solutions converge. State transitions are observed near the saddle points corresponding to (c) the period-five and (d) the period-four traveling wave profiles. The solid curves' colors represent initial perturbations with different wavenumbers, which lead to different dynamics (and outcomes). The wave profiles are shown in (e), with the symbols in the corners of the plots denoting the corresponding fixed points in the phase planes in (a,b,c,d). In (f), the leading eigenvalues of the linearization about the corresponding wave profile in (e) are shown.

profile has two pairs of conjugate eigenvalues with positive real part, while the period-five profile has four pairs.

A closer examination of the state transition process is shown in Fig. 3.8 for three representative perturbations around the period-five fixed point. Rapid oscillation of the modes' energies can be observed during the transition process, indicating intense nonlinear interactions. The space-time plot shows a similar phase shift feature as seen during the collision of solitons [90], but the wave profile is completely modified here. Figure 3.8(b) shows a one-stage transition due to a single-mode perturbation $\mathfrak{d}W(\zeta) = 0.02\sin(k_p\zeta)$, $k_p = 3$. This mode's energy $|\eta_3|$ increases exponentially, overtakes the initial $|\eta_5|$ value and converges to the period-three attractor. Figure 3.8(a,c) show a two-stage transition with single-mode perturbations $k_p = 1, 4$, respectively. Figure 3.8(a) shows higher level of oscillation than (c), since all modes are harmonics of $k_p = 1$, and higher $|\eta_1|$ can be observed for $t \in [0.05, 0.2]$. The interaction between mode 5 and mode 1 (Fig. 3.8(a)) immediately excites mode 4, and $|\eta_4|$ grows exponentially as the most unstable modes of the linear system. This results in a similar transition process for $k_p = 1$ and 4 in Fig. 3.8(a) and (c), respectively.

While such transition paths are complex and intriguing, we would like to emphasize the existence of the transition depends on the spectral stability of the traveling wave profile itself, which is interpreted as a saddle point or an attractor in the energy phase plane, and the transition direction is determined by the perturbation $W(\zeta)$. After an immediate targeted transition, whether another transition happens or not depends on the spectral stability of the subsequent wave profile attained.

Another intriguing aspect of this topic is multi-mode perturbations to the unperturbed flat interface, which is a more realistic situation that might arise in experiments, where the mode of the ambient noise is hard to control in an experiment. The competition between all possible states will finally select the observable pattern. Next we analyze this multi-mode case and provide an explanation of the selection process leading to multiperiodic nonlinear traveling waves.

3.5.4 Multiperiodic waves

An interesting observation from Fig. 3.8(a) is the coexistence of mode 1 and mode 4 during the transition, exemplified by the oscillations about the period-four fixed point in the energy phase plane shown in Fig. 3.7(c). The energy components of the wave profile are harmonics of $k_f = 4$, except the nontrivial $|\eta_1| \approx |\eta_8|$. During the time interval $t \in [0.05, 0.2]$, the space-time plot of wave profile evolution shows that a period-four wave is modulated by mode 1. This coexistence lasts for a relatively long time (compared to the total transition time) until mode 3 ultimately becomes dominant. An even longer coexistence is found when

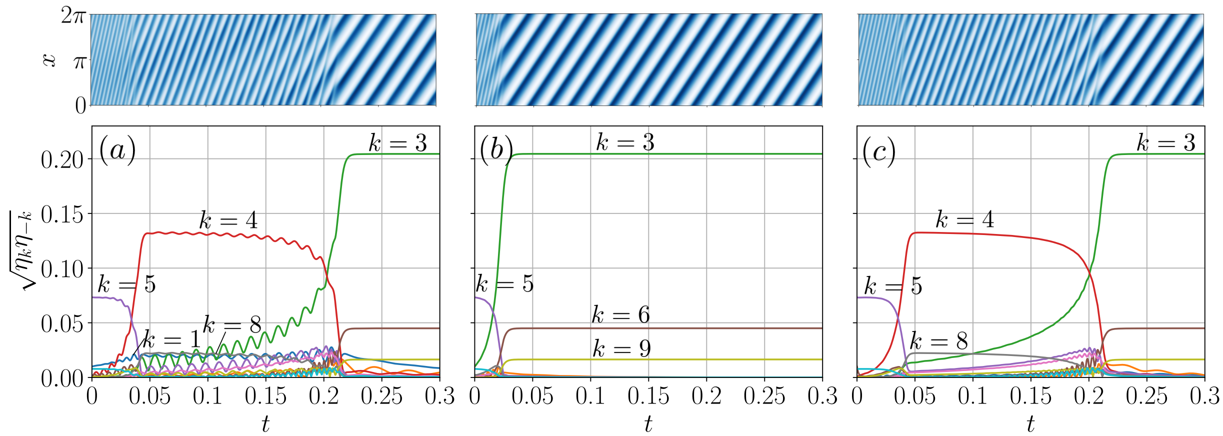

Figure 3.8. Fourier mode energy evolution (mode competition and nonlinear interaction) for a perturbed period-five traveling wave subjected to harmonic perturbation with (a) $k_p = 1$, (b) $k_p = 3$, and (c) $k_p = 4$. The top row shows the corresponding space-time plot of the transition process with color representing the amplitude of the wave profile η.

perturbing the period-four traveling profile with mode 2, as shown by the gray curve in Fig. 3.7(d), leading to a period-four wave modulated by mode 2, as in Fig. 3.9(a). The interaction between mode 2 and mode 4 occurs for $t \in [0, 0.6]$, an interval twice longer than any complete transitions in Fig. 3.8.

These long-lived multiperiodic waves states, which we have identified numerically, can be considered analogous to double cnoidal waves of the KdV equation. Double cnoidal waves are the spatially periodic generalization of the well-known two-soliton solution of KdV [122]. They can be considered as exact solutions with two independent phase velocities [123]. The evolution of the phase velocities $v_p(k)$ of modes $k = 2$ and 4 (of the Fourier decomposition of η) are shown in Fig. 3.9(b). The phase velocity of mode 2 experiences more intense oscillation than mode 4, which can be seen also from Fig. 3.9(a). These oscillations are caused by the energy interaction between even modes, and a low pass filter can be applied to evaluate a time-averaged phase velocity for mode 2, shown as the black curve (the jump around $t = 0$ is a windowing effect). It is surprising to see that while $|\eta_2|$, the amplitude of mode 2, is growing slowly, its phase velocity maintains around $v_p(k = 2) \approx 53.5$, which is independent of $v_p(k = 4) \approx 218.1$. Haupt and Boyd [123] constructed double cnoidal solutions of KdV

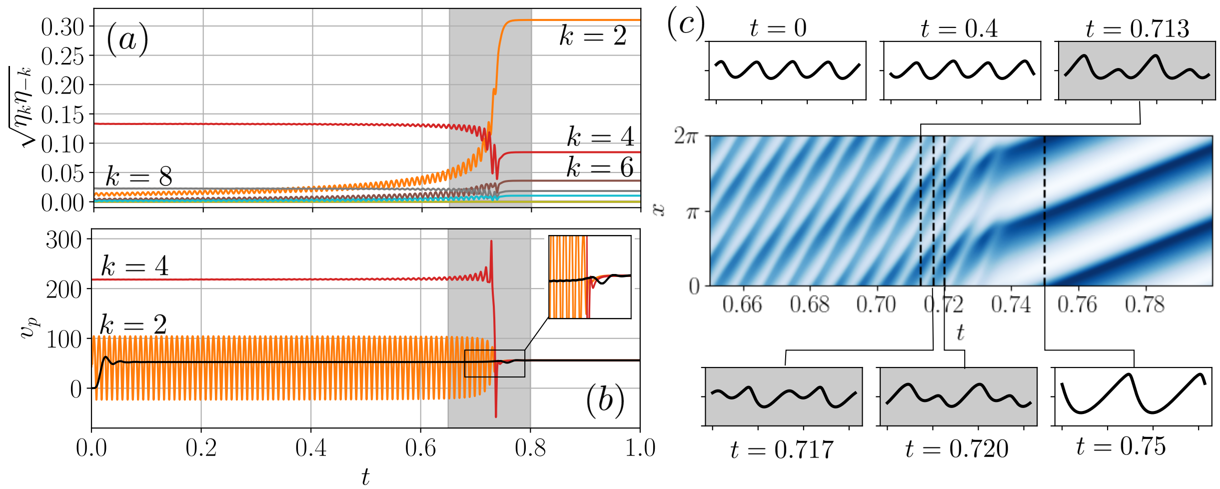

Figure 3.9. (a) Fourier modes energy interactions for a perturbed period-four traveling profile with perturbation $\mathfrak{d}W(\zeta) = 0.02\sin(2\zeta)$. ($b$) The phase velocities of mode 4 and mode 2. The black solid line shows the filtered $v_p(k=2)$. (c) Space-time plot and the corresponding wave profiles of the transition during $t \in [0.65, 0.8]$, marked as the grey region in (a) and (b).

through a harmonic balance of lower modes. On the other hand, the sharper peak of the quasi-double-cnoidal-waves in Fig. 3.9(c) shows the importance of the balance among higher harmonic modes in our model KS-type long-wave equation.

The rapid transition during $t \in [0.65, 0.8]$ is characterized by "wave chasing" in the physical domain. Mode 2 and mode 4 become comparable in Fourier energy, with mode 4 propagating faster than mode 2. Visually, this observation is similar to soliton collisions: when the peak of mode 2 is caught by that of mode 4, an elevation can be observed and then a decrease as they separate, shown in the wave profiles in Fig. 3.9(c) for $t \in [0.713, 0.72]$. However, while soliton collisions (in the sense of Zabusky and Kruskal [90]) leave the wave profile and propagation velocity unchanged, the "chasing" (and interaction) in the current study results in the waves ultimately merging into the period-two nonlinear traveling wave. The phase velocity of mode 4 dramatically decreases, and all modes in the system merge into a phase velocity $v_p \approx 55.8$, which becomes the propagation velocity v_f of the period-two traveling wave. It is interesting to note that, in this process, the time-averaged propagation velocity of mode 2 barely changes, except for the mitigation of the oscillations. This can be intuitively understood from the strong stability of the period-two traveling wave profile, while a mathematical reason might emerge from the singular limit of a double cnoidal wave (if it exists in this system).

In the end, this study answers one question posed in Chapter 2: when the energy of higher modes is dominant, this confined ferrofluid system can accommodate multiperiodic traveling waves, resembling a long-lasting, but non-integrable, double cnoidal wave field. When the energy of the two component modes becomes comparable, a rapid transition happens and the modulated propagating wave profile saturates to its envelope. In a sense, this means that these periodic nonlinear waves lose their shapes upon "collision." However, it would be interesting to ask if a localized solitary wave also exists for our model equation, and to address what would happen during the localized waves' collisions.

3.6 Discussion

We identified the allowed wave states (specifically, their spatial periods), which bifurcate as the most unstable linear mode k_m is varied, as fixed points in an energy phase plane, using the dissipative soliton concept [106]. State transitions are observed when some traveling wave profiles are perturbed, depending on their spectral stability, and the transition "direction" (towards another fixed point in the energy phase plane) is determined by the perturbation. It would be of interest to realize the obtained traveling wave profiles (and their transition dynamics) in laboratory experiments. The wave selection process with multi-mode perturbations poses a challenge in that the initial perturbation must be carefully controlled, especially for the spectrally unstable profiles.

Another novel feature of this study is that multiperiodic nonlinear waves (akin to the double cnoidal wave of the KdV equation) were found numerically in the context of a (non-integrable) long-wave equation of the modified KS type. Perturbations of spectrally stable modes interact intensely with their harmonics, which are already present as part of the original spectrally unstable traveling wave profile. Such interactions are long-lived, until an abrupt transition to a final stable traveling wave occurs. As mentioned in Section 3.5.4, we were unable to construct perturbative solutions in the sense of the double cnoidal waves

[123], therefore a complete mathematical explanation of these multiperiodic nonlinear wave dynamics (and the transitions between them) remains an open problem to be addressed in future work. Finally, it would also be of interest to derive a 2D version of our model long-wave equation, and the dynamics it governs could be compared and contrasted to resent work on the 2D KS equation [116].

4. DELAYED HOPF BIFURCATION AND TIME-DEPENDENT CONTROL OF A FERROFLUID INTERFACE

SUMMARY

In Chapter 2, fully nonlinear simulations revealed that the spinning gear emerges as a stable traveling wave along the droplet's interface bifurcates from the trivial (equilibrium) shape. In this chapter, a center manifold reduction is applied to show the geometrical equivalence between a two-harmonic-mode coupled system of ordinary differential equations arising from a weakly nonlinear analysis of the interface shape and a Hopf bifurcation. The rotating complex amplitude of the fundamental mode saturates to a limit circle as the periodic traveling wave solution is obtained. An amplitude equation is derived from a multiple-time-scale expansion as a reduced model of the dynamics. Then, inspired by the well-known delay behavior of time-dependent Hopf bifurcations, we design a slowly time-varying magnetic field such that the timing and emergence of the interfacial traveling wave can be controlled. The proposed theory allows us to determine the time-dependent saturated state resulting from the dynamic bifurcation and delayed onset of instability. The amplitude equation also reveals hysteresis-like behavior upon time reversal of the magnetic field. The state obtained upon time reversal differs from the state obtained during the initial (forward-time) period, yet it can still be predicted by the proposed reduced-order theory.

The material in this chapter was published as [Z. Yu, I.C. Christov, "Delayed Hopf bifurcation and control of a ferrofluid interface via a time-dependent magnetic field," *Phys. Rev. E*, vol. 107, art. 055102, 2023] [124] (authors retain rights to reproduce article in a thesis or dissertation). Both authors contributed to the analysis of the problem and the derivation of the mathematical model, which was led by Z.Y. Z.Y. wrote the Python scripts and conducted all the case studies and data analysis. Z.Y. and I.C.C. jointly discussed the results, drafted and revised the manuscript for publication.

4.1 Problem formulation and governing equations

In Chapter 2, the nonlinear evolution of the stably rotating ferrofluid droplet was studied mainly through fully nonlinear simulation. The low-dimensional ODEs, such as Eqs. (2.11) and (4.1) to be discussed below, arising from a weakly nonlinear analysis can also serve as a good approximation of the shape, but do not provide dynamical intuition beyond the initial, linear growth regime. In this study, we first derive a simpler model, using weakly nonlinear analysis, which allows us to gain dynamical insights. Then, we compare this new model with the nonlinear simulations performed using the vortex-sheet solver introduced and benchmarked in Chapter 2.

The simulations in Chapter 2 showed that the droplet shape exhibits a long-wave instability, and a finite number of harmonic modes can appropriately describe the dynamics. In this study, we are interested in the dynamics around the critical point, *i.e.*, when the system achieves $\mathrm{Re}\,[\Lambda(k_f)] = 0$, where k_f is the fundamental mode (we set $k_f = 7$ as in Chapter 2). When the fundamental mode is marginally unstable, *i.e.*, $\mathrm{Re}\,[\Lambda(k_f)] \gtrsim 0$, a small number of harmonic modes is sufficient to approximate the fully nonlinear dynamics. Thus, we first truncate Eq. (2.11) with four harmonic modes, $k = k_f, 2k_f, 3k_f, 4k_f$, representing the interactions with the fundamental mode. The representation using only four harmonic modes is sufficient for the parameters used in this study. This fact will be demonstrated *a posteriori* by comparison to the fully nonlinear simulation in Figs. 4.4, 4.7, 4.8, and 4.9. To obtain an explicit-in-time system of equations for η_k, we further eliminate $\dot{\eta}_{k'}$ on the right-hand side of Eq. (2.11) by reusing the equation itself. We thus obtain a system of four nonlinear ODEs:

$$\dot{x} = a_1 x + a_2 x^* y + a_3 y^* z + a_4 z^* p, \tag{4.1a}$$

$$\dot{y} = b_1 y + b_2 x^* z + b_3 y^* p + b_4 x^2, \tag{4.1b}$$

$$\dot{z} = c_1 z + c_2 x^* p + c_3 xy, \tag{4.1c}$$

$$\dot{p} = d_1 p + d_2 xz + d_3 y^2, \tag{4.1d}$$

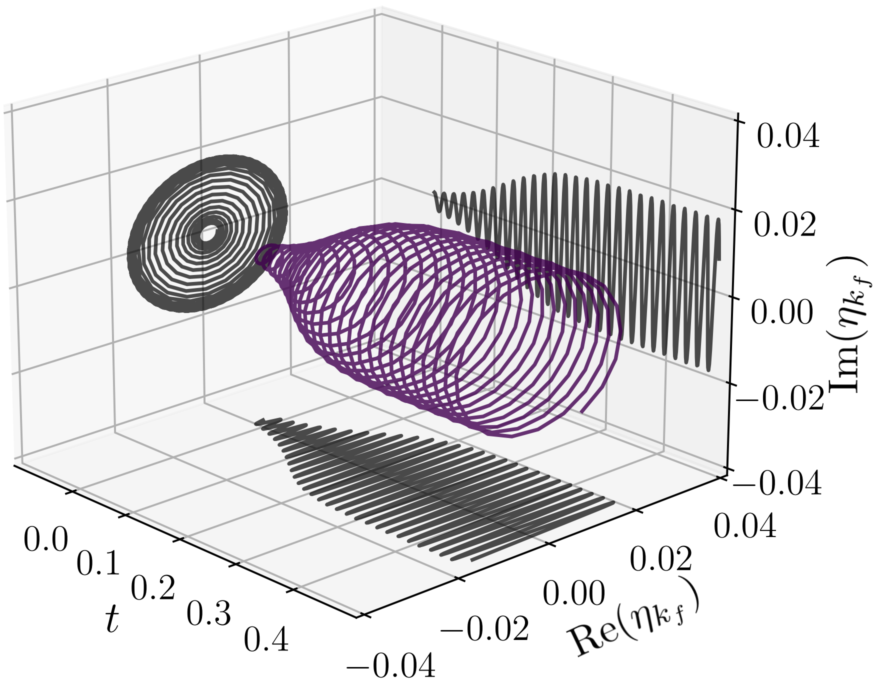

Figure 4.1. The evolution of the fundamental mode k_f from a fully nonlinear simulation with $\mathrm{N_{Ba}} = 1$ and $\mathrm{N_{Br}} = 13$.

where $x = \eta_{k_f}$, $y = \eta_{2k_f}$, $z = \eta_{3k_f}$, $p = \eta_{4k_f}$. The superscript $*$ denotes complex conjugation. The system (4.1) retains all second-order terms in the perturbation's amplitude. The expressions for the complex coefficients a_j, b_j, c_j, and d_j are given in Appendix 4.1.

4.2 Traveling wave solution and its stability

The system (4.1) can be conveniently written in polar form by setting $j = r_j(t)e^{i\phi_j(t)}$, where $j \in \{x, y, z, p\}$. Under this transformation, the evolution equations for the amplitudes $r_j \in \mathbb{R}$ and phase angles $\phi_j \in \mathbb{R}$ of the first four harmonic modes become decoupled, yielding separate ODEs for the real and imaginary parts of the complex ODEs. The complex ODEs are written as:

$$\dot{r}_x + i\dot{\phi}_x r_x = a_1 r_x + a_2 r_x r_y e^{i(\phi_y - 2\phi_x)} + a_3 r_y r_z e^{i(\phi_z - \phi_y - \phi_x)} + a_4 r_z r_p e^{i(\phi_p - \phi_z - \phi_x)}, \tag{4.2a}$$

$$\dot{r}_y + i\dot{\phi}_y r_y = b_1 r_y + b_2 r_x r_z e^{i(\phi_z - \phi_x - \phi_y)} + b_3 r_y r_p e^{i(\phi_p - 2\phi_y)} + b_4 r_x^2 e^{i(2\phi_x - \phi_y)}, \tag{4.2b}$$

$$\dot{r}_z + i\dot{\phi}_z r_z = c_1 r_z + c_2 r_x r_p e^{i(\phi_p - \phi_x - \phi_z)} + c_3 r_x r_y e^{i(\phi_x + \phi_y - \phi_z)}, \tag{4.2c}$$

$$\dot{r}_p + i\dot{\phi}_p r_p = d_1 r_p + d_2 r_x r_z e^{i(\phi_x + \phi_z - \phi_p)} + d_3 r_y^2 e^{i(2\phi_y - \phi_p)}. \tag{4.2d}$$

For the original droplet problem in Chapter 2, the traveling wave solution on the periodic domain $[0, 2\pi]$ can be written as $\eta(\theta, t) = \sum_{k=-\infty}^{+\infty} r_k e^{i\phi_k(t)}$, where the real amplitudes r_k are independent of time and related to the complex amplitudes in Eq. (2.7) via $\eta_k = r_k e^{-ikv_p t + \phi_{0,k}}$. The phase depends on time as $\phi_k(t) = k(\theta - v_p t) + \phi_{0,k}$, such that $\dot{\phi}_k = -kv_p$ with v_p being the (right) propagation speed of the traveling wave. Here, the $\phi_{0,k}$ describe the relative phase difference with respect to the fundamental mode. One example of a fully nonlinear simulation is shown in Fig. 4.1, where the magnitude $r_{k_f} = |\eta_{k_f}(t)|$ of the fundamental mode's rotating complex amplitude $\eta_{k_f}(t)$ saturates to a constant as the traveling wave solution is achieved.

To understand this traveling wave solution, we set $\dot{r}_x = \dot{r}_y = \dot{r}_z = \dot{r}_p = 0$ and

$$\begin{aligned} \phi_x &= \Omega t, & \phi_y &= 2\Omega t + \phi_{0,y}, \\ \phi_z &= 3\Omega t + \phi_{0,z}, & \phi_p &= 4\Omega t + \phi_{0,p}, \end{aligned} \tag{4.3}$$

where $\Omega = -k_f v_p$ is the rate of change of the phase of the fundamental mode k_f. Substituting the traveling wave solution (4.3) into the system (4.1) (or in the polar form system (4.2)) gives rise to:

$$(i\Omega - a_1)r_x = a_2 r_x r_y e^{iD} + a_3 r_y r_z e^{iA} + a_4 r_z r_p e^{iB}, \tag{4.4a}$$

$$(i2\Omega - b_1)r_y = b_2 r_x r_z e^{iA} + b_3 r_y r_p e^{iC} + b_4 r_x^2 e^{-iD}, \tag{4.4b}$$

$$(i3\Omega - c_1)r_z = c_2 r_x r_p e^{iB} + c_3 r_x r_y e^{-iA}, \tag{4.4c}$$

$$(i4\Omega - d_1)r_p = d_2 r_x r_z e^{-iB} + d_3 r_y^2 e^{-iC}, \tag{4.4d}$$

where $A = \phi_{0,z} - \phi_{0,y}$, $B = \phi_{0,p} - \phi_{0,z}$, $C = \phi_{0,p} - 2\phi_{0,y}$ are the relative phase difference. The latter three unknowns, together with r_x, r_y, r_z, r_p, and Ω, characterize the nonlinear traveling wave; note that D is calculated from A, B, and C as $D = A + B - C$.

Equations (4.4) are solved using a Newton–Krylov method available in the SciPy library [125]. The solutions are shown in Fig. 4.2. Near the critical point of the system, when $\mathrm{Re}(a_1) = 0$, the magnitudes of the higher-order modes (*i.e.*, r_z and r_p) become small (comparable to machine precision), and the Newton–Krylov method struggles to converge.

On the other hand, as the nonlinearity becomes weaker, the system can be approximated by an even lower-order system. Taking $z = p = 0$, the system (4.1) reduces to

$$\dot{x} = a_1 x + a_2 x^* y, \tag{4.5a}$$

$$\dot{y} = b_1 y + b_4 x^2, \tag{4.5b}$$

and the stationary solution r_x is found from (4.5) to satisfy

$$(b_1 - 2i\Omega)(a_1 - i\Omega) = a_2 b_4 r_x^2. \tag{4.6}$$

This stationary solution is shown in Fig. 4.2. One immediate conclusion that can be drawn from Eq. (4.6) is that at the critical point, when $\mathrm{Re}(a_1) = 0$, one solution is $\Omega = \mathrm{Im}\,(a_1)$ and $r_x = 0$. This solution corresponds to the non-hyperbolic equilibrium point. Along this solution branch of Eq. (4.6), if $\mathrm{Re}(a_1)$ were to further decrease (and become negative), then $r_x^2 < 0$, and thus there are no real solutions for r_x. In other words, the traveling wave solution does not exist (initial perturbation to the equilibrium state decay).

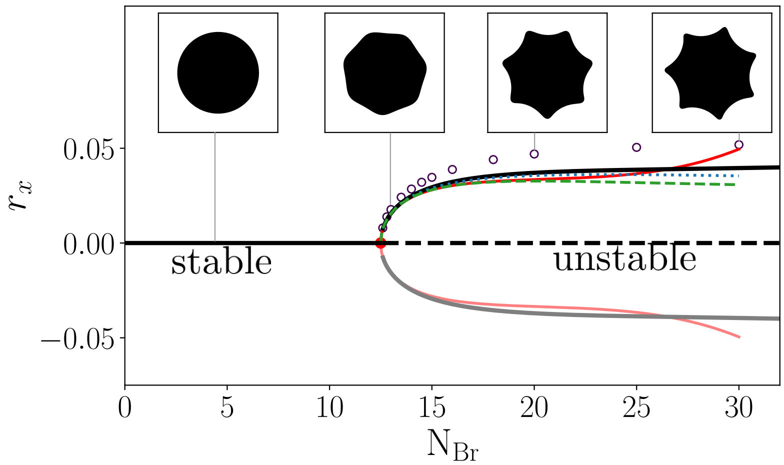

Figure 4.2. The fundamental mode's amplitude bifurcates with $\mathrm{N_{Br}}$. The circles mark the amplitude from the fully nonlinear simulations. The black and gray solid curves show the solution of the four-mode coupling system (4.4), while the gray curve (with negative amplitude) has no physical meaning. The black dashed line represents the unstable trivial solution $r_j = 0$, $j \in \{x, y, z, p\}$. The red curve shows the solution near the critical point obtained from the reduced model (4.6). The green dashed line shows the result from the center manifold reduction (4.15). The blue dotted line shows the multiple-time-scale analysis result from Eq. (4.29). An azimuthal field with $\mathrm{N_{Ba}} = 1$ is used, and to set the critical point of the system, *i.e.*, $\mathrm{Re}(a_1) = 0$ for $k_f = 7$, we must take $\mathrm{N_{Br}} = 12.5$.

Next, we address the question of the stability of the traveling wave solution. We perturb the complex stationary solution by taking

$$x(t) = \left(\epsilon_x + r_x e^{i\phi_{0,x}}\right) e^{i\Omega t}, \tag{4.7a}$$

$$y(t) = \left(\epsilon_y + r_y e^{i\phi_{0,y}}\right) e^{i2\Omega t}, \tag{4.7b}$$

$$z(t) = \left(\epsilon_z + r_z e^{i\phi_{0,z}}\right) e^{i3\Omega t}, \tag{4.7c}$$

$$p(t) = \left(\epsilon_p + r_p e^{i\phi_{0,p}}\right) e^{i4\Omega t}. \tag{4.7d}$$

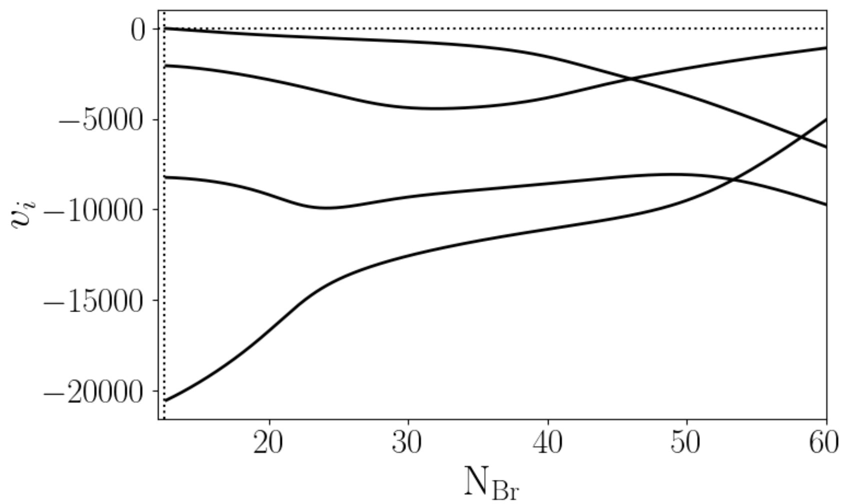

Figure 4.3. The real part of the four eigenvalues of the traveling wave solution's stability matrix $\boldsymbol{S}$.

The evolution of the perturbation $\boldsymbol{\epsilon} = [\epsilon_x, \epsilon_y, \epsilon_z, \epsilon_p]^\top$ is given by $\dot{\boldsymbol{\epsilon}} = \boldsymbol{S}\boldsymbol{\epsilon}$, where the matrix $\boldsymbol{S}$ is given by

$$\boldsymbol{S} = \begin{bmatrix} a_1 - i\Omega + a_2 r_y & a_2 r_x + a_3 r_z & a_3 r_y + a_4 R r_p & a_4 r_z \\ b_2 r_z + 2b_4 r_x & b_1 - 2i\Omega + b_3 r_p & b_2 r_x & b_3 r_y \\ c_2 r_p + c_3 r_y & c_3 r_x & (c_1 - 3i\Omega) & c_2 r_x \\ d_2 r_z & 2d_3 r_y & d_2 r_x & d_1 - 4i\Omega \end{bmatrix}. \tag{4.8}$$

We find that the real part of the four eigenvalues of $\boldsymbol{S}$, given by $\{v_i = \mathrm{Re}\,[\,\mathrm{eig}(\boldsymbol{S})]\}_{i=1,2,3,4}$, shown in Fig. 4.3, are always negative for the range of parameters considered in this study, which indicates that the traveling wave is on the stable solution branch of the dynamical system. This result agrees with the stability diagram numerically investigated in Chapter 2, wherein the traveling wave profiles were found to be local attractors. Also, while Chapter 2 studied the stability of the droplet profile in the physical domain, the current study revises and verifies the result in the Fourier domain.

The bifurcation of the amplitude r_x with increasing $\mathrm{N_{Br}}$ is shown in Fig. 4.2. A stable limit cycle emerging from the trivial solution beyond a critical value of the parameter is, of course, the familiar Hopf bifurcation. The limit cycle is the traveling wave solution with complex amplitude rotating at a constant speed Ω, which is also seen in Fig. 4.1. Next, we wish to understand the details and implications of this Hopf bifurcation of the ferrofluid droplet's interface dynamics.

4.3 Supercritical Hopf bifurcation

The system (4.1) of four complex-valued nonlinear ODEs is challenging to analyze. Instead, to determine the properties of the observed bifurcation, we consider the reduced, two-mode system (4.5). This reduction is supported by the fact that, around the critical point (*i.e.*, for weak nonlinearity), the dynamics can be well approximated by a small number of harmonic modes. Indeed, the fully nonlinear simulation in Fig. 4.4(*a*,*b*) shows that, around the critical point (here, $\mathrm{N_{Br}} = 12.5$ when $\mathrm{Re}(a_1) = 0$), the dynamics involves effectively only two harmonic modes (the fundamental mode $k = k_f = 7$ and its harmonic $k = 2k_f = 14$). For larger $\mathrm{N_{Br}}$, the "strength" of the instability also increases (since a_1 increases with $\mathrm{N_{Br}}$), and nonlinearity leads to the interaction of multiple harmonics modes, as seen in Fig. 4.4(*c*). However, around the critical point, as in Fig. 4.4(*a*,*b*), the system (4.5) captures the leading-order behavior.

The linearization of the system (4.5) around the fixed point $(x, y) = (0, 0)$ is simply

$$\dot{x} = a_1 x, \qquad \dot{y} = b_1 y. \tag{4.9}$$

Thus, the dynamics of x and y are decoupled. We are only interested in leading mode, for which we have:

$$\dot{x}_r = \mathrm{Re}(a_1)x_r - \mathrm{Im}(a_1)x_i, \tag{4.10a}$$

$$\dot{x}_i = \mathrm{Re}(a_1)x_i + \mathrm{Im}(a_1)x_r, \tag{4.10b}$$

where $x_r = \mathrm{Re}(x)$ and $x_i = \mathrm{Im}(x)$. The linearized system (4.10) has a pair of eigenvalues $\lambda_\pm = \mathrm{Re}(a_1) \pm i\,\mathrm{Im}(a_1)$. Thus, the non-hyperbolicity condition (*i.e.*, that one conjugate pair of imaginary eigenvalues exist at the critical point when $\mathrm{Re}(a_1) = 0$ and $\mathrm{Im}(a_1) \neq 0$), and the transversality condition (*i.e.*, that $\partial\,\mathrm{Re}(a_1)/\partial \mathrm{N_{Br}} \neq 0$) of the Hopf bifurcation are easily verified. To satisfy the genericity condition, however, the first Lyapunov coefficient needs to also be shown to be negative [126], such that the limit cycle is orbitally stable. However, the calculation of this coefficient is not trivial for higher-dimensional systems [126], [127]. Instead, we turn to the center manifold method to further reduce the dimensionality of the system (4.5) near the critical point and obtain a planar dynamical system.

4.3.1 Center manifold reduction

From the dynamics studied above, we expect the current system to have a parameter-dependent center manifold on which the system exhibits the Hopf bifurcation. In contrast, the behavior off the manifold is "trivial" (meaning that the leading mode dominates the dynamics).

A quadratic approximation is used to derive the finite-dimensional center manifold [126], [127]. Specifically, we assume the dynamics on the center manifold can be related by a scalar function $y = V(x, x^*)$. To quadratic order, its Taylor series is

$$V(x, x^*) = \frac{1}{2} g_{20} x^2 + g_{11} x x^* + \frac{1}{2} g_{02} x^{*2} + \mathcal{O}(|x|^3). \tag{4.11}$$

The unknown coefficient g_{20}, g_{11}, and g_{02} can be found by substituting (4.11) into the reduced system (4.5):

$$\dot{y} = V_x \dot{x} + V_{x^*} \dot{x}^* = a_1 g_{20} x^2 + 2\,\mathrm{Re}(a_1) g_{11} x x^* + a_1^* g_{02} x^{*2} + \mathcal{O}(|x|^3), \tag{4.12a}$$

$$\dot{y} = b_1 y + b_4 x^2 = \left(\frac{b_1}{2} g_{20} + b_4\right) x^2 + b_1 g_{11} x x^* + \frac{b_1}{2} g_{20} x^{*2} + \mathcal{O}(|x|^3). \tag{4.12b}$$

The equivalence of the two equations in system (4.12) at $\mathcal{O}(|x|^2)$ gives

$$g_{20} = 2b_4/(2a_1 - b_1), \text{ and } g_{11} = g_{02} = 0. \tag{4.13}$$

Thus, for the system (4.5) near its critical point $(x, y) = (0, 0)$, we find the center manifold to be:

$$\mathcal{W}_c = \left\{ (x, y) : y = V(x) = \frac{b_4}{2a_1 - b_1} x^2 \right\}. \tag{4.14}$$

Correspondingly, we have a locally topologically equivalent dynamical system [126]:

$$\dot{x} = a_1 x + \frac{a_2 b_4}{2a_1 - b_1}|x|^2 x, \tag{4.15a}$$

$$\dot{y} = 2a_1 y. \tag{4.15b}$$

Now, the equations for x and y are decoupled and Eq. (4.15a) is the restriction [126] of the system (4.5) to its center manifold $\mathcal{W}_c$. The dynamics of the system are essentially determined by this restriction, *i.e.*, Eq. (4.15a), since (4.15b) is linear and its dynamics is trivial. Indeed, as shown in Fig. 4.4, Eq. (4.15a) accurately captures the evolution of x from system (4.5) along the center manifold. It is also evident that Eq. (4.15a) even captures the original fully nonlinear system's dynamics (*i.e.*, Eqs. (2.2), (2.6), (2.3)). Further, the single ODE (4.15a) from the center manifold reduction also accurately predicts the permanent rotating droplet profile, especially near the critical point ($\mathrm{N_{Br}} = 12.5$ as in Fig. 4.4(a,b)).

Notably, it takes four steps of reduction to obtain the single ODE (4.15a) from the original Hele-Shaw problem. First, we performed the weakly nonlinear expansion (2.11) in the Fourier domain. Second, the weakly nonlinear expansion was truncated at a finite number of harmonic modes (four in the current study), to yield the system (4.1). Third, we approximated the system (4.1) by the two-harmonic-mode system (4.5) near the critical point. Fourth, along the center manifold, the system (4.5) becomes decoupled, and the leading mode's nonlinear evolution is accurately described by Eq. (4.15a). The second and third steps can be combined since they only depend on how many modes we wish to retain. In the physical system under consideration here, for weaker nonlinearity, a smaller number of interacting modes is present. Note that the system (4.5) can also be obtained by restricting the system (4.1) to its critical eigenspace $\{z = 0,\ p = 0\}$. This *tangent approximation* does not always guarantee topological equivalence [126], [127]. In the present problem, the specific meaning of the harmonic amplitudes, *i.e.*, x, y, z, p, and the long-wave instability feature of the Hele-Shaw problem ensure the tangent approximation is successful.

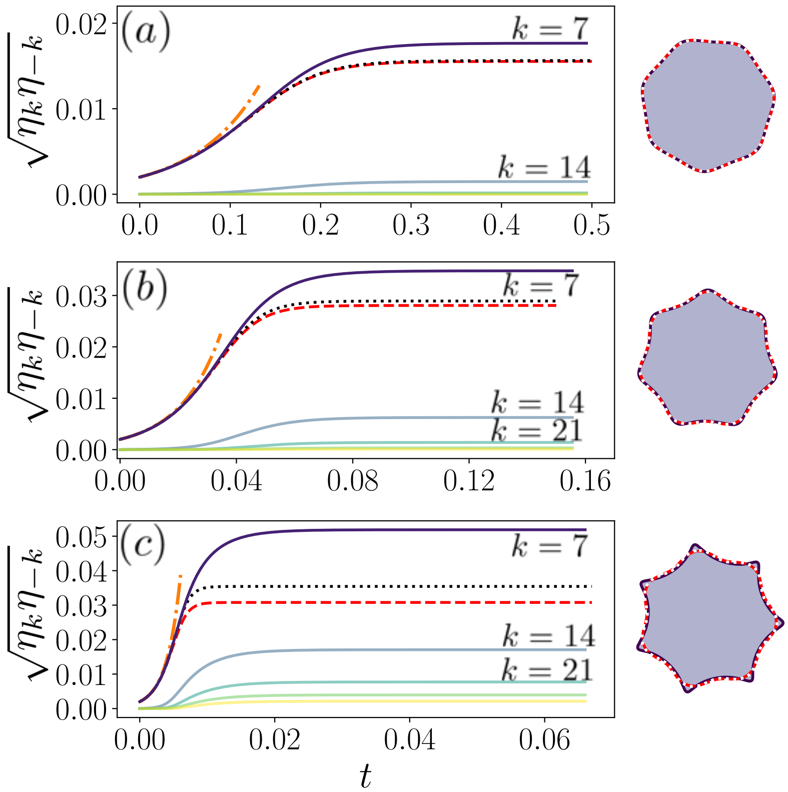

Figure 4.4. Comparison of leading modes' amplitude evolution for (a) $\mathrm{N_{Br}} = 13$, (b) $\mathrm{N_{Br}} = 15$, and (c) $\mathrm{N_{Br}} = 30$. Shown are the center manifold reduction solution from Eq. (4.15) (black dotted curve), the multiple-time-scale analysis solution from Eq. (4.29) (red dashed curve), and the fully nonlinear simulation (solid curves). The orange dash-dotted curve shows the unstable linear evolution. The corresponding permanent rotating droplet shapes are shown on the right, produced via a fully nonlinear simulation (purple solid), via the multiple-time-scale analysis (red dashed), and via the center manifold method (white dotted).

4.3.2 Normal form of the Hopf bifurcation

Let $a_1 = \mu + i\omega$ $(\omega < 0)$ and $\tau = -\omega t$, then Eq. (4.15a) can be rewritten as:

$$\frac{dx}{d\tau} = \left(-\frac{\mu}{\omega} - i\right) x + \frac{a_2 b_4}{-(2a_1 - b_1)\omega} |x|^2 x, \tag{4.16}$$

which is the normal form of a Hopf bifurcation [126] in which the motion along the limit cycle is counterclockwise. The rotation direction of our ferrofluid droplet is determined by the direction of the magnetic field's azimuthal component, and thus the sign of the imaginary part of the linear growth rate, as discussed in Chapter 2. This sign does not change the stability of the system. For a dynamical system in the form (4.16), the first Lyapunov coefficient can be directly computed as $\mathrm{Re}\left[\frac{a_2 b_4}{-(2a_1-b_1)\omega}\right]$, and shown to be always negative for the parameters chosen in this study. Thus, together with the condition $-\mu/\omega > 0$, the existence of a supercritical Hopf bifurcation is proven. The corresponding stable limit cycle has radius

$$r_x = \sqrt{\frac{-\mu}{\mathrm{Re}\left(\frac{a_2 b_4}{2a_1-b_1}\right)}}. \tag{4.17}$$

As expected, Fig. 4.2 shows that this radius can predict the amplitude of the traveling wave solution near the critical point of the system, *i.e.*, when the ferrofluid interface experiences weak nonlinearity.

Equation (4.16) reveals that the linearly unstable but nonlinearly stable interfacial dynamics of the confined ferrofluid interface emerge via a Hopf bifurcation. We expect that this analysis can also be applied to other Hele-Shaw problems involving interfacial dynamics characterized by long-wave instability, such as the configuration in [41]. For systems exhibiting a long-wave instability, a finite set of wavenumbers usually dominates the dynamics, and thus the truncation to a finite-dimensional space, in the Fourier domain, is fruitful, reducing the original infinite-dimensional partial differential equations to a low-dimensional system of ODEs. Furthermore, in the weakly nonlinear regime, the number of unstable modes can be controlled such that two-mode interaction (4.5) can be analyzed via a center manifold reduction, while still revealing important dynamical features of the original infinite-dimensional problem, which has nonlocal dynamics as already hinted by the vortex-sheet formulation of the problem [128].

The success of the center manifold reduction may appear surprising. The simple local equation (4.15a) successfully captures the nonlocal dynamics. This feature can be understood by considering the stationary pattern emerging from the balance of capillary and centrifugal forces, discussed by Álvarez-Lacalle *et al.* For the stationary pattern, imposing the zero vorticity condition, the vortex-sheet formulation is reduced to a single geometric ODE in space. The solution of this geometric ODE is the well-known family of *elasticas*. Álvarez-

Lacalle *et al.* build the connection between the elastica solutions of the Saffman–Taylor problem and the bifurcation analysis of interfacial growth problems. The unstable branch of the subcritical bifurcation diagram obtained from their amplitude equation is similar to Eq. (4.15a) herein. It is interesting to note that while Ref. [99] shows the linearly stable modes in the Saffman–Taylor problem are generically nonlinearly unstable (characterized by a subcritical bifurcation), the current study finds patterns that are nonlinearly stable (characterized by a supercritical bifurcation), even if linearly unstable. However, even though the vortex-sheet formulation of the problem from [99] and the present study are similar, a geometric ODE providing exact solutions cannot be obtained in the current work due to the dynamic nature (*i.e.*, the nonzero interface velocity and local vorticity).

Although the proposed model reduction process, starting with the leading-order weakly nonlinear approximation and followed by the center manifold calculation, looks straightforward, it does not mean that the Hopf bifurcation result follows trivially. First, a complex linear growth rate is necessary such that, near the critical point of the system, a simple pair of complex-conjugate eigenvalues cross the imaginary axis when varying the controllable bifurcation parameter. The latter ensures the satisfaction of the non-hyperbolicity and transversality conditions. For example, when the linear growth rate is purely real (*e.g.*, when the interface is subjected to only a radial magnetic field as in [27], [36]), a supercritical pitchfork bifurcation can be expected, from which a *static* gear-like pattern emerges. In comparison, the propagating interfacial wave, driven by the tilted magnetic field introduced in [41], is expected to be governed by a Hopf bifurcation. In addition, it must be properly shown that the physical configuration and parameters yield a negative first Lyapunov coefficient, which ensures that a stable limit cycle emerges from the bifurcation.

Another possibility is a *dynamical* bifurcation, such as a *delayed* bifurcation [129], [130]. In a delayed Hopf bifurcation, the dynamics is infinitesimally slow with respect to the bifurcation parameter. The real part of the linear growth rate is initially negative until a critical time, thereupon becoming positive, which causes the solution to abruptly begin to rotate with a large amplitude. Next, we would like to understand if a delayed bifurcation can be observed in the confined ferrofluid droplet problem. Further, we would like to determine how well the critical (delay) time can be approximated. To answer these questions, we first conduct a multiple-time-scale analysis of Eq. (4.5). Then, we analyze a time-dependent problem with a slow-varying bifurcation parameter.

4.4 Multiple-time-scale analysis

Multiple-time-scale analysis allows for the calculation of the leading effect of nonlinearity on the propagation of a harmonic wave [112]. Following the approach used in Section 3.4.1, to begin the multiple-time-scale analysis we perturb the bifurcation parameter with $a_1 = \epsilon^2\varkappa + i\omega$ around its critical value $\mathrm{Re}(a_1) = 0$, where again $\epsilon \ll 1$ is a small perturbation parameter, and $\varkappa > 0$ is independent of ϵ. The assumption that the linear growth rate is much smaller than the oscillation rate, *i.e.*, $\epsilon \ll 1$ is supported by Fig. 4.1, in which the envelope and oscillations are clearly evolving on disparate time scales. This perturbation makes the leading mode marginally unstable and also the only unstable mode of the system. We first rescale Eq. (4.5) to a small amplitude problem via $x \mapsto \epsilon x$ and $y \mapsto \epsilon y$:

$$\dot{x} = (\epsilon^2\varkappa + i\omega)x + \epsilon a_2 x^* y, \tag{4.18a}$$

$$\dot{y} = b_1 y + \epsilon b_4 x^2. \tag{4.18b}$$

Then, we assume that x and y have multiple-time-scale pertubation expansions in the form:

$$x(t, T_1) = x_0(t, T_1) + \epsilon x_1(t, T_1) + \epsilon^2 x_2(t, T_1) + \mathcal{O}(\epsilon^3), \tag{4.19a}$$

$$y(t, T_1) = y_0(t, T_1) + \epsilon y_1(t, T_1) + \epsilon^2 y_2(t, T_1) + \mathcal{O}(\epsilon^3). \tag{4.19b}$$

The slow time scale is $T_1 = \epsilon^2 t$, and the time derivative transforms as $\dot{(\cdot)} = d(\cdot)/dt = \partial(\cdot)/\partial t + \epsilon^2 \partial(\cdot)\partial T_1$. Substituting the time derivative and the expansion (4.19) into the small amplitude equation (4.18) gives rise to the system:

$$\left(\frac{\partial}{\partial t} + \epsilon^2 \frac{\partial}{\partial T_1}\right)(x_0 + \epsilon x_1 + \epsilon^2 x_2) = (\varkappa \epsilon^2 + i\omega)(x_0 + \epsilon x_1 + \epsilon^2 x_2) + \epsilon a_2 (x_0^* + \epsilon x_1^* + \epsilon^2 x_2^*)(y_0 + \epsilon y_1 + \epsilon^2 y_2), \tag{4.20a}$$

$$\left(\frac{\partial}{\partial t} + \epsilon^2 \frac{\partial}{\partial T_1}\right)\left(y_0 + \epsilon y_1 + \epsilon^2 y_2\right) = b_1 (y_0 + \epsilon y_1 + \epsilon^2 y_2) + \epsilon b_4 (x_0 + \epsilon x_1 + \epsilon^2 x_2)^2. \tag{4.20b}$$

By collecting terms at $\mathcal{O}(1)$, we obtain the leading-order equation (4.21)

$$\frac{\partial x_0}{\partial t} - i\omega x_0 = 0, \tag{4.21a}$$

$$\frac{\partial y_0}{\partial t} - b_1 y_0 = 0, \tag{4.21b}$$

which has a solution of the form

$$x_0(t, T_1) = A_x(T_1) e^{i\omega t}, \tag{4.22a}$$

$$y_0(t, T_1) = A_y(T_1) e^{b_1 t}, \tag{4.22b}$$

subjected to the initial conditions $x_0(0,0) = A_x(0) = X$, $y_0(0,0) = A_y(0) = Y$, where $X, Y \in \mathbb{C}$.

Then, at $\mathcal{O}(\epsilon)$, the equation is

$$\frac{\partial x_1}{\partial t} - i\omega x_1 = a_2 x_0^* y_0 = a_2 A_x^* A_y e^{(b_1 - i\omega)t}, \tag{4.23a}$$

$$\frac{\partial y_1}{\partial t} - b_1 y_1 = b_4 x_0^2 = b_4 A_x^2 e^{2i\omega t}, \tag{4.23b}$$

which can be solved as

$$x_1 = \frac{a_2}{b_1 - 2i\omega}\left(A_x^* A_y e^{(b_1 - i\omega)t} - X^* Y e^{i\omega t}\right), \tag{4.24a}$$

$$y_1 = \frac{-b_4}{b_1 - 2i\omega}\left(A_x^2 e^{2i\omega t} - X^2 e^{b_1 t}\right), \tag{4.24b}$$

with initial condition $x_1(0,0) = 0,\ y_1(0,0) = 0$.

Finally, at $\mathcal{O}(\epsilon^2)$, we have

$$\frac{\partial x_2}{\partial t} - i\omega x_2 = -\frac{\partial x_0}{\partial T_1} + \varkappa x_0 + a_2(x_0^* y_1 + x_1^* y_0), \tag{4.25a}$$

$$\frac{\partial y_2}{\partial t} - b_1 y_2 = -\frac{\partial}{\partial T_1} y_0 + 2b_4 x_0 x_1, \tag{4.25b}$$

with initial condition $x_2(0,0) = 0,\ y_2(0,0) = 0$. The nonlinear term in Eq. (4.25a) can be calculated as:

$$\begin{aligned} x_0^* y_1 + x_1^* y_0 \quad &= \quad A_x^* e^{-i\omega t}\left[\frac{-b_4}{b_1 - 2i\omega}(A_x^2 e^{2i\omega t} - X^2 e^{b_1 t})\right] \\ &+ \quad A_y e^{b_1 t}\left[\frac{a_2^*}{b_1^* + 2i\omega}(A_x A_y^* e^{(b_1^* + i\omega)t} - XY^* e^{-i\omega t})\right]. \end{aligned} \tag{4.26}$$

To eliminate the secular term, we require that

$$-\frac{\partial x_0}{\partial T_1} + \varkappa x_0 + \frac{a_2 b_4}{2i\omega - b_1} A_x^* A_x^2 e^{i\omega t} = 0, \tag{4.27}$$

which yields the amplitude equation

$$\frac{dA_x}{dT_1} = \varkappa A_x + \frac{a_2 b_4}{2i\omega - b_1}|A_x|^2 A_x. \tag{4.28}$$

The complex amplitude $A_x(T_1)$ describes the slow temporal modulation of the base periodic (harmonic wave) solution.

Let $A_x(T_1) = \alpha(T_1) e^{i\beta(T_1)}$, where $\alpha, \beta \in \mathbb{R}$, then the real part of the amplitude equation (4.28) is

$$\frac{d\alpha}{dT_1} = \varkappa\alpha + Q\alpha^3, \tag{4.29}$$

where we defined $Q = \mathrm{Re}(\frac{a_2 b_4}{2i\omega - b_1})$. The amplitude equation (4.29) is also known as the *Landau equation* [131]. Unsurprisingly, equation (4.29) agrees with the center manifold reduction (4.15a). The only difference is the denominator of Q. In the case of Eq. (4.15a), the derivation is limited to dynamics near the critical point, *i.e.*, in the neighborhood of

$\mathrm{Re}(a_1) = 0$ with $\mathrm{Re}(a_1) > 0$ (see [126]), thus a_1 appears in the equation. Meanwhile, Eq. (4.29) is derived by separating the real part $\varkappa$ and imaginary part ω of a_1 into different orders of ϵ, such that there is only $i\omega$ in the denominator of Q. However, this difference is trivial. As seen in Fig. 4.2, the difference between the traveling wave amplitudes computed from Eq. (4.29) and Eq. (4.15a) are barely distinguishable. Importantly, Eqs. (4.15a) and (4.29) are asymptotically equivalent as $\mathrm{Re}(a_1) \to 0$ (at the critical point).

4.5 Time-dependent problem

A central question concerning pattern formation in time-dependent systems is how unsteady external forces affect the phase space structures and their evolution. This question is somewhat analogous to the question of how the quasistatic variation of a bifurcation parameter affects local attractors. The key insight is provided by the supercritical Hopf bifurcation, for which the instability onset (when the solution is repelled from the equilibrium) occurs later than the instant when the equilibrium loses its stability.

Above, we have shown that the amplitude equation (4.29) can predict the permanent rotating shape (traveling wave profile) seen in the nonlinear simulations of the confined ferrofluid droplet. Now, we move on to the question of dynamics: using the bifurcation delay feature to dynamically control the time evolution of the interface.

To start, we first reconsider the amplitude equation (4.29) for time-varying magnetic fields. Above, we took $a_1 = \epsilon^2\varkappa + i\omega$, where $\varkappa \in \mathbb{R}$. Now, instead, consider the slowly-varying time-dependent real growth rate $\varkappa = \varkappa(T_1) = \varkappa_0 + IT_1$, and thus

$$a_1 = a_1(T_1) = \epsilon^2(\varkappa_0 + IT_1) + i\omega, \tag{4.30}$$

where $\epsilon^2\varkappa_0$ is the small initial growth rate, which can be either positive or negative. Here, $\epsilon^2 I$ is the slow evolution rate of $\mathrm{Re}(a_1)$ on the long time scale T_1, *i.e.*, $d\ \mathrm{Re}(a_1)/dT_1 = \epsilon^2 I$. Physically, the linear variation of a_1 with T_1 can be achieved by controlling the combination of azimuthal and radial magnetic field strengths, or $\mathrm{N_{Ba}}(t)$ and $\mathrm{N_{Br}}(t)$, respectively. For example, we can take $\mathrm{N_{Ba}} = 1$ and set $\mathrm{N_{Br}}(t)$ to be a suitable linear function of time.

Next, the amplitude equation (4.29) can be shown, via the same analysis as before, to take the form:

$$\frac{d\alpha}{dT_1} = (\varkappa_0 + IT_1)\alpha + Q\alpha^3, \tag{4.31}$$

and its solution is given by

$$\alpha(T_1) = \exp\left(\varkappa_0 T_1 + \tfrac{1}{2}IT_1^2\right) \times \left[\left(-Q\sqrt{\frac{\pi}{I}}e^{\frac{-\varkappa_0^2}{I}}\right)\operatorname{erfi}\left(\frac{\varkappa_0 + IT_1}{\sqrt{I}}\right) + c\right]^{-1/2}, \tag{4.32}$$

where $c = 1/X^2 + Q\sqrt{\pi/I}e^{-\varkappa_0^2/I}\operatorname{erfi}(\varkappa_0/\sqrt{I})$ is a constant related to the initial value $X = \alpha(T_1 = 0)$. The imaginary error function erfi is defined via $\operatorname{erfi}(z) = -i\operatorname{erf}(iz)$ [132].

The solution (4.32) for $\varkappa_0 < 0$ is shown in Fig. 4.5(a). For $T_1 < T_c$, the linear growth rate is such that $\mathrm{Re}(a_1) < 0$, and the initial small perturbation decays, as shown in the inset. At $T_1 = T_c$, $a_1(T_c) = 0$ and the equilibrium loses its linear stability. Now, the amplitude starts to grow, yet it remains infinitesimally small with respect to the initial perturbation. Next, at $T_1 = T_{\text{exit}}(> T_c)$, the initial perturbation amplitude is recovered, and now the solution starts to repel from the initial state. Subsequently, the amplitude increases abruptly due to the positive linear growth rate. This exponential increase is also observed in the time-independent problem, as shown in Fig. 4.4, which is followed by the saturation of the energy ($i.e.$, emergence of the permanent traveling wave profile).

Under the proposed time-dependent field, the exponential increase is followed by a slow increase, which is identified as the quasistatic region, in which the solution slowly varies with the bifurcation parameter. As seen from Fig. 4.5(a), the time-dependent solution (4.32) saturates to the quasistatic solution

$$\alpha_s = \sqrt{\frac{\varkappa_0 + IT_1}{-Q}}, \tag{4.33}$$

which is obtained by setting $d\alpha/dT_1 = 0$ in Eq. (4.31). This saturation can be intuitively understood as the balance of the exponential factor $e^{IT_1^2/2}$ and the decay factor $\operatorname{erfi}[(\varkappa_0 + IT_1)/\sqrt{I}]^{-1/2}$ as $T_1 \to \infty$ in the time-dependent solution (4.32). This balance also provides the possibility of predicting the delay time T_e analytically.

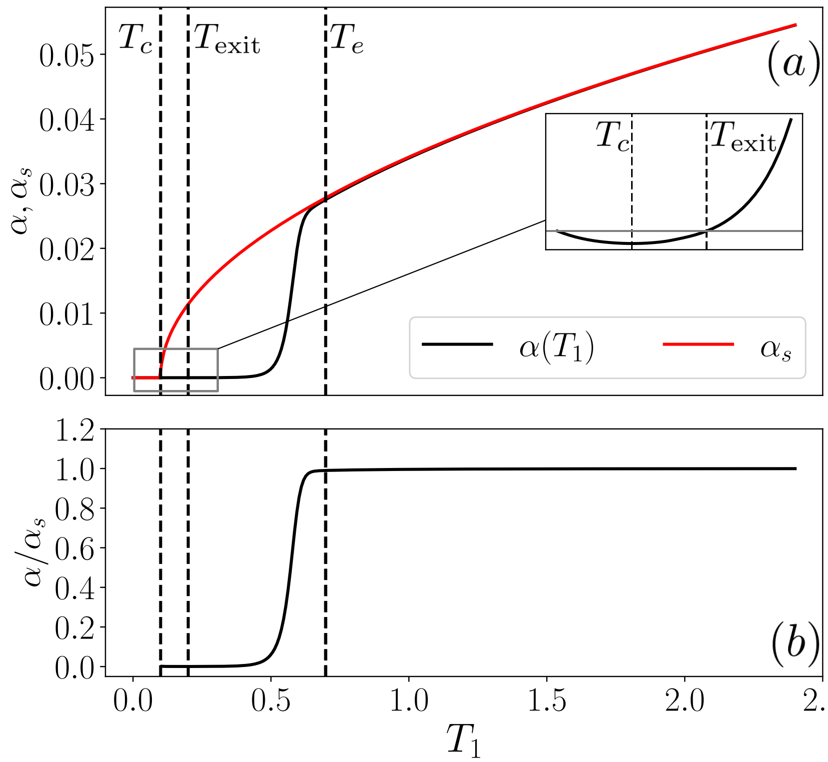

Figure 4.5. (a) The solution $\alpha(T_1)$ from Eq. (4.32) (black) saturates to the quasistatic solution α_s from Eq. (4.33) (red) as T_1 increases. (b) The ratio α/α_s approaches 1 during the same time period. Here, T_e denotes the time when $\alpha/\alpha_s = \rho = 0.99$. The remaining parameters are taken as $\varkappa_0 = -7.5$, $I = 75$, and the initial condition is $X = 5 \times 10^{-6} \ll 1$.

4.5.1 Approximation of the bifurcation delay time

To approximate the delay time T_e, we consider the equation

$$\frac{\alpha(T_e)}{\alpha_s(T_e)} = \rho, \tag{4.34}$$

such that when $T_1 > T_e$, $\alpha/\alpha_s > \rho$. In this study, we take $\rho = 0.99$ without loss of generality. Now, we would like to determine T_e from Eq. (4.34) and establish the quality of this approximation. To this end, we use the quasistatic solution (4.33) and time-dependent solution (4.32) to calculate the ratio

$$\frac{\alpha_s^2}{\alpha^2} = 1 + \frac{1}{2}\frac{I}{\varkappa^2} - \left(\frac{1}{QX^2}e^{\varkappa_0^2/I}\right)e^{-\varkappa^2/I}R + \mathcal{O}(\varkappa^{-4}), \tag{4.35}$$

where the expansion is valid for $\varkappa = \varkappa_0 + IT_1 \to \infty$. The following expansion of the imaginary error function at infinity (as $|z| \to \infty$) [132] has been used:

$$\mathrm{erfi}(z) = \frac{e^{z^2}}{\sqrt{\pi}}\left(z^{-1} + \frac{1}{2}z^{-3} + \frac{3}{4}z^{-5} + \cdots\right) - i. \tag{4.36}$$

Further, the coefficient $\sqrt{\pi/I}\left[\mathrm{erfi}\left(\varkappa_0/\sqrt{I}\right) + i\right]$ of the exponentially decaying term $e^{-\varkappa^2/I}\varkappa$ is neglected when compared to terms of $\mathcal{O}(1/X^2)$ for $X \ll 1$.

Note that Eq. (4.33) is valid only if $\varkappa_0 + IT_1 > 0\ \forall T_1$, *i.e.*, $\varkappa_0 > 0$. Thus, when $\varkappa_0 > 0$, the time T_e can be evaluated via Eqs. (4.35) and (4.34). Specifically, T_e solves

$$1 + \frac{I}{2}\frac{1}{(\varkappa_0 + IT_e)^2} + \frac{\varkappa_0 + IT_e}{-Q}\frac{1}{X^2}e^{-(2\varkappa_0 T_e + IT_e^2)} \approx \frac{1}{\rho^2}, \tag{4.37}$$

For $\varkappa_0 < 0$, T_e can instead be written as $T_e = T_c + T_{e,2}$, where $T_c = -\varkappa_0/I$ is the critical time defined by requiring a vanishing linear growth rate ($\varkappa(T_c) = 0$). When $T_1 < T_c$, $\varkappa < 0$, and perturbations decay. Thus, we can use the approximation $d\alpha/dT_1 = (\varkappa_0 + IT_1)\alpha$. At $T_1 = T_c$, the initial perturbation X decreases to its minimum value of α_c, where

$$\alpha_c = X\exp\left(\int_0^{T_c} \varkappa_0 + IT_1\, dT_1\right) = Xe^{-\varkappa_0^2/(2I)}. \tag{4.38}$$

For $T_1 > T_c$, $\varkappa > 0$, Eq. (4.37) can be used to evaluate $T_{e,2}$, by substituting $X_2 = \alpha_c$ as the initial value and $\varkappa_{0,2} = 0$.

When $X^2 \gg \frac{2}{-QI}(\varkappa + IT_e)^3 e^{-(2\varkappa_0 T_e + IT_e^2)}$, the effect of the initial perturbation amplitude is no longer important, and the delay time can be explicitly predicted by

$$T_e \approx \frac{\rho}{\sqrt{2I(1-\rho^2)}} - \frac{\varkappa_0}{I}, \tag{4.39}$$

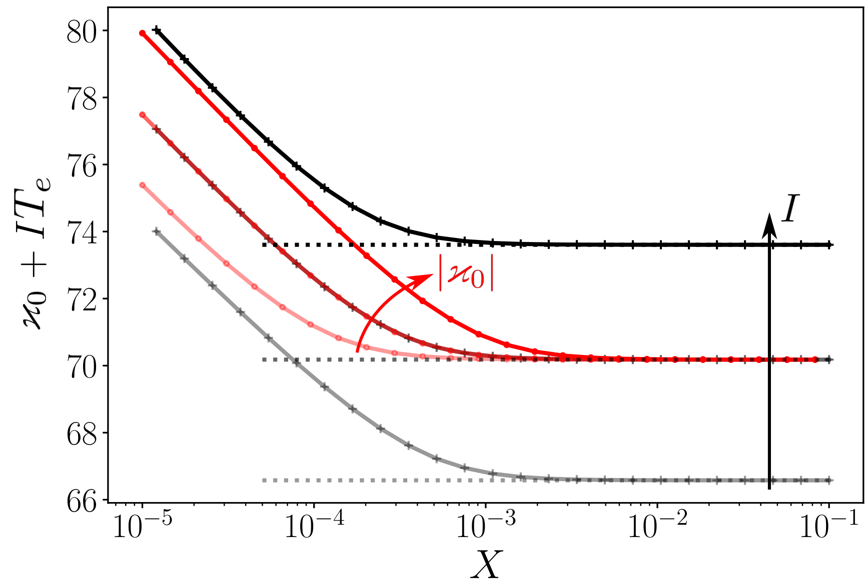

Figure 4.6. Dependence of $\varkappa_0 + IT_e$ on the initial perturbation strength X, based on the prediction of the delay time T_e via Eq. (4.37). The black curve with '+' markers represents the predicted time for different values of $I = 180, 200, 220$, with an arrow pointing in the direction of increasing I. The red curve with '∘' markers represents the predicted time for different values of $\varkappa_0 = -35, -40, -45$. The dotted horizontal lines denote the asymptotic values of $\sqrt{I\rho^2/2(1-\rho^2)}$.

or $\varkappa = \varkappa_0 + IT_e = \sqrt{I\rho^2/2(1-\rho^2)}$. As shown in Fig. 4.6, for fixed $\varkappa_0$ and I, the delay time T_e first decreases as the initial perturbation increases, and then starts to saturate (around 10^{-3}) to the value determined by $\varkappa_0$ and I only. Note that $\varkappa_0$ and I are controllable parameters corresponding to the external forces, and thus in the physical system, as long as the droplet is perturbed by a perceivable amplitude (say, $> 0.1\%$ of its initial radius), the delay time can be explicitly computed/controlled via Eq. (4.39).

Figure 4.7 shows that the delay time T_e evaluated from Eq. (4.37), based on the physical parameters and initial perturbation can predict the bifurcation delay. Further, it is evident that this prediction compares favorably with the delayed time observed in the multiple-time-scale analysis and the fully nonlinear simulations. For example, T_e can be taken as the minimum time needed for the time-dependent evolution to saturate to a predictable stationary state. When $T_1 < T_e$, the dynamics is governed by exponential growth or decay.

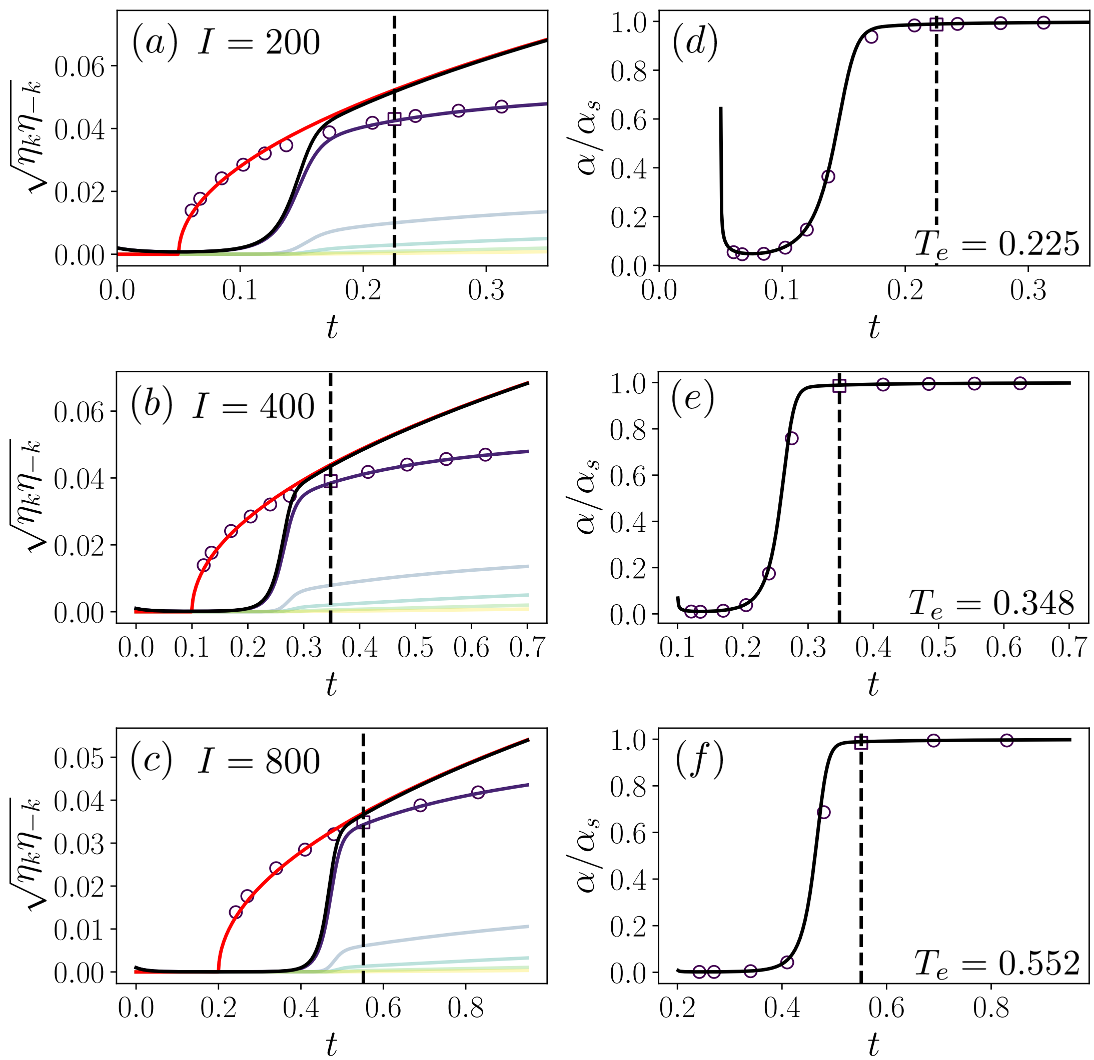

Figure 4.7. The delay time prediction (marked by the vertical dashed line) from the multiple-time scale analysis, compared to the fully nonlinear simulations. In (a,b,c), the black (resp. purple) curves show the leading mode's amplitude evolution from the multiple-time-scale analysis (resp. fully nonlinear simulations). The red curves (resp. purple circles) show the stationary solution for the corresponding $a_1(t)$ from the multiple-time-scale analysis (resp. fully nonlinear simulations). The amplitude ratio of the time-dependent evolution and the corresponding stationary solution is shown in (d,e,f), with the black curve (resp. purple circles) denoting the ratio from the multiple-time-scale analysis (resp. fully nonlinear simulations).

Subsequently, the amplitude experiences limited growth constrained by nonlinearity. Finally, when $T_1 > T_e$, the dynamics saturate to a state governed by the balance of nonlinearity and dispersion, and the interface evolution is determined by the quasistatic variation of the bifurcation parameter, *i.e.* the system responds to the (slow) external forcing instantaneously.

Figure 4.8 shows fully nonlinear simulation examples using the value of T_e to control the droplet's evolution. The azimuthal field's strength is fixed via $\mathrm{N_{Ba}} = 1$, and the radial field's strength, set by $\mathrm{N_{Br}}$, is determined through $a_1 = \varkappa_0 + It$ for $t \leq T_{\mathrm{off}}$. For $T_1 > T_{\mathrm{off}}$, $\mathrm{N_{Br}}(T_1) = \mathrm{N_{Br}}(T_{\mathrm{off}})$, *i.e.*, both fields are static. Figure 4.8 shows three cases, for different values of T_{off} but with the same initial perturbation strength $X = 0.001$, and the same physical parameters (corresponding to $I = 400$, $\varkappa_0 = -40$). In Fig. 4.8(a) $T_{\mathrm{off}} < T_e$. In this case, the radial field's strength stops increasing when the droplet amplitude is still in the linear regime, so it grows exponentially. In Fig. 4.8(b,c), $T_{\mathrm{off}} \geq T_e$, and the radial field's strength stops increasing when the droplet begins to settle into the permanent rotating state. Note that, while T_e is calculated through the multiple-time-scale analysis (which is a reduced model involving only two harmonic modes), it can still effectively capture the saturated state from the fully nonlinear simulations. The delay time T_e can be controlled via an external magnetic field, which allows targeting the shape of the droplet, by evaluating the quasistatic solution $\alpha_s = \sqrt{-\varkappa/Q}$ with the linear growth rate $\varkappa$ at the targetted time T_{off}.

4.5.2 Irreversible dynamics under a time-reversed magnetic field

In the classic film *Low Reynolds Number Flows* [133], G. I. Taylor explained the physical meaning of reversibility — "low Reynolds number flows are reversible when the direction of motion of the boundaries, which gave rise to the flow, is reversed." The reversibility of Stokes flow is due to its steadiness and the fact that inertial forces are negligible. In this time-independent flow, the time-reversed problem solves the same equations as the original Stokes flow. These equations are linear in Taylor's example of Couette flow. The reversed fluid flow is the result of reversing the direction of the external forcing (rotation of the cylinder in the Couette flow example shown by Taylor). The reversibility is at first surprising, as it can be

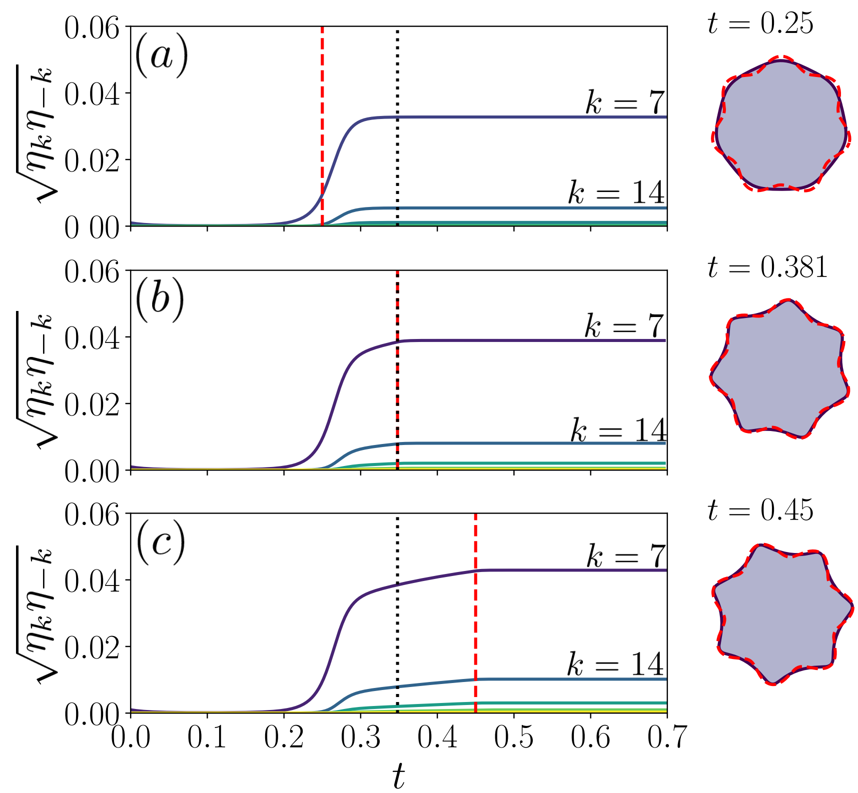

Figure 4.8. Control of the rotating droplet shapes (via the amplitude of the interfacial traveling wave) for (*a*) $T_{\text{off}} = 0.25$, (*b*) $T_{\text{off}} = T_e \approx 0.348$, and (*c*) $T_{\text{off}} = 0.45$. The curves show the leading mode's amplitude evolution from the fully nonlinear simulations. The red dashed vertical line denotes the turn-off time T_{off}; the black dotted vertical line denotes the delay time prediction T_e. The colored droplets are the real-time profiles from the fully nonlinear simulations (up to the corresponding times), and the red dashed outlines show the targetted profiles evaluated via Eq. (4.33). Here, $I = 400$, $X = 0.001$, $\varkappa_0 = -40$, and $\mathrm{N_{Ba}} = 1$, which are also the values used to evaluate T_e. For the convenience of the comparison, $\epsilon = 1$ is taken such that T_1 and t can be plotted at the same time scale. All other parameters are determined through Eq. (2.13) and Appendix 4.1.

used to show that the initial state of the fluid is recovered under flow reversal, which in some ways may contradict intuition based on observations of everyday fluid flows.

In this study, the original problem is a Hele-Shaw flow, which in general is also expected to be reversible like a Stokes flow. Yet, the reversibility of the dynamics of the confined ferrofluid droplet is not an obvious consequence because nonlinearity arises from the surface forces (capillary tension and magnetic traction) acting on the fluid–fluid interface. The interface is also subjected to unsteady forcing by the time-dependent external magnetic field. And, thus, time-reversing the magnetic field strengths does not return the fluid interface back to its initial shape. This irreversibility is demonstrated in Fig. 4.9, in which the fully nonlinear simulations show the perturbation amplitude upon time-reversing the magnetic field can be (a) smaller, (b) similar, or (c) larger than the initial perturbation.

The reversed process is initialized with the final state (T_f, α_f) from the forward process, then $\mathrm{N_{Ba}} = 1$ is fixed, and $\mathrm{N_{Br}}$ is manipulated such that the linear growth rate decreases linearly. Specifically, $\Upsilon = \mathrm{Re}(a_1) = \Upsilon_0 - IT_1$, where $\Upsilon_0 = \varkappa_0 + IT_f$. This protocol achieves the reversal process of the external field, and $\Upsilon(t) = \varkappa(T_f - t)$, $\forall t \in [0, T_f]$. Note that, while the magnetic field is reversed, the external forces are not. The magnetic surface force depends on the interface's shape, and the irreversible evolution of the interface implies the irreversibility of the external forces in this problem. Thus, it is of interest to determine how to evaluate $\Upsilon(T_f)$, if the initial state corresponding to $\varkappa(0)$ cannot be fully recovered in this irreversible system.

To answer this question, we first utilize Eq. (4.29) from the multiple-time-scale analysis to formulate the reverse problem as:

$$\frac{d\alpha}{dT_1} = (\Upsilon_0 - IT_1)\alpha + Q\alpha^3. \tag{4.40}$$

The solution for α can be calculated explicitly from

$$S(T_{1,a})\frac{1}{(\alpha_a)^2} + 2Q\tilde{S}(T_{1,a}) = S(T_{1,b})\frac{1}{(\alpha_b)^2} + 2Q\tilde{S}(T_{1,b}), \tag{4.41}$$

where the subscripts a, b denote two arbitrary states and

$$S(t) = e^{2\Upsilon_0 t - It^2}, \tag{4.42a}$$

$$\tilde{S}(t) = \int_0^t S(t')\,dt' = \frac{1}{2}\sqrt{\frac{\pi}{I}} e^{\Upsilon_0^2/I} \operatorname{erf}\left(\frac{It - \Upsilon_0}{\sqrt{I}}\right). \tag{4.42b}$$

Taking $T_{1,a} = 0$, $\alpha_a = \alpha_f$, then the reversed initial amplitude α_b can be predicted at $T_{1,a} = T_f$. One quick approximation can be made on finding the final state (T_f, α_f) when the forward evolution (4.31) enters the quasistatic region, *i.e.*, $T_f > T_e$, and the amplitude α_f can be approximated by Eq. (4.33).

Figure 4.9 shows a comparison of the forward and reversed processes approximated by Eqs. (4.31) and (4.40). In the quasistatic region, the evolution is close to reversible, after which the reverse evolution does not experience a sudden decrease in amplitude, which would parallel the rapid increase during the forward process. The cycling process under the fully nonlinear simulation shows similar dynamics. It is interesting to note that α_f from the simulation and Eq. (4.31) are different at $t = T_f$, yet the predictions of both during the reverse process eventually coincide in the small-t region, meaning that Eq. (4.40) provides a good approximation to the reversed "initial" amplitude.

This result is very similar to the one reported in the experimental work [134], wherein the peak of a magnetic fluid interface attains different amplitudes at the same field strength upon cycling the external magnetic field. This effect was attributed to the strong permeability of the ferrofluid. While in our work, the hysteresis-like behavior is mainly due to the time-dependent field's interaction with the interfacial nonlinearity, which is captured by the reduced models in Eq. (4.31) and Eq. (4.40). The difference between these evolution equations highlights the hysteresis-like behavior.

On the one hand, Eq. (4.40) provides a tool for predicting the time-reversed process. On the other hand, this equation also provides a new point of view on the observed irreversibility. Solutions to Eq. (4.31) in the (T_1, α) plane, and solutions to Eq. (4.40) in the $(T_f - T_1, \alpha)$ plane are two families of curves that intersect at (T_f, α_f). The initial condition (4.31) determines a certain curve in the forward family, along which any arbitrary (T_f, α_f) can be found as the

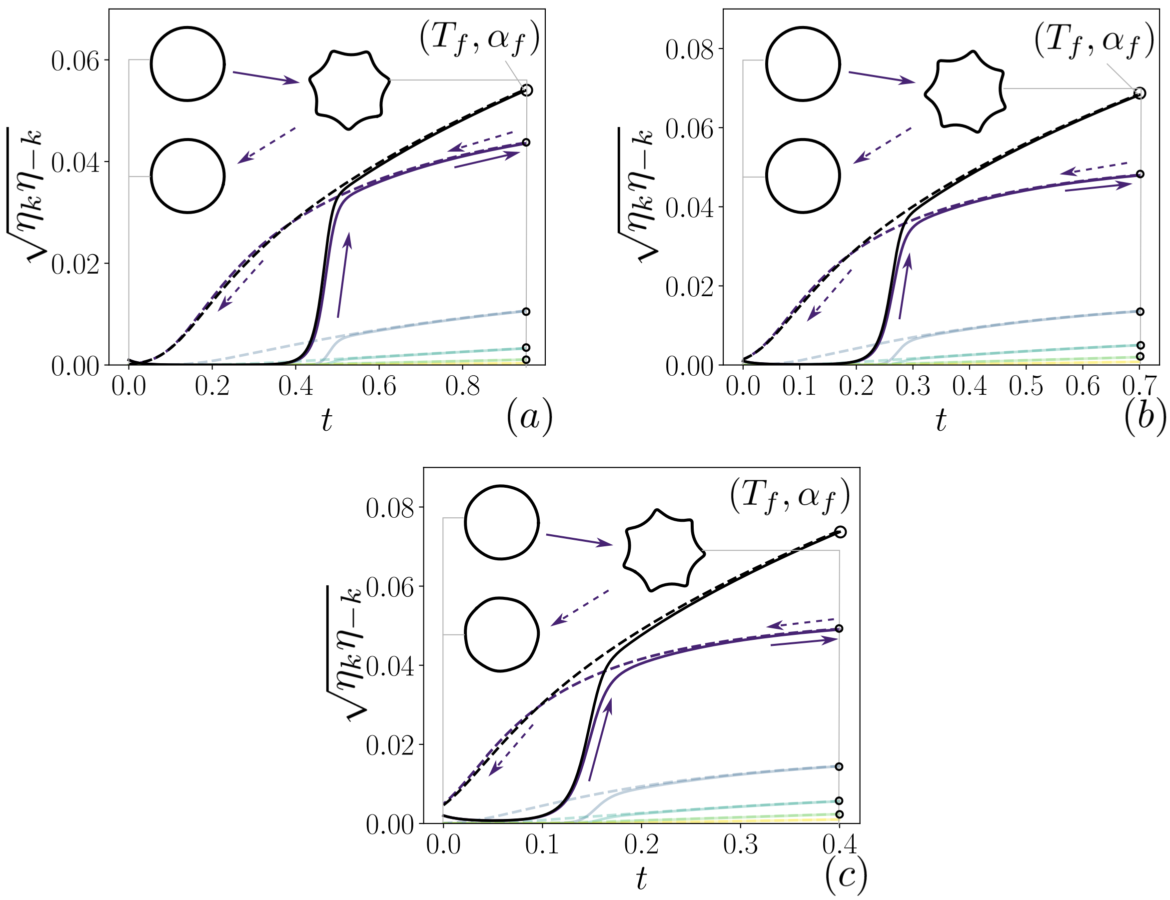

Figure 4.9. Dynamics under a reversed-time magnetic field: comparison of the prediction from the multiple-time-scale analysis and the fully nonlinear simulations. The solid (resp. dashed) curves show the forward (resp. reverse) process for which $\dot{\lambda}(k_f) > 0$ ($\dot{\lambda}(k_f) < 0$). The black (resp. purple) curve shows the leading mode amplitude evolution from the multiple-time scale analysis (resp. fully nonlinear simulations). The circle represents the (T_f, α_f) state. In (a), $T_f = 0.95$, $X = 0.001$, and $I = 200$. In (b), $T_f = 0.7$, $X = 0.001$, and $I = 400$. In (c), $T_f = 0.4$, $X = 0.002$, and $I = 800$. In all three simulations, $\varkappa_0 = -40$, and $\epsilon = 1$ is taken such that T_1 and t can be plotted at the same abscissa.

intersection point with the curve in the reverse family determined by Eq. (4.40). Importantly, these two curves intersect only at (T_f, α_f) and do not overlap.

4.6 Discussion

The intrinsic reason why a simple, local ODE can approximate the fully nonlocal dynamics is discussed, also in the context of the static problem considered in [99]. However, unlike the case in [99], we are unable to obtain a single curvature ODE for the dynamic problem, due to the difficulty of eliminating the nonlocal term from the vortex-sheet formulation of the full Hele-Shaw problem. This task remains an open question, specifically whether such a single curvature ODE even exists to exactly describe the family of traveling wave solutions discussed herein. To further understand that challenge, suppose that vortex elements on the interface are subjected to rigid rotation. In this case, a moving frame transformation would eliminate the relative velocity (and, thus, the nonlocal term). However, to perform a moving frame transformation, the exact traveling wave velocity needs to be found, which is still nontrivial. On the other hand, if the interface is not rotating as a rigid body, then the elements on the interface have some local rotation rate, which collectively leads to the interfacial wave. In this case, when the local velocity is nonuniformly distributed along the interface, a moving frame transformation may not exist. The success of the approximations in the present work might imply the existence of such a curvature equation, but how to obtain it is left as an open question. Answering this question would surely provide further examples of the relevance of elastica solutions.

In this work, the bifurcation parameter is controlled by a simple linear variation, which allows for the explicit analytical solution of the amplitude equation, and the approximation of the delay time. The linear variation with time is expected to be the simplest strategy that can be realized in experiments, as it only requires increasing the magnetic field strength at a constant rate. Thus, by explicitly predicting the delay time, our work enables the effective design of the target control. Further, the selection of a linear variation scheme requires minimal algebraic calculations to obtain a straightforward prediction.

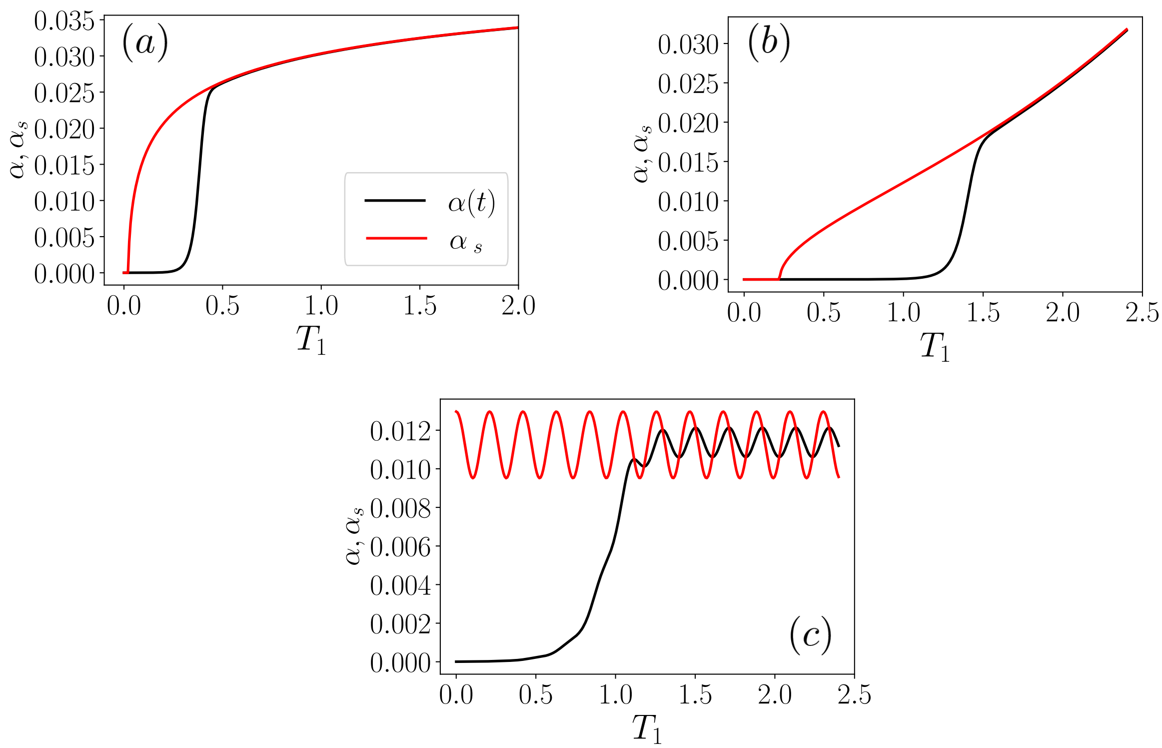

Figure 4.10. The time-dependent solution $\alpha(T_1)$ (black) and quasi-static solution α_s (red) evaluated from Eq. (4.29) with (a) $\varkappa = \varkappa_0 + 20\log(20T_1 + 1)$; (b) $\varkappa = \varkappa_0 + 0.08Ie^{T_1}$; and (c) $\varkappa = \varkappa_0 + 0.03I\cos(30T_1)$. $I = 75$ for all three cases, and $\varkappa_0 = 7.5$ for $(a{,}b)$, while $\kappa_0 = -7.5$ for (c).

Other control protocols, such as periodic forcing, can also be considered, providing a different view on the accumulation of the time-dependent evolution. We show three examples: a log-varying, an exponentially increasing, and an oscillating growth rate. We can observe that for a log-varying or an exponentially increasing growth rate, as in Fig. 4.10(a) and (b), respectively, α will saturate to the quasi-static solution α_s. This is not the case, however, for the oscillating growth rate shown in Fig. 4.10(c). This observation opens a series of follow-up questions: (i) How do we prove the saturation mathematically, and how do we obtain the explicit delay prediction like in Eq. (4.39)? (ii) How do we quantify the reliable prediction time range (since the exponential variation will quickly break down the slow-time-variation assumption)? (iii) How do we quantify the observed phase lag between the time-dependent solution and the quasi-static solution for an oscillating growth rate? These questions are left to future work.

The proposed reduction method can be generally applied to other interfacial problems governed by a finite number of harmonic modes. Our mode-reduction approach also allows for the effective and computationally inexpensive prediction of the dynamics, as well as for "reverse engineering" of time-dependent forcing schemes (*i.e.*, choosing a forcing that generates dynamics of interest), such as those aiming to achieve pattern stabilization [48] or self-similar evolution [47], [49] of fluids confined in Hele-Shaw cells.

4.1 Appendix: Coefficients for the reduced model

The coefficients in the system of ODEs (4.1) are

$$
\begin{aligned}
a_1 &= \Lambda(k),\\
a_2 &= F(k,-k) + F(k,2k) + G(k,-k)\Lambda(-k) + G(k,2k)\Lambda(2k),\\
a_3 &= F(k,-2k) + F(k,3k) + G(k,-2k)\Lambda(-2k) + G(k,3k)\Lambda(3k),\\
a_4 &= F(k,-3k) + F(k,4k) + G(k,-3k)\Lambda(-3k) + G(k,4k)\Lambda(4k),\\
b_1 &= \Lambda(2k),\\
b_2 &= F(2k,-k) + F(2k,3k) + G(2k,-k)\Lambda(-k) + G(2k,3k)\Lambda(3k),\\
b_3 &= F(2k,-2k) + F(2k,4k) + G(2k,-2k)\Lambda(-2k) + G(2k,4k)\Lambda(4k),\\
b_4 &= F(2k,k) + G(2k,k)\Lambda(k),\\
c_1 &= \Lambda(3k),\\
c_2 &= F(3k,-k) + F(3k,4k) + G(3k,-k)\Lambda(-k) + G(3k,4k)\Lambda(4k),\\
c_3 &= F(3k,k) + F(3k,2k) + G(3k,k)\Lambda(k) + G(3k,2k)\Lambda(2k),\\
d_1 &= \Lambda(4k),\\
d_2 &= F(4k,k) + F(4k,3k) + G(4k,k)\Lambda(k) + G(4k,3k)\Lambda(3k),\\
d_3 &= F(4k,2k) + G(4k,2k)\Lambda(2k),
\end{aligned}
$$

where the functions F and G are given in Eqs. (2.12).

5. MAGNETIC TORQUE-INDUCED WAVE PROPAGATION ON A FERROFLUID THIN FILM

SUMMARY

In this chapter, we extend our investigation to encompass fast-varying magnetic fields. Due to the magnetic relaxation, a phase lag arises between the magnetization and the magnetic field. Consequently, the linear magnetization assumption becomes invalid, resulting in the emergence of a magnetic torque density, which means that the spin velocity and vorticity no longer coincide. To study these new physical features, we develop a long-wave model that incorporates a rotating magnetic field. Separating the slow flow time scale from the fast magnetization relaxation time scale allows for an approximation of the magnetic torques and forces, and thus the decoupling of the flow equations from Maxwell's equations. A traveling-wave Dirichlet boundary condition is imposed on the magnetic scalar potential, which gives rise to the desired locally rotating magnetic field. Its spatial variation with the evolving interface is found by solving Maxwell's equations with an interface condition. The derived model incorporates a surface boundary condition that highlights a shear force originating from the surface torque. Through linear stability analysis, we identify the rotating field as a new mechanism that can be both destabilizing and lead to wave propagation. The linear stability predictions are subsequently verified through nonlinear simulations. The observed behaviors hint at the emergence of complex and highly nonlinear phenomena, such as the formation of "shock waves" and the transition to long-lasting "chaotic wave" states.

5.1 Mathematical model and governing equations

In Chapters 2 and 3, we have shown that a static magnetic field can be used to generate traveling waves on a ferrofluid interface, with predictable velocity. In Chapter 4, our work was expanded to explore the dynamics of ferrofluid interfaces subjected to a quasistatic field toward achieving real-time control. Beyond the focus in the previous chapters, it would also be of interest to consider the time-dependent interface control using a fast-varying magnetic field.

In a static magnetic field, the internal dipole moments of the nanoparticles in the ferrofluid align in the direction of the field. This process is referred to as magnetic relaxation. Usually, this process occurs immediately, and we assume the magnetization is instantaneously adjusted, being linearly proportional to the magnetic field $\mathbf{M} = \chi\mathbf{H}$. However, when the magnetic field changes on a time scale comparable to the magnetization relaxation time, a lag arises between the magnetization and the applied field, such that they are not collinear. Therefore, a body-torque density, given by $\mu_0\mathbf{M} \times \mathbf{H}$, is created.

To understand the most basic effect of the magnetic torque, we employ a two-dimensional configuration to derive a model in a Cartesian configuration. This configuration is simpler than a Hele-Shaw cell, which is a good starting point for our first attempt at studying the effect of magnetic torque on the interfacial dynamics. Figure 5.1 shows a schematic of the configuration of a two-layer thin fluid film in the region $0 < y < \beta h_0$, with h_0 being a characteristic "depth" of the ferrofluid film at rest. The interface between the fluids is denoted as $y = f(x,t)$. The ferrofluid thin film (fluid "2") is below the interface $0 < y < f$, while a nonmagnetic fluid (fluid "1") fills the remaining space $f < y < \beta h_0$.

The magnetic field $\mathbf{H}$ is determined by the magnetic scalar potential as $\mathbf{H} = \boldsymbol{\nabla}\psi$, which is subject to a Dirichlet boundary condition on the top and bottom walls. On the bottom wall, we apply a traveling-wave potential given by $\psi|_{y=0} = \psi_0 \cos(Kx/L + \Omega t)$. On the top wall, $\psi|_{y=\beta h_0} = 0$. This configuration will give rise to a rotating magnetic field $\mathbf{H}$, as we will show in Section 5.3.1. Such Dirichlet boundary condition is also used in [135], wherein a static and uniform magnetic scalar potential is imposed at the wall on the ferrofluid thin film. In the remainder of this chapter, we will first introduce the basic equations governing

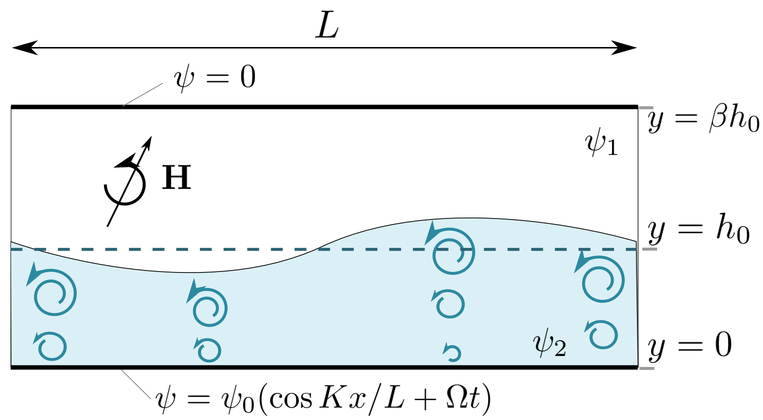

Figure 5.1. Schematic illustration of a ferrofluid film, with unperturbed depth h_0, subjected to a magnetic field $\mathbf{H}$ with rotation frequency Ω. This field is generated by the traveling-wave Dirichlet boundary condition on the magnetic scalar potential at the top and bottom boundaries. The interface, $y = f(x,t)$, separates the ferrofluid (fluid "2") from the exterior fluid (fluid "1"), which is assumed to have negligible viscosity and velocity (*e.g.*, air)

this model problem, including the balance of linear momentum, the balance of internal angular momentum, the magnetization equation, Maxwell's equations, as well as the suitable boundary condition on the fluid–fluid interface. Then, we will reduce the problem to a long-wave wave equation, followed by a discussion on linear instability and nonlinear dynamics exhibited by this reduced-order model of a ferrofluid thin field subject to magnetic surface torques.

5.1.1 Linear and internal angular momentum equation

The balances of linear and internal angular momentum in a ferrofluid can be derived from the macroscopic momentum conservation statements [136] and, respectively, take the forms:

$$\rho\left[\frac{\partial \boldsymbol{v}}{\partial t} + (\boldsymbol{v}\cdot\boldsymbol{\nabla})\boldsymbol{v}\right] = \boldsymbol{\nabla}\cdot\boldsymbol{T} + \boldsymbol{F}, \tag{5.1a}$$

$$\mathcal{I}\left[\frac{\partial \boldsymbol{\omega}}{\partial t} + (\boldsymbol{v}\cdot\boldsymbol{\nabla})\boldsymbol{\omega}\right] = \boldsymbol{\nabla}\cdot\boldsymbol{C} - \boldsymbol{\epsilon} : \boldsymbol{T} + \boldsymbol{G}, \tag{5.1b}$$

where ρ is the density of the ferrofluid, $\boldsymbol{v}$ is its velocity, $\mathcal{I}$ is the moment of inertia density, $\boldsymbol{\omega}$ is the spin velocity of the particles in the ferrofluid, $\boldsymbol{T}$ is the Cauchy stress tensor, $\boldsymbol{C}$ is the couple-stress dyadic, and $\boldsymbol{\epsilon}$ is the unit pseudo-isotropic triadic. For an incompressible ferrofluid, the body force density is $\boldsymbol{F} = \mu_0 \mathbf{M} \cdot \boldsymbol{\nabla}\mathbf{H}$, and the body-couple density is $\boldsymbol{G} = \mu_0 \mathbf{M} \times \mathbf{H}$. The Cauchy stress is expressed as (see, *e.g.*, [8], [136], [137]):

$$\boldsymbol{T} = -p\boldsymbol{I} + \mu_f[\boldsymbol{\nabla}\boldsymbol{v} + (\boldsymbol{\nabla}\boldsymbol{v})^\top] + \mu_v \boldsymbol{\epsilon} \cdot (\boldsymbol{\nabla} \times \boldsymbol{v} - 2\boldsymbol{\omega}) + \mu_b(\boldsymbol{\nabla} \cdot \boldsymbol{v})\boldsymbol{I}, \tag{5.2}$$

where $\boldsymbol{I}$ is the unit isotropic dyadic, and μ_f, μ_b, and μ_v are the coefficients of shear, bulk, and the so-called vortex viscosity, respectively. The couple-stress dyadic $\boldsymbol{C}$ characterizes the diffusion of internal angular momentum, and it has the form [138]:

$$\boldsymbol{C} = \mu_f'[\boldsymbol{\nabla}\boldsymbol{\omega} + (\boldsymbol{\nabla}\boldsymbol{\omega})^\top] + \mu_b'(\boldsymbol{\nabla} \cdot \boldsymbol{\omega})\boldsymbol{I}, \tag{5.3}$$

where μ_f' and μ_b' are the shear and bulk coefficients of spin viscosity, respectively, but they are both neglected in this study. Substituting the constitutive relations from Eqs. (5.2) and (5.3) into Eqs. (5.1a) and (5.1b), and employing the continuity equation $\boldsymbol{\nabla} \cdot \boldsymbol{v} = 0$ for an incompressible fluid, the linear and angular momentum balances become:

$$\rho \left[\frac{\partial \boldsymbol{v}}{\partial t} + (\boldsymbol{v} \cdot \boldsymbol{\nabla})\boldsymbol{v} \right] = -\boldsymbol{\nabla} p + \mu_0 \mathbf{M} \cdot \boldsymbol{\nabla}\mathbf{H} + 2\mu_v \boldsymbol{\nabla} \times \boldsymbol{\omega} + (\mu_f + \mu_v)\nabla^2 \boldsymbol{v}, \tag{5.4a}$$

$$\mathcal{I} \left[\frac{\partial \boldsymbol{\omega}}{\partial t} + (\boldsymbol{v} \cdot \boldsymbol{\nabla})\boldsymbol{\omega} \right] = \mu_0 \mathbf{M} \times \mathbf{H} + 2\mu_v(\boldsymbol{\nabla} \times \boldsymbol{v} - 2\boldsymbol{\omega}). \tag{5.4b}$$

The second term in Eq. (5.4b) results from the antisymmetric part of the Cauchy stress in Eq. (5.2), and represents the interchange of between internal angular momentum and macroscopic linear momentum. Physically, this term arises when there is a difference between the rate of rotation of a fluid element, *i.e.*, half the vorticity $\boldsymbol{\nabla} \times \boldsymbol{v}/2$, and the rate of internal spin of the particles $\boldsymbol{\omega}$ [139].

In the two-dimensional problem considered in Fig. 5.1, the velocity field is $\boldsymbol{v} = (u, v, 0)$ and the spin velocity is in the out-of-plane direction, *i.e.*, $\boldsymbol{\omega} = (0, 0, \omega)$.

We rewrite the Cauchy stress tensor from Eq. (5.2) using $\boldsymbol{\nabla} \cdot \boldsymbol{v} = 0$. Then, using the Maxwell tensor $\boldsymbol{T}_m = -\frac{\mu_0 H^2}{2}\boldsymbol{I} + \mathbf{BH}$, the *total* stress tensor for a ferrofluid (see, *e.g.*, [8], [82], [140]) is given by:

$$\boldsymbol{T}_{\text{tot}} = \boldsymbol{T} + \boldsymbol{T}_m = -p\boldsymbol{I} + \mu_f[\boldsymbol{\nabla}\boldsymbol{v} + (\boldsymbol{\nabla}\boldsymbol{v})^\top] + \mu_v \boldsymbol{\epsilon} \cdot (\boldsymbol{\nabla} \times \boldsymbol{v} - 2\boldsymbol{\omega}) - \frac{\mu_0 H^2}{2}\boldsymbol{I} + \mathbf{BH}, \quad (5.5)$$

Across the interface $y = f(x)$, the stress balances in the normal and tangential direction are given by

$$[\![\hat{\boldsymbol{n}} \cdot \boldsymbol{T}_{\text{tot}} \cdot \hat{\boldsymbol{n}}]\!] = \sigma\kappa, \quad (5.6a)$$

$$[\![\hat{\boldsymbol{n}} \cdot \boldsymbol{T}_{\text{tot}} \cdot \hat{\boldsymbol{\tau}}]\!] = 0, \quad (5.6b)$$

where $\hat{\boldsymbol{n}}$ denotes the upward unit normal vector to the interface, $\hat{\boldsymbol{\tau}}$ is the tangential vector, and κ is the curvature. These are given by

$$\hat{\boldsymbol{n}} = \frac{(-f_x, 1)}{\sqrt{1+f_x^2}}, \qquad \hat{\boldsymbol{\tau}} = \frac{(1, f_x)}{\sqrt{1+f_x^2}}, \qquad \kappa = -\frac{f_{xx}}{(1+f_x^2)^{2/3}}. \quad (5.7)$$

Equation (5.6a) is the expression of the Young–Laplace law, where σ is the surface tension at the fluid–fluid interface. Furthermore, the kinematic boundary condition is given by:

$$v = \frac{\partial f}{\partial t} + u\frac{\partial f}{\partial x} \quad \text{at} \quad y = f. \quad (5.8)$$

Finally, on the bottom of the domain, we impose the no-slip boundary condition:

$$u = 0 \quad \text{at} \quad y = 0. \quad (5.9)$$

5.1.2 Magnetization relaxation equation

The magnetization equation is a phenomenological equation describing, at the continuum level, the effect of the collective motion of the magnetic particles suspended in the nonmagnetic medium [82]. The magnetization field $\mathbf{M}$ of the ferrofluid evolves according to the classical model [141]:

$$\frac{\partial \mathbf{M}}{\partial t} + (\boldsymbol{v} \cdot \boldsymbol{\nabla})\mathbf{M} - \boldsymbol{\omega} \times \mathbf{M} + \frac{1}{\tau}[\mathbf{M} - \mathbf{M}_{\text{eq}}] = \mathbf{0}, \tag{5.10}$$

where the third term represents the generation of magnetization due to the "rotation" of the magnetized particles and their dipoles, while the last term represents the relaxation of the magnetization towards an equilibrium magnetization $\mathbf{M}_{\text{eq}}$. The relaxation time constant τ is on the order of 10^{-5} seconds for the ferrofluid used in [82]. The equilibrium magnetization $\mathbf{M}_{\text{eq}}$ is generally described by the Langevin equation. In the low magnetic field strength limit, *i.e.*, $|\mathbf{H}| \ll k_B T/(V_p M_p \mu_0)$, where k_B is Boltzmann's constant, T is the temperature, V_p is the magnetic particle's volume, and M_p is the domain magnetization for magnetite, the equilibrium magnetization is approximately linear with $\mathbf{H}$ [8]:

$$\mathbf{M}_{\text{eq}} \approx \chi \mathbf{H}, \tag{5.11}$$

where χ is the constant magnetic susceptibility.

5.1.3 Maxwell's equations

In the bulk flow, as introduced in Chapter 1, we have the quasistatic Maxwell's equations:

$$\boldsymbol{\nabla} \cdot \mathbf{B} = 0, \tag{5.12a}$$

$$\boldsymbol{\nabla} \times \mathbf{H} = \mathbf{0}, \tag{5.12b}$$

where $\mathbf{B}$ is the magnetic flux given by

$$\mathbf{B} = \mu_0(\mathbf{M} + \mathbf{H}). \tag{5.13}$$

Fluid 1 is non-magnetic, such that $\mathbf{M}_1 = \mathbf{0}$. Applying Eq. (5.12a) to each phase, and introducing the magnetic potential ψ, allows us to rewrite Maxwell's equations as

$$\nabla^2\psi_1 = 0, \qquad \nabla^2\psi_2 = -\boldsymbol{\nabla}\cdot\mathbf{M}_2, \tag{5.14}$$

where $\boldsymbol{\nabla}\psi_i = \mathbf{H}_i$. Across the interface, we have the jump conditions

$$[\![\mathbf{B}\cdot\hat{\boldsymbol{n}}]\!] = 0, \qquad [\![\mathbf{H}\cdot\hat{\boldsymbol{\tau}}]\!] = 0. \tag{5.15}$$

5.2 Reduced model under the lubrication approximation

We seek to obtain a reduced-order model from the many coupled equations introduced above. To this end, in this section, we apply the lubrication approximation to the linear momentum and internal angular momentum equations. The magnetization and Maxwell's equations are scaled with respect to a long wavelength L, according to the longitudinal and vertical disparity of scales embodied in a thin film.

Now, the dimensionless governing equations and boundary conditions (dimensionless variables are denoted by a tilde) are as follows:

$$\begin{aligned}
&x = L\tilde{x}, \quad && y = h_0\tilde{y}, && f = h_0\tilde{f}, && t = \frac{U}{L}\tilde{t},\\
&u = U\tilde{u}, && v = \delta U\tilde{v}, && \omega = \frac{U}{h_0}\tilde{\omega}, && p = \frac{\mu_f UL}{h_0^2}\tilde{p}\\
&\psi = \psi_0\tilde{\psi}, && \mathbf{H} = H_0(\delta\tilde{H}_x, \tilde{H}_y), && \mathbf{M} = H_0(\delta\tilde{M}_x, \tilde{M}_y), &&
\end{aligned} \tag{5.16}$$

where L is the (long) characteristic horizontal length scale, $H_0 = \psi_0/h_0$, and the aspect ratio is $\delta = h_0/L \ll 1$.

5.2.1 Reduced linear and angular momentum equations

We first introduce the convective and rotational Reynolds numbers, respectively:

$$\mathrm{Re} = \frac{\rho UL}{\mu_f}, \qquad \mathrm{Re}_I = \frac{\mathcal{I}U}{L\mu_v}. \tag{5.17}$$

The magnetic Bond number is

$$\mathrm{N_B} = \frac{\mu_0 H_0^2 L}{U\mu_f}\delta^2, \tag{5.18}$$

representing the ratio of the magnetic body force to the viscous forces in the flow. Then, the scaled linear momentum equation (5.4a), written in components, is:

$$\delta^2 \mathrm{Re}\frac{\tilde{D}\tilde{u}}{\tilde{D}\tilde{t}} = -\frac{\partial \tilde{p}}{\partial \tilde{x}} + \mathrm{N_B}\left(\delta^2 \tilde{M}_x \frac{\partial \tilde{H}_x}{\partial \tilde{x}} + \tilde{M}_y \frac{\partial \tilde{H}_x}{\partial \tilde{y}}\right) + 2\frac{\mu_v}{\mu_f}\frac{\partial \tilde{\omega}}{\partial \tilde{y}} + \left(1 + \frac{\mu_v}{\mu_f}\right)\tilde{\nabla}^2 \tilde{u}, \tag{5.19a}$$

$$\delta^4 \mathrm{Re}\frac{\tilde{D}\tilde{v}}{\tilde{D}\tilde{t}} = -\frac{\partial \tilde{p}}{\partial \tilde{y}} + \mathrm{N_B}\left(\delta^2 \tilde{M}_x \frac{\partial \tilde{H}_y}{\partial \tilde{x}} + \tilde{M}_y \frac{\partial \tilde{H}_y}{\partial \tilde{y}}\right) - 2\delta^2\frac{\mu_v}{\mu_f}\frac{\partial \tilde{\omega}}{\partial \tilde{x}} + \delta^2\left(1 + \frac{\mu_v}{\mu_f}\right)\tilde{\nabla}^2 \tilde{v}, \tag{5.19b}$$

where $\frac{\tilde{D}(\cdot)}{\tilde{D}\tilde{t}} = \frac{\partial(\cdot)}{\partial \tilde{t}} + \tilde{u}\frac{\partial(\cdot)}{\partial \tilde{x}} + \tilde{v}\frac{\partial(\cdot)}{\partial \tilde{y}}$, and $\tilde{\nabla}^2(\cdot) = \delta^2\frac{\partial^2(\cdot)}{\partial \tilde{x}^2} + \frac{\partial^2(\cdot)}{\partial \tilde{y}^2}$. The scaled balance of internal angular momentum (5.4b) is:

$$\mathrm{Re}_I \frac{\tilde{D}\tilde{\omega}}{\tilde{D}\tilde{t}} = \mathrm{N_B}\frac{\mu_f}{\mu_v}\left(\tilde{\mathbf{M}} \times \tilde{\mathbf{H}}\right)\cdot \hat{\boldsymbol{e}}_z + 2\left(\delta^2\frac{\partial \tilde{v}}{\partial \tilde{x}} - \frac{\partial \tilde{u}}{\partial \tilde{y}}\right) - 4\tilde{\omega}. \tag{5.20}$$

Neglecting terms of $\mathcal{O}(\delta^2, \delta^4, \delta^2\mathrm{Re}, \delta^4\mathrm{Re}, \mathrm{Re}_I)$, the linear momentum equations (5.19) simplify to

$$\frac{\partial \tilde{p}}{\partial \tilde{x}} = \mathrm{N_B}\tilde{M}_y \frac{\partial \tilde{H}_x}{\partial \tilde{y}} + 2\frac{\mu_v}{\mu_f}\frac{\partial \tilde{\omega}}{\partial \tilde{y}} + \left(1 + \frac{\mu_v}{\mu_f}\right)\frac{\partial^2 \tilde{u}}{\partial \tilde{y}^2}, \tag{5.21a}$$

$$\frac{\partial \tilde{p}}{\partial \tilde{y}} = \mathrm{N_B}\tilde{M}_y \frac{\partial \tilde{H}_y}{\partial \tilde{y}}, \tag{5.21b}$$

and the angular momentum equation (5.20) becomes:

$$4\tilde{\omega} = \mathrm{N_B}\frac{\mu_f}{\mu_v}\tilde{T} - 2\frac{\partial \tilde{u}}{\partial \tilde{y}}, \tag{5.22}$$

where the magnetic torque is $\tilde{T} = \left(\tilde{\mathbf{M}} \times \tilde{\mathbf{H}}\right)\cdot \hat{\boldsymbol{e}}_z$.

At the interface, $y = f(x,t)$, the stress balances in the normal and tangential directions from Eq. (5.6), to leading order, yield:

$$-\left[\!\!\left[\tilde{p} + \frac{1}{2}\mathrm{N_B}\tilde{M}_y^2\right]\!\!\right] = -\frac{1}{\mathrm{Ca}}\tilde{f}'', \tag{5.23a}$$

$$\left[\!\!\left[\frac{\partial \tilde{u}}{\partial \tilde{y}} + \frac{\mu_v}{\mu_f}\left(\frac{\partial \tilde{u}}{\partial \tilde{y}} + 2\tilde{\omega}\right)\right]\!\!\right] = 0, \tag{5.23b}$$

where the scaled capillary number Ca is given by

$$\mathrm{Ca} = \frac{\mu_f U}{\sigma}\delta^{-3}, \tag{5.24}$$

as is standard for thin films [142]. By combining Eq. (5.23b) and the angular momentum equation (5.22), we see that the torque on the interface acts as a shear stress:

$$\frac{\partial \tilde{u}}{\partial \tilde{y}} = -\frac{\mathrm{N_B}}{2}\tilde{T}. \tag{5.25}$$

Finally, the scaled kinematic boundary condition has the same form as Eq. (5.8). Using the continuity equation, the kinematic boundary condition can be rewritten as

$$\frac{\partial \tilde{f}}{\partial \tilde{t}} + \frac{\partial}{\partial \tilde{x}}\left(\int_0^{\tilde{f}} \tilde{u}\, d\tilde{y}\right) = 0. \tag{5.26}$$

5.2.2 Reduced magnetization equation

Due to the fast relaxing of the magnetization, as discussed in Section 1.4 in the introduction, it is necessary to choose a different time scale for the magnetization equation. The relaxation time τ is a reasonable option:

$$t = \tau\bar{t}. \tag{5.27}$$

Note that different time scales in the flow equations and the magnetization equations will be reconciled in Section 5.3.2, wherein we will calculate the time-averaged magnetic forcing terms over one rotating period, *i.e.*, we will average over the fast $\bar{t}$ time and eliminate it from the equations.

Then, the scaled magnetization equation can be written as

$$\frac{\partial \tilde{\mathbf{M}}}{\partial \bar{t}} + \frac{1}{\mathrm{Sr}_M}(\tilde{\boldsymbol{v}} \cdot \boldsymbol{\nabla})\tilde{\mathbf{M}} - \frac{1}{\mathrm{Sr}_M \delta}\tilde{\boldsymbol{\omega}} \times \tilde{\mathbf{M}} + (\tilde{\mathbf{M}} - \chi \tilde{\mathbf{H}}) = \mathbf{0}, \tag{5.28}$$

where the magnetization Strouhal number is defined as

$$\mathrm{Sr}_M = \frac{L}{\tau U}. \tag{5.29}$$

This Strouhal represents the relative magnitudes of the convective time scale, L/U, to the characteristic time of magnetization evolution, τ. Assuming the convective time scale is much larger than that of magnetization, i.e., $1/\mathrm{Sr}_M \ll \delta$, the changes of magnetization due to rotation and convection are negligible, and the magnetization equation (5.28) can be simplified as

$$\frac{\partial \tilde{\mathbf{M}}}{\partial \bar{t}} + (\tilde{\mathbf{M}} - \chi \tilde{\mathbf{H}}) = \mathbf{0}. \tag{5.30}$$

5.2.3 Reduced Maxwell's equations

The scaled Maxwell's equations (5.14) can be written as

$$\delta^2 \frac{\partial^2 \tilde{\psi}_1}{\partial \tilde{x}^2} + \frac{\partial^2 \tilde{\psi}_1}{\partial \tilde{y}^2} = 0, \tag{5.31a}$$

$$\delta^2 \frac{\partial^2 \tilde{\psi}_2}{\partial \tilde{x}^2} + \frac{\partial^2 \tilde{\psi}_2}{\partial \tilde{y}^2} = -\left(\delta^2 \frac{\partial \tilde{M}_x}{\partial \tilde{x}} + \frac{\partial \tilde{M}_y}{\partial \tilde{y}}\right). \tag{5.31b}$$

Keeping only the leading order terms, we obtain:

$$\frac{\partial^2 \tilde{\psi}_1}{\partial \tilde{y}^2} = 0, \qquad \frac{\partial^2 \tilde{\psi}_2}{\partial \tilde{y}^2} = -\frac{\partial \tilde{M}_y}{\partial \tilde{y}}, \tag{5.32}$$

with the boundary condition at the walls:

$$\tilde{\psi}_1 = 0 \qquad \text{on} \quad \tilde{y} = \beta, \tag{5.33a}$$

$$\tilde{\psi}_2 = \cos(K\tilde{x} + \bar{\Omega}\bar{t}) \qquad \text{on} \quad \tilde{y} = 0. \tag{5.33b}$$

On the interface, the leading-order boundary conditions (5.15) are

$$\frac{\partial \tilde{\psi}_1}{\partial \tilde{y}} = \frac{\partial \tilde{\psi}_2}{\partial \tilde{y}} + \tilde{M}_y \qquad \text{on} \quad \tilde{y} = \tilde{f}(\tilde{x}, \tilde{t}), \tag{5.34a}$$

$$\tilde{\psi}_1 = \tilde{\psi}_2 \qquad \text{on} \quad \tilde{y} = \tilde{f}(\tilde{x}, \tilde{t}). \tag{5.34b}$$

5.3 Derivation of the long-wave equation

In this section, we will derive a long-wave equation out of the reduced model in Section 5.2. Note that the time scale in the magnetization equation (5.30) is different from that in other equations. Thus, we will first calculate the magnetic field and magnetization at the instantaneous surface position $\tilde{y} = \tilde{f}(\tilde{x}, \tilde{t})$, and then calculate the time-averaged (over the fast time scale of the magnetization equation) forcing terms that act on the linear momentum and internal angular momentum equations.

5.3.1 Leading order solution of magnetic field and magnetization

In this section, we will first solve Eq. (5.30) using an arbitrary rotating magnetic field to show the phase lag of the magnetization. Then, we will solve Eq. (5.32) for the magnetic field corresponding to the configuration in Fig. 5.1, and derive the generalized relation between the magnetic field and the magnetization.

To start, we assume that the harmonic potential applied on the boundary can generate the rotating magnetic field

$$\tilde{H}_x(\tilde{x},\tilde{y},\bar{t}) = \tilde{H}_{xc}(\tilde{x},\tilde{y})\cos\Xi + \tilde{H}_{xs}(\tilde{x},\tilde{y})\sin\Xi, \tag{5.35a}$$

$$\tilde{H}_y(\tilde{x},\tilde{y},\bar{t}) = \tilde{H}_{yc}(\tilde{x},\tilde{y})\cos\Xi + \tilde{H}_{ys}(\tilde{x},\tilde{y})\sin\Xi, \tag{5.35b}$$

where $\Xi = K\tilde{x} + \bar{\Omega}\bar{t}$, and $\bar{\Omega} = \tau\Omega$ is the scaled external driving frequency. Then, the magnetization can be solved from Eq. (5.30) as

$$\tilde{M}_x(\tilde{x},\tilde{y},\bar{t}) = \chi^*[(H_{xc} - H_{xs}\bar{\Omega})\cos\Xi + (H_{xc}\bar{\Omega} + H_{xs})\sin\Xi], \tag{5.36a}$$

$$\tilde{M}_y(\tilde{x},\tilde{y},\bar{t}) = \chi^*[(H_{yc} - H_{ys}\bar{\Omega})\cos\Xi + (H_{yc}\bar{\Omega} + H_{ys})\sin\Xi], \tag{5.36b}$$

which can also be written as

$$\tilde{M}_x(\tilde{x},\tilde{y},\bar{t}) = \chi\tilde{H}_{xc}\cos(\Xi-\alpha) + \chi\tilde{H}_{xs}\sin(\Xi-\alpha), \tag{5.37a}$$

$$\tilde{M}_y(\tilde{x},\tilde{y},\bar{t}) = \chi\tilde{H}_{yc}\cos(\Xi-\alpha) + \chi\tilde{H}_{ys}\sin(\Xi-\alpha), \tag{5.37b}$$

where $\chi^* = \chi/(1+\bar{\Omega}^2)$, and α is the phase lag between the magnetic field and the magnetization with $\tan\alpha = \bar{\Omega}$. Note that the torque can then be calculated as

$$\tilde{T} = \left(\tilde{\mathbf{M}} \times \tilde{\mathbf{H}}\right)\cdot \hat{\boldsymbol{e}}_z = \tilde{M}_x\tilde{H}_y - \tilde{M}_y\tilde{H}_x = \frac{\chi\bar{\Omega}}{1+\bar{\Omega}^2}(\tilde{H}_{xc}\tilde{H}_{ys} - \tilde{H}_{xs}\tilde{H}_{yc}). \tag{5.38}$$

Next, we solve Maxwell's equations (5.32) in the proposed configuration Fig. 5.1. For convenience, the $(\tilde{\cdot})$ notation will be dropped henceforth.

We first assume $\partial M_y/\partial y = 0$, which will be proved later, and then integrate Eq. (5.32) twice, using the boundary conditions (5.33) on the top and bottom walls to find the integration constants. We thus obtain a solution ansatz as

$$\psi_1 = C_1(y-\beta)\sin\Xi + A_1(y-\beta)\cos\Xi, \tag{5.39a}$$

$$\psi_2 = C_2 y\sin\Xi + (A_2 y + 1)\cos\Xi, \tag{5.39b}$$

where unknown parameters A_1, A_2, C_1, C_2 are functions of x only, and are to be obtained by applying the interface conditions (5.34) at $y = f(x,t)$.

The solution from Eq. (5.39) gives rise to the magnetic field components in fluid 1 and fluid 2:

$$H_{1,y} = \frac{\partial \psi_1}{\partial y} = C_1 \sin \Xi + A_1 \cos \Xi, \tag{5.40a}$$

$$H_{2,y} = \frac{\partial \psi_2}{\partial y} = C_2 \sin \Xi + A_2 \cos \Xi, \tag{5.40b}$$

$$H_{2,x} = \frac{\partial \psi_2}{\partial x} = (A_2' y + K C_2 y) \cos \Xi + [C_2' y - K(A_2 y + \mathcal{A})] \sin \Xi. \tag{5.40c}$$

Using the relation between the magnetic field and magnetization derived in Eq. (5.36), we obtain the magnetization in fluid 2:

$$M_y = \chi^* [(A_2 - C_2 \bar{\Omega}) \cos \Xi + (A_2 \bar{\Omega} + C_2) \sin \Xi], \tag{5.41}$$

which is indeed independent of y, as assumed.

Next, substituting Eqs. (5.40) and (5.41) into the interfacial boundary condition (5.34a), and Eq. (5.39) into Eq. (5.34b), we can obtain the following relations:

$$C_1 = C_2 + \chi^* (A_2 \bar{\Omega} + C_2), \tag{5.42a}$$

$$A_1 = A_2 + \chi^* (A_2 - C_2 \bar{\Omega}), \tag{5.42b}$$

$$C_2 f = C_1 (f - \beta), \tag{5.42c}$$

$$A_2 f + 1 = A_1 (f - \beta), \tag{5.42d}$$

which can be solved by

$$A_2 = \frac{\chi^*(f - \beta) - \beta}{[\chi^*(f - \beta) - \beta]^2 + [\chi^* \bar{\Omega}(f - \beta)]^2}, \tag{5.43a}$$

$$C_2 = \frac{-\bar{\Omega} \chi^* (f - \beta)}{[\chi^*(f - \beta) - \beta]^2 + [\chi^* \bar{\Omega}(f - \beta)]^2}. \tag{5.43b}$$

Now, given the interface deformation $y = f(x,t)$, the magnetic field and magnetization can be obtained, by assuming that the time scale of the flow dynamics is significantly greater than the time scale of the external forcing. In such cases, it is possible to approximate the magnetic field forces by their time-averaged values over the forcing time scale (*i.e.*, the time scale of the rotating magnetic field. This approximation allows for a simplified representation of the magnetic field forces and their impact on the film, and this time-scale separation and time-averaged force evaluation approach is commonly used in studies of time-varying forcing of ferrofluids [62], [66].

5.3.2 Time-averaged equations

In this section, we introduce the decoupled governing equations by approximating the magnetic body force, normal stress, magnetic torque, and spin velocity by their averaged values on the rotating time scale:

$$\begin{aligned}
&x\text{-momentum:} && \frac{\partial p}{\partial x} = \mathrm{N_B}\left\langle M_y \frac{\partial H_x}{\partial y}\right\rangle + 2\frac{\mu_v}{\mu_f}\frac{\partial\langle\omega\rangle}{\partial\tilde{y}} + \left(1+\frac{\mu_v}{\mu_f}\right)\frac{\partial^2 u}{\partial y^2}, && (5.44a)\\
&y\text{-momentum:} && \frac{\partial p}{\partial y} = \mathrm{N_B}\left\langle M_y \frac{\partial H_y}{\partial y}\right\rangle, && (5.44b)\\
&\text{angular momentum:} && 4\langle\omega\rangle = \mathrm{N_B}\frac{\mu_f}{\mu_v}\langle T\rangle - 2\frac{\partial u}{\partial y}, && (5.44c)\\
&[\![\hat{\boldsymbol{n}}\cdot\boldsymbol{T}\cdot\hat{\boldsymbol{n}}]\!] = \sigma\kappa : && p + \frac{1}{2}\mathrm{N_B}\langle M_y^2\rangle = -\frac{1}{\mathrm{Ca}}f'', && (5.44d)\\
&[\![\hat{\boldsymbol{n}}\cdot\boldsymbol{T}\cdot\hat{\boldsymbol{\tau}}]\!] = 0 : && \frac{\partial u}{\partial y} = \frac{\mu_v}{\mu_f}\left(-\frac{\partial u}{\partial y} - 2\langle\omega\rangle\right), && (5.44e)
\end{aligned}$$

where $\langle\cdot\rangle = \int_0^{2\pi/\bar{\Omega}}(\cdot)\,d\bar{t}$ represents the averaging over one rotating period $2\pi/\bar{\Omega}$ of the magnetic field on the fast time scale $\bar{t}$. By substituting Eqs. (5.40) into Eq. (5.41), we obtain

$$\begin{aligned}
F_b = \left\langle M_y\frac{\partial H_x}{\partial\tilde{y}}\right\rangle &= \frac{\chi^*}{4}[(A_2^2+C_2^2)' - 2K\bar{\Omega}(A_2^2+C_2^2) + 2\bar{\Omega}(A_2C_2' - C_2A_2')], && (5.45a)\\
F_s = \langle M_y^2\rangle &= \frac{\chi^{*2}}{2}[(1+\bar{\Omega}^2)(A_2^2+C_2^2)], && (5.45b)\\
T_b = \langle T\rangle &= \bar{\Omega}\chi^*[(C_2A_2' - A_2C_2')y + K(A_2^2+C_2^2)y + KA_2]. && (5.45c)
\end{aligned}$$

Now, we can calculate the time-average body force F_b, time-averaged torque T_b, and time-averaged magnetic normal stress F_s. Note that $\partial H_y/\partial y = 0$, such that the pressure p is independent of y according to Eq. (5.44b).

Next, we will derive the long-wave equation based on the time-averaged model (5.44).

5.3.3 Long-wave equation

Since $\partial p/\partial y = 0$, we can integrate the x-component linear momentum equation (5.44b) with respect to y:

$$\frac{\partial p}{\partial x} y = \mathrm{N_B} F_b y + \frac{\mathrm{N_B}}{2} T_b + \frac{\partial u}{\partial y} + c(x), \tag{5.46}$$

where F_b is independent of y as calculated in Eq. (5.45a), and $c(x)$ is the integration constant. As discussed in the previous section, the angular momentum equation (5.44c) simplifies the tangential stress balance condition (5.44c) on the interface $y = f(x,t)$ as $\partial u/\partial y = -\mathrm{N_B} T_b/2$. This interfacial boundary condition determines $c(x)$, and we have

$$\frac{\partial u}{\partial y} = \left(\frac{\partial p}{\partial x} - \mathrm{N_B} F_b\right)(y - h) - \frac{\mathrm{N_B}}{2} T_b. \tag{5.47}$$

Integrating Eq. (5.47) with respect to y once more, and imposing the no-slip condition (5.9), we can obtain the velocity profile as

$$u = \left(\frac{\partial p}{\partial x} - \mathrm{N_B} F_b\right)\left(\frac{1}{2}y^2 - hy\right) - \frac{\mathrm{N_B}\bar{\Omega}\chi^*}{2}\left\{[C_2 A_2' - A_2 C_2' + K(A_2^2 + C_2^2)]\frac{y^2}{2} + kA_2 y\right\}, \tag{5.48}$$

where $\partial p/\partial x$ can be obtained by differentiating the normal stress balance condition (5.44d) with respect to x.

Thus, we have derived a long-wave equation in the form:

$$\frac{\partial f}{\partial t} + \frac{\partial q}{\partial x} = 0, \qquad \text{with} \tag{5.49a}$$

$$q = \frac{1}{3\mathrm{Ca}} f^3 f''' - \frac{\mathrm{N_B}}{4}\chi^*\bar{\Omega} K f^3 + \frac{\mathrm{N_B}}{4}\chi^*\bar{\Omega}(A_2 C_2' - C_2 A_2') f^3 - \frac{\mathrm{N_B}}{4}\chi^*\bar{\Omega} K A_2 f^2, \tag{5.49b}$$

where A_2 and C_2 can be found from Eq. (5.43), and

$$A_2 C_2' - C_2 A_2' = \left\{ \frac{1}{[\chi^*(f-\beta)-\beta]^2 + [\chi^*\bar{\Omega}(f-\beta)]^2} \right\}^2 \chi^* \bar{\Omega} f' \beta. \tag{5.50}$$

The first term in Eq. (5.49b) arises from surface tension, which is commonly obtained from the thin film dynamics, such as in [143], while the second and third terms arise from the combination of magnetic body force and torque. The fourth term arises from the magnetic torque only. Clearly, the long-wave equation (5.49) is highly nonlinear, and the effect of each physical force on the thin film evolution is not immediately clear due to their coupling.

5.4 Thin film evolution

In this section, using our long-wave equation (5.49), we study the effect of magnetic torque on the linear and nonlinear dynamics of the thin film evolution.

5.4.1 Linear stability analysis

First, we carry out a linear stability analysis of the evolution equation (5.49), by perturbing the flat film as $f(x,t) = 1 + \epsilon\eta(x,t)$, where $\epsilon \ll 1$. Next, taking the Fourier decomposition of the surface elevation as $\eta(x,t) = \sum_{k=-\infty}^{\infty} \eta_k(t) e^{ikx}$, at leading-order we obtain $\dot{\eta}_k = \Lambda(k)\eta_k$, with

$$\begin{aligned} \Lambda(k) = &\left[\frac{\mathrm{N_B}(\chi^*\bar{\Omega})^2\beta}{4(m_0^2+n_0^2)^2} - \frac{1}{3\mathrm{Ca}} k^2 \right] k^2 \\ &+ \left[\frac{3K\mathrm{N_B}\chi^*\bar{\Omega}}{4} + \frac{\mathrm{N_B}\chi^*\bar{\Omega}}{4(m_0^2+n_0^2)} \left(2m_0 + 1 - \frac{2\chi^* m_0^2 + 2\chi^* n_0 m_0 \bar{\Omega}}{m_0^2+n_0^2} \right) \right] ik, \end{aligned} \tag{5.51}$$

where $m_0 = [\chi^*(h_0-\beta)-\beta]$, and $n_0 = [\chi^*\bar{\Omega}(h_0-\beta)]$.

The real part of the linear growth rate (5.51) is similar to the one in Section 3.3. Surface tension stabilizes the film, while the rotation of the external field destabilizes it (the third term of the flux q in Eq. (5.49b)). The most unstable mode k_m satisfies:

$$\left. \frac{d\,\mathrm{Re}\,[\Lambda(k)]}{dk} \right|_{k=k_m} = 0 \qquad \Longleftrightarrow \qquad k_m^2 = \frac{3\mathrm{Ca}\mathrm{N_B}(\chi^*\bar{\Omega})^2\beta}{8(m_0^2+n_0^2)^2}, \tag{5.52}$$

which is more sensitive to the change of rotation frequency $\bar{\Omega}$ than the field strength $\mathrm{N_B}$. Figure 3.2(a) shows examples of how the linear growth rate, which is characterized by the typical long-wave instability of thin-films [142]. The imaginary part of the growth rate $\mathrm{Im}\,[\Lambda(k)]$, contributed by the second and fourth term of the flux q from Eq. (5.49b), suggests the possibility of nondispersive (coherent) wave propagation, as in Chapters 2 and 3. Indeed, the phase velocity $\mathrm{Im}\,[\Lambda(k)]/k$ can be used to predict the nonlinear propagation velocity, which will be discussed in Section 5.4.2.

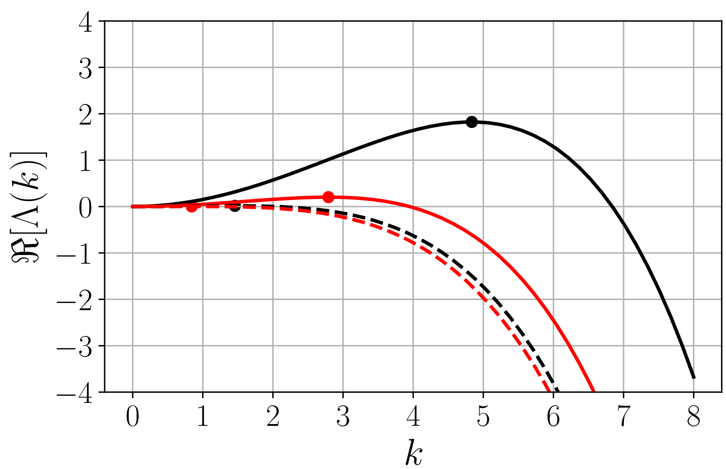

Figure 5.2. Real part of the linear growth rate, $\mathrm{Re}\,[\Lambda(k)]$, as a function of the wavenumber k for different magnetic Bond numbers: $\mathrm{N_B} = 1000$ (red) and $\mathrm{N_B} = 3000$ (black), with the rotating frequency set by $\bar{\Omega} = 0.03$ (dashed) or $\bar{\Omega} = 0.1$ (solid). The most unstable mode k_m is marked with $\bullet$.

5.4.2 Nonlinear evolution

To understand the nonlinear interfacial wave dynamics subjected to a fast-varying magnetic field, we solve Eq. (5.49) numerically using the pseudospectral method [109]. For the linear terms, the spatial derivatives are evaluated using the fast Fourier transform (FFT) with $N = 256$, while the nonlinear terms are inverted back to the physical domain (via the inverse FFT), evaluated, and then transformed back to Fourier space. The fourth-order Runge–Kutta scheme is used for time advancement. To stabilize the simulation, three-fifths of the higher wavenumbers are filtered out. The parameters $\mathrm{Ca} = 100$, $\chi = 5$, and $K = 1$

will be used in this section, and the initial flat interface will be perturbed by mode $k = 1$ as $f(x, 0) = 1 + 0.005\sin(x)$.

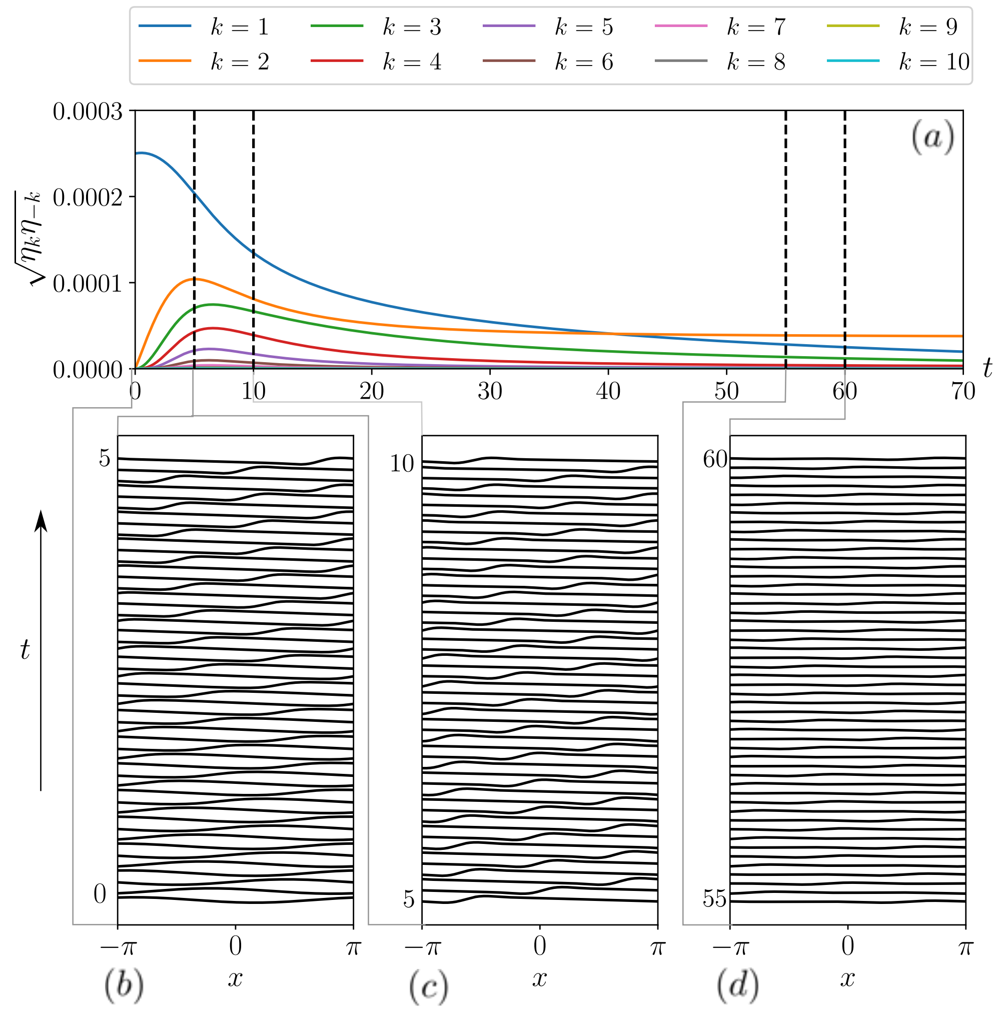

Figure 5.3. Interface evolution of the ferrofluid thin film subjected to a magnetic field with $\mathrm{N_B} = 3000$ and rotating frequency $\bar{\Omega} = 0.03$. The Fourier mode energy evolution is shown in (a), with the wave profile evolution shown in (b), (c), and (d).

Wave propagation, as suggested by the imaginary part of the linear growth rate, can be observed in Figs. 5.3 and 5.4. However, due to the strong nonlinearities of the long-wave equation, the range of validity of the linear analysis is limited. The simulations in Figs. 5.3 and 5.4 are both conducted with $\mathrm{N_B} = 3000$, while the simulation in Fig. 5.4 is for a higher forcing frequency $\bar{\Omega} = 0.1$ (compared to $\bar{\Omega} = 0.03$ used in Fig. 5.3). The most unstable mode is $k_m \approx 1.5$ in Fig. 5.3, and $k_m \approx 4.8$ in Fig. 5.4. The mode $k = 1$ is linearly unstable, *i.e.*,

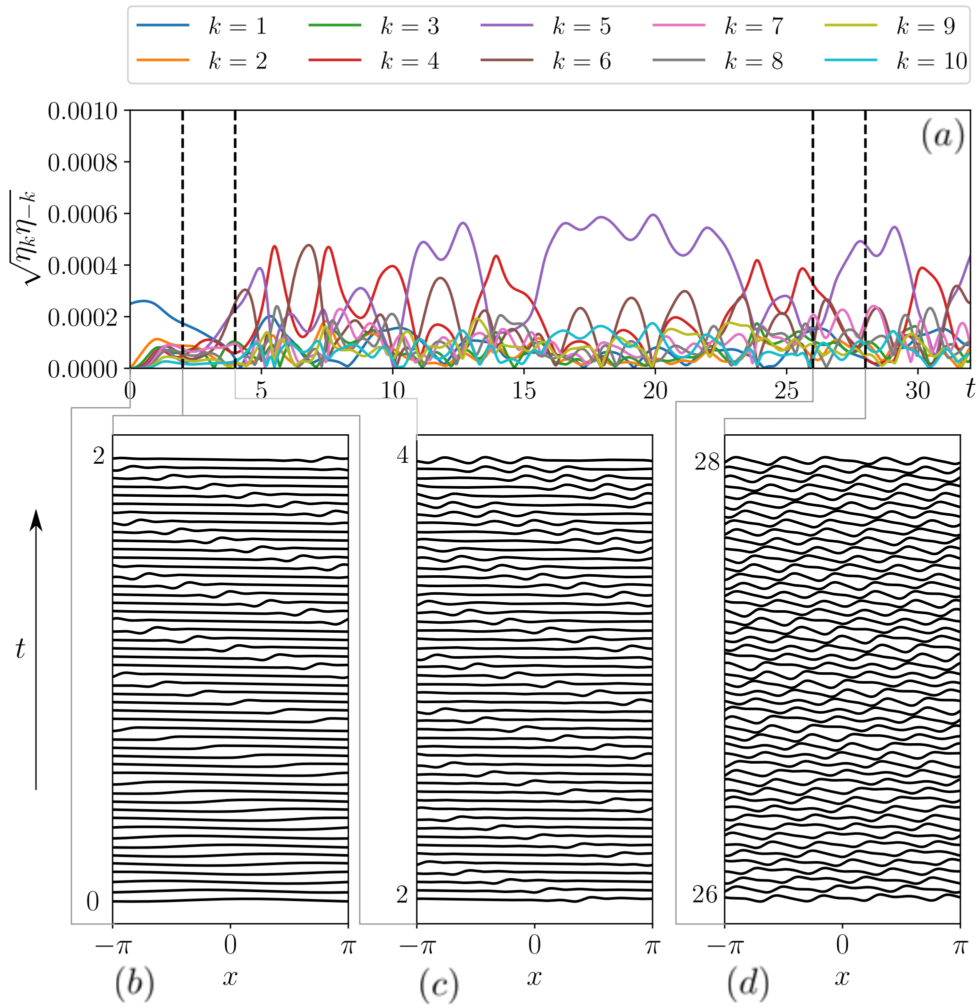

Figure 5.4. Interface evolution of the ferrofluid thin film subjected to a magnetic field with $\mathrm{N_B} = 3000$ and rotating frequency $\bar{\Omega} = 0.1$. The Fourier mode energy evolution is shown in (a), with the wave profile evolution shown in (b), (c), and (d).

$\mathrm{Re}\,[\Lambda(k=1)] > 0$ in both simulations. It experiences a short growth ($t \in [0,5]$ in Fig. 5.3 and $t \in [0,1]$ in Fig. 5.4), followed by the decay.

Meanwhile, the other modes $k > 0$ grow sequentially from zero due to the nonlinear interactions. They reach a peak value on the same order as the first mode. The interface deformation in this time period is shown in Fig. 5.3(b) and Fig. 5.4(b), where a "shock wave" emerges from the initial flat interface with small harmonic perturbation. Subsequently, however, the interface evolution under different forcing frequencies is not the same. For a lower frequency $\bar{\Omega} = 0.03$, the amplitude of the "shock wave" starts to decay around time $t \approx 5$, as shown in Fig. 5.3(c). The decay lasts for a long time, as indicated in the Fourier components' evolution shown in Fig. 5.3(a). Finally, this wave can be barely seen in comparison with the initial perturbation, as shown in Fig. 5.3(d). However, for a higher frequency $\bar{\Omega} = 0.1$, this "shock wave" first decays and then evolves into a triple-peak wave, as shown in Fig. 5.4(c). Figure 5.4(a) suggests a long-time wave interaction with finite amplitude around $|\eta_k| \simeq 10^{-4}$. One time window for $t \in [26, 28]$ shown in Fig. 5.4(d) highlights the disordered wave state.

In the remainder of this section, we will investigate separately these two observations: (i) the similar formation of a propagating "shock wave" for both forcing frequencies and (ii) the different long-time evolution for each forcing frequency. We will start with the effect of the parameters on the characteristic of the "shock wave," such as the profile shape and the propagation speed. Then, we will discuss the long-lasting disordered waves shown in Fig. 5.4(d).

"Shock wave" propagation

The propagating "shock wave" emerges from the flat interface for all parameter values considered in this study, including $\mathrm{N_B} = 1000, 3000$ with rotating frequency $\bar{\Omega} = 0.03, 0.1$. Figure 5.5 shows a comparison of the wave profile, for different parameter values, at the time when the interface is achieving the largest amplitude during the "shock wave" evolution. For larger rotating frequencies or a stronger magnetic field, the "shock wave" is steeper and has a larger amplitude.

As shown in Figs. 5.3(a) and 5.4(a), the propagating "shock wave" consists of multiple harmonic modes interacting nonlinearly. However, this waveform also shows the nondispersive feature indicated by the imaginary part of the linear growth rate (5.51). In this section, we measure the propagation velocity in two ways. The most direct way is to trace the velocity of one peak in the physical domain. Another way is to calculate the velocity using the method described in Section 2.4.2, namely by tracing the phase change in the Fourier domain. The latter may be suitable here since the "shock wave" propagates as a coherent wavepacket for a substantial time. This behavior is evident from observing that

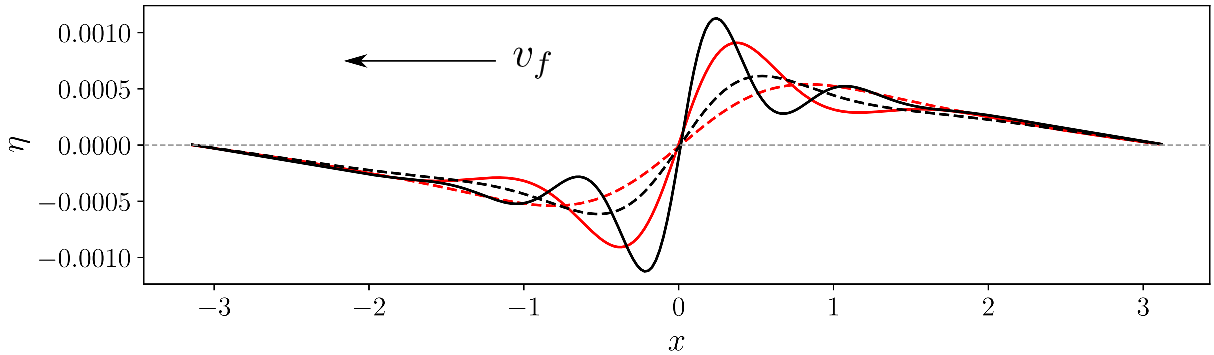

Figure 5.5. Comparison of the propagating "shock wave" profile for different magnetic Bond numbers: $\mathrm{N_B} = 1000$ (red) and $\mathrm{N_B} = 3000$ (black), with the rotating frequency set by $\bar{\Omega} = 0.03$ (dashed) or $\bar{\Omega} = 0.1$ (solid).

the propagation velocity is the same for the first five harmonic modes during the "shock wave" evolution, as shown in Fig. 5.6(a). The velocity remains constant until the transient to the disordered wave state occurs if there is one. The difference between these two velocity measurement methods is less than 0.1%, which provides confidence in the estimate of the nonlinear wave speed.

Figure 5.6(b) shows the comparison of the constant "shock wave" propagation speed and the phase velocity evaluated from the imaginary part of Eq. (5.51), *i.e.*, $\mathrm{Im}\,[\Lambda(k)]/k$. It is surprising that while the real part of the linear growth rate has limited predictive power of the highly nonlinear evolution, the imaginary part makes a good prediction of the propagation velocity of the "shock wave," even though the steep front necessitates multiple harmonic modes to capture (due to the nonlinear interactions between modes). In addition, Fig. 5.6(b) shows, that despite the fact that the imaginary part of Eq. (5.51) is not a linear function of the rotating frequency $\bar{\Omega}$, $\mathrm{Im}\,[\Lambda(k)]$ grows linearly over the frequency ranged $\bar{\Omega} \in [0, 0.2]$ of interest.

Due to its constant propagation velocity, and slowly decaying amplitude, the "shock wave" can be regarded as a quasi-coherent wave structure on a ferrofluid thin film subjected to a rotating magnetic field. The main difference with the propagating interfacial wave discussed in Chapter 3 is the wave profile itself. When the interface is subjected to a static, tilt magnetic field, the coherent interfacial waves look like the so-called "cnoidal waves"

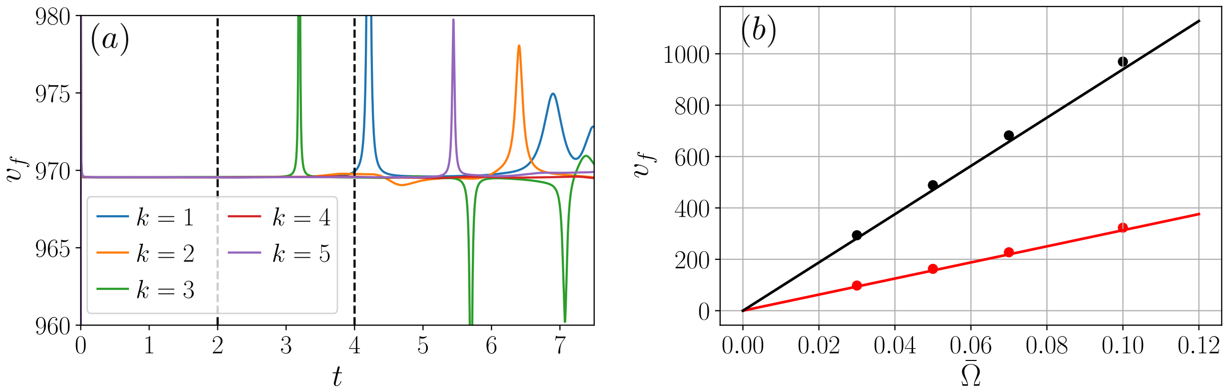

Figure 5.6. (a) The evolution of the phase velocity of the first five harmonic modes, which remain constant in the interval $t \in [0, 2]$ during the "shock wave" propagation. (b) The markers show the constant "shock wave" propagation speed extracted from the numerical simulations at different rotating frequencies $\bar{\Omega}$ for $\mathrm{N_B} = 1000$ (red) and $\mathrm{N_B} = 3000$ (black), while the solid curves show the phase velocity predicted from the imaginary part of the linear growth rate, $\mathrm{Im}\,[\Lambda(k)]/k$.

discussed in Chapter 3, which are nonlinear periodic waves generalizing sines and cosine. On the other hand, when the interface is subjected to a rotating magnetic field, the magnetic torque and body force tend to drive a "shock wave" with a steep front. This observation also indicates the different effects of the nonlinearity in these two long-wave thin-film equations. While the waves induced by the static field are characterized by the low-dimensional property (only the first few Fourier modes contain energy), as shown in Chapter 3 and discussed in Chapter 4, the formation of the steep "shock wave" in this chapter necessitates more harmonic modes to capture, as shown in Figs. 5.3(a) and 5.4(a). This difference naturally leads to the question to be answered in future work: *Without the low-dimensional property, how do we identify the nonlinear structures behaving like the "shock wave" state? Is there any unstable manifold that leads to further transient away from this state?*

Disordered wave interaction

While the "shock wave" propagation commonly exists for all parameter values investigated in this study, the disordered wave interaction only emerges for relatively large forcing frequency, *i.e.*, $\bar{\Omega} = 0.1$ with $\mathrm{N_B} = 1000, 3000$.

Taking the definition of the total energy $\mathcal{E}(t) \equiv \frac{1}{2}\int_{-\pi}^{+\pi} \eta(x,t)^2\,dx$ of the wave field as in Section 3.3.2, we can show the wave evolution in the energy phase plane $(\mathcal{E}, \dot{\mathcal{E}})$ as in Fig. 5.7. Different from Chapter 3, where the energy phase plane trajectories are attracted to fixed points, the trajectories on Fig. 5.7 do not appear to reach any attractor, but rather oscillate in a disorderly manner in the region $\mathcal{E} \in [2,5] \times 10^{-6}$. This region corresponds to the disordered wave interaction region $t \in [4, 32]$ seen in Fig. 5.4, which is featured by the long-time interaction and the bounded solution. This behavior is similar to the chaotic waves, which refers to the phenomenon of bounded nonperiodic evolution in completely deterministic nonlinear dynamical systems with sensitive dependence on initial conditions [102].

Thus, to better understand the disorder dynamics, we demonstrate the sensitive dependence on initial conditions. To this end, we conduct the simulation starting at nearby initial conditions. Figure 5.7(a) shows the trajectories in the energy phase plane for two initial conditions with $\mathrm{N_B} = 3000$, $\bar{\Omega} = 0.1$. One trajectory (black curve) starts from $f_a(x) = 1 + 0.0005\sin(x)$, while the second trajectory (red dashed curve) from $f_b(x) = 1 + 0.000501\sin(x)$. We see that the trajectories separate, displaying the divergence of dynamics emerging from nearby initial conditions. Figure 5.7(b) shows the norm of the relative difference between the trajectories (that is, $e = |(f_a - f_b)/f_a|$). We observe that the norm $\|e\|_2(t)$ grows irregularly with time, clearly indicating the sensitive dependence of the dynamics on the initial conditions.

The chaotic behavior of ferrofluids is not as well known as its controllable pattern formation. Nevertheless, chaotic dynamics of ferrofluids have been reported in several physical systems. Laroze, Siddheshwar, and Pleiner [144] studied thermally-driven convection of ferrofluids in two dimensions subjected to a static magnetic field. They reduce the complex dynamics to a generalized Lorenz model. Boyer and Falcon [145] reported the observation of wave turbulence on the surface of a ferrofluid that is mechanically forced and subjected

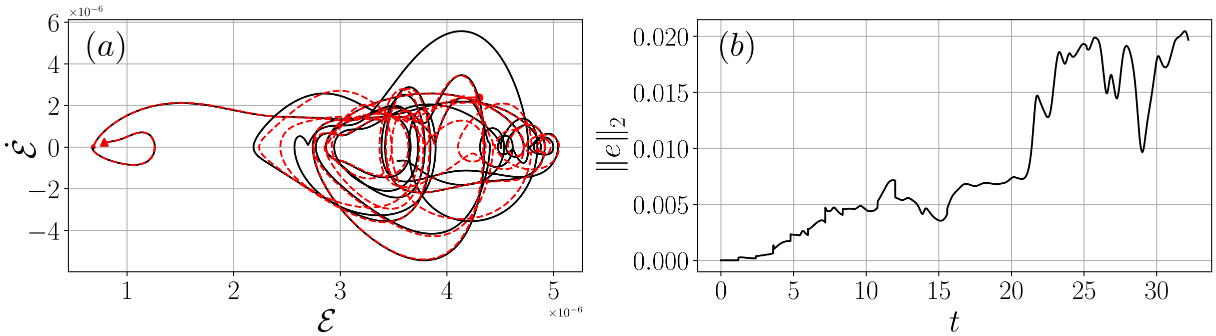

Figure 5.7. (a) Deviating trajectories in the energy phase plane show the chaotic feature of the long-wave equation, with initial condition $f_a(x) = 1 + 0.0005\sin(x)$ (black), and $f_b(x) = 1 + 0.000501\sin(x)$ (red dashed). (b) The norm of the difference between the dynamics $f(x,t)$ with $f(x,0) = f_a(x)$ and $f(x,0) = f_b(x)$.

to a static normal magnetic field. Surface waves arise only above a critical field strength. The turbulent flow of a ferrofluid in a channel subjected to an oscillating magnetic field was studied by Schumacher, Riley, and Finlayson [146] using direct numerical simulation. They concluded that the pressure drop required to maintain a constant flow rate is smaller than that for a steady magnetic field. Meanwhile, Altmeyer, Do, and Lai [147] suggest that turbulence can occur at low Reynolds numbers in rotating ferrofluids. This work shows how a steady or time-dependent magnetic field can modify the dynamics. However, to the best of our knowledge, the current work is the first time when the chaotic interfacial wave is induced directly by the rotating, time-dependent magnetic field.

Kirkinis [78] also included the effect of the surface torque in a long-wave thin-film equation. In this case, the surface torque is approximated as constant, thus the impact of the interface's deformation on the torque is neglected. In this work, the permanent traveling wave is reported to arise from the balance between the torque and the van der Waals forces. Meanwhile, in this work, when the torque is balanced with surface tension and derived via a consistent scaling of the governing equations, the effect of the magnetic torque in Eq. (5.49) reveals more complicated dynamics in both space and time than observed in [78]. In future work, we will further characterize the dynamics using different approaches, such as bifurcation diagrams and Lyapunov exponents. We plan to investigate an extensive parameters study and reveal the route to chaos, as has been done for the KSE and the generalized KSE [113], [148].

5.5 Discussion

As discussed in Chapter 1, the configuration of the magnetic fields plays a crucial role in determining the effect of the magnetic forces on a ferrofluid interface, specifically, these forces can either stabilize or destabilize it. By harnessing these effects and balancing them with other external forces, it is possible to achieve desired functionalities. While the forces from various static magnetic fields have been investigated, the use of a time-dependent rotating magnetic field remains relatively less explored. A rotating magnetic field introduces unique features such as a shear-like torque on the surface, which can provide a new mechanism for coherent wave propagation on a ferrofluid interface. It is intriguing to study how this torque-induced motion interacts with other forces, such as viscous shear or gravity. An investigation in this direction can be found in [149], wherein experiments were conducted to demonstrate the sliding behavior of deformed ferrofluid droplets subjected to shear in a channel. In another study [150], both experiment and theory were employed to showcase how a nonuniform magnetic field can reverse the draining of a vertical magnetic soap film. In [151], a long-wave equation is derived for a ferrofluid film flowing down an inclined substrate with a nonlinear magnetization. Notably, the magnetic fields in these works were static. Investigating how forces arising from a rotating magnetic field can compete against other external forces, such as gravity or viscous shear, and understanding how the interaction between magnetic torque and these forces affects the dynamic response of a ferrofluid, can provide valuable insights into the development of novel functionalities in, *e.g.*, soft robots.

Another promising direction worth pursuing is the exploration of nonlinear dynamics in active colloidal systems. Ferrofluids consist of self-driven particles with individual dynamics that collectively exhibit macroscopic coherent motions. Under time-varying magnetic fields, the ferrofluid particles can be categorized as one type of active colloid, utilizing energy input at the particle level to propel persistent motion at the continuum level. Other types of active colloids can be driven by chemical reactions [152], [153] or electric fields [154], [155], and even motile bacteria in suspensions can be considered as active colloids [156], [157]. While agent-based (particle-level) simulations can be computationally expensive, the continuum approach enables the study of large-scale systems. By generalizing the Navier–Stokes equations to take into account the asymmetric stress, a model was developed that can capture the surface waves observed in experiments on active colloidal suspensions [76]. Another model derived for Quincke spinners in an electric field reveals turbulence-like motion [155]. The emergence of similar behaviors in the current model of a ferrofluid thin-film subject to magnetic torques, specifically the surface waves and chaotic states, motivates us to further advance our understanding of their complex nonlinear dynamics. Active colloids represent a vibrant area of research [1], [2], and the development of simple, interpretable models coupled with the exploration of fundamental principles governing their behavior will accelerate the progress in developing new technologies and materials with unique properties.

6. CONCLUSION

In this thesis, we proposed a novel magnetic field configuration that induces the deformation and steady spinning of a confined circular ferrofluid droplet, resembling a "gear," driven by interfacial traveling waves. To investigate the nonlinear evolution of such ferrofluids interfaces, we employed a combination of numerical simulations and mathematical modeling. By successive reduction of the fully nonlinear problem to different levels of simplification (while keeping only the key physics), we uncovered rich dynamic features, which we analyzed from various perspectives. In doing so, we developed long-wave models to study wave propagation and amplitude equations to characterize bifurcations. In turn, these mathematical frameworks enabled the design of time-dependent strategies for non-invasive control of ferrofluid interfaces. Furthermore, we extend our work to explore the effects of fast time-varying magnetic fields, characterized by new physics such as an asymmetric stress tensor and the existence of magnetic point torques in the continuum model.

Specifically, the chapter-wise accomplishments of this thesis are:

- **Chapter 2:** This study demonstrated how a perturbed circular ferrofluid droplet can evolve into a nonlinearly stable rotating shape. The most unstable mode sets how perturbations evolve into a permanent profile characterized by skewness and asymmetry. Through the integration of weakly nonlinear theory and fully nonlinear simulations, we uncovered the emergence of permanent rotating shapes driven by interfacial traveling waves, with predictable propagation velocities. Additionally, our investigation revealed how the coupling of magnetic field components alters asymmetry and nonlinear instability, giving rise to phenomena akin to "wave breaking." The nonlinear analysis conducted in this study lays the foundation for future design and experimental implementation of a stable rotating ferrofluid microswimmer system.

- **Chapter 3:** The dynamics of long, small-amplitude nonlinear waves on the interface of a thin ferrofluid film was analyzed for the configuration of a horizontal Hele-Shaw flow subjected to a tilted magnetic field. We showed that such ferrofluid interfaces support periodic traveling waves governed by a modified KS-type equation. A linear stability analysis and a nonlinear energy budget were employed to reveal that the balance between stabilizing surface tension forces (energy sink/loss) and destabilizing magnetic forces (energy source/gain) leads to the generation of dissipative solitons on the ferrofluid interface. Our results lead to a quantitative understanding of these nonlinear periodic traveling wave profiles, and how interfacial waves can be generated and controlled (specifically, their propagation velocity and shape) non-invasively by an external magnetic field. A multiple-scale analysis provides a weakly nonlinear correction to the propagation velocity of harmonic waves. This calculation also reveals how the marginally unstable linear solution is equilibrated by weak nonlinearity and tends to the permanent traveling wave solution. This long-wave equation has rich dynamics, such as transitions between different nonlinear periodic states and long-lived multi-periodic wave profiles.

- **Chapter 4:** In this study, we reduced the nonlinear system introduced in Chapter 2 to a finite set of ODEs, demonstrating that a periodic traveling wave on the droplet's interface is stable, and its dynamics is governed by a Hopf bifurcation at the critical growth rate. A center manifold reduction shows the geometrical equivalence between a two-harmonic-mode coupled ODE system describing the interface evolution and a supercritical Hopf bifurcation. This reduction is supported by the amplitude (Landau) equation derived from a multiple-time scale analysis. Both methods adequately predict the fully nonlinear evolution, as demonstrated by comparisons between the theory and fully nonlinear, interface-resolved simulations of the original PDE system. Next, with the reduced model revealing the key dynamical features, we designed a slowly-varying radial magnetic field such that the timing of the emergence of the spinning "gear" can be controlled. This work is inspired by the well-known delay behavior of dynamic Hopf bifurcations. In this study, the delay time is predicted based on the fact that the time-varying amplitude equation finally saturates to the quasistatic amplitude. This time can be manipulated purely via an external magnetic field by controlling the linear growth rate and its rate of change. We also studied the evolution under a time-reversed magnetic field. While we found that the evolution of the droplet is irreversible due to the nonlinearity in the interface condition, the reverse evolution, and the final stated achieved under it, can still be well approximated by the reversed amplitude equation.

- **Chapter 5:** In this work, we developed a long-wave equation model for a thin film subjected to the in-plane rotating magnetic field. The model incorporates special surface boundary conditions, where the viscous shear force is balanced by the surface torque through consistent scaling. Through linear stability analysis, we identified the rotating field as a mechanism of destabilization of the flat interface and a mechanism for generating propagating waves. These predictions were validated through nonlinear simulations of the governing long-wave, thin-film equation. We found that, beyond the linear regime, the dynamics become increasingly complex, characterized by the emergence of "shock waves" from small harmonic perturbations and the presence of long-lasting "chaotic" states. These observations suggest the presence of something akin to "active turbulence," opening up exciting new avenues for further exploration. For example, it may be that these dynamics could be observed in experiments with active colloids.

REFERENCES

[1] M. C. Marchetti, J. F. Joanny, S. Ramaswamy, *et al.*, "Hydrodynamics of soft active matter," *Rev. Mod. Phys.*, vol. 85, pp. 1143–1189, 2013. DOI: 10.1103/RevModPhys.85.1143.

[2] D. Saintillan, "Rheology of Active Fluids," *Annu. Rev. Fluid Mech.*, vol. 50, pp. 563–592, 2018. DOI: 10.1146/annurev-fluid-010816-060049.

[3] A. Sokolov, M. M. Apodaca, B. A. Grzybowski, and I. S. Aranson, "Swimming bacteria power microscopic gears," *Proc. Natl Acad. Sci. USA*, vol. 107, pp. 969–974, 2010. DOI: 10.1073/pnas.0913015107.

[4] G. Z. Lum, Z. Ye, X. Dong, *et al.*, "Shape-programmable magnetic soft matter," *Proc. Natl Acad. Sci. USA*, vol. 113, E6007–E6015, 2016. DOI: 10.1073/pnas.1608193113.

[5] T. Xu, J. Zhang, M. Salehizadeh, O. Onaizah, and E. Diller, "Millimeter-scale flexible robots with programmable three-dimensional magnetization and motions," *Science Robotics*, vol. 4, eaav4494, 2019. DOI: 10.1126/scirobotics.aav4494.

[6] J. Giltinan, P. Katsamba, W. Wang, E. Lauga, and M. Sitti, "Selectively controlled magnetic microrobots with opposing helices," *Appl. Phys. Lett.*, vol. 116, p. 134 101, 2020. DOI: 10.1063/1.5143007.

[7] B. J. Nelson, I. K. Kaliakatsos, and J. J. Abbott, "Microrobots for Minimally Invasive Medicine," *Annu. Rev. Biomed. Eng.*, vol. 12, pp. 55–85, 2010. DOI: 10.1146/annurev-bioeng-010510-103409.

[8] R. Rosensweig, *Ferrohydrodynamics*. Mineola, NY: Dover Publications, 2014, Republication of the 1997 edition.

[9] E. Blums, A. Cebers, and M. Maiorov, *Magnetic Fluids*. Berlin: De Gruyter, 1997. DOI: 10.1515/9783110807356.

[10] I. Torres-Díaz and C. Rinaldi, "Recent progress in ferrofluids research: Novel applications of magnetically controllable and tunable fluids," *Soft Matter*, vol. 10, pp. 8584–8602, 2014. DOI: 10.1039/C4SM01308E.

[11] P. Voltairas, D. Fotiadis, and L. Michalis, "Hydrodynamics of magnetic drug targeting," *J. Biomech.*, vol. 35, pp. 813–821, 2002. DOI: 10.1016/S0021-9290(02)00034-9.

[12] F. Serwane, A. Mongera, P. Rowghanian, *et al.*, "In vivo quantification of spatially varying mechanical properties in developing tissues," *Nat. Methods*, vol. 14, pp. 181–186, 2017. DOI: 10.1038/nmeth.4101.

[13] X. Fan, X. Dong, A. C. Karacakol, H. Xie, and M. Sitti, "Reconfigurable multifunctional ferrofluid droplet robots," *Proc. Natl Acad. Sci. USA*, vol. 117, pp. 27 916–27 926, 2020. DOI: 10.1073/pnas.2016388117.

[14] R. Ahmed, M. Ilami, J. Bant, B. Beigzadeh, and H. Marvi, "A shapeshifting ferrofluidic robot," *Soft Robotics*, 2020. DOI: 10.1089/soro.2019.0184.

[15] P. Dunne, T. Adachi, A. A. Dev, *et al.*, "Liquid flow and control without solid walls," *Nature*, vol. 581, pp. 58–62, 2020. DOI: 10.1038/s41586-020-2254-4.

[16] L. C. Morrow, T. J. Moroney, and S. W. McCue, "Numerical investigation of controlling interfacial instabilities in non-standard Hele-Shaw configurations," *J. Fluid Mech.*, vol. 877, pp. 1063–1097, 2019. DOI: 10.1017/jfm.2019.623.

[17] P. G. Saffman and G. Taylor, "The penetration of a fluid into a porous medium or Hele-Shaw cell containing a more viscous liquid," *Proc. R. Soc. Lond. A*, vol. 245, pp. 312–329, 1958. DOI: 10.1098/rspa.1958.0085.

[18] D. Bensimon, L. P. Kadanoff, S. Liang, B. I. Shraiman, and C. Tang, "Viscous flows in two dimensions," *Rev. Mod. Phys.*, vol. 58, pp. 977–999, 1986. DOI: 10.1103/RevModPhys.58.977.

[19] G. M. Homsy, "Viscous fingering in porous media," *Annu. Rev. Fluid Mech.*, vol. 19, pp. 271–311, 1987. DOI: 10.1146/annurev.fl.19.010187.001415.

[20] M. Zeybek and Y. C. Yortsos, "Long waves in parallel flow in Hele-Shaw cells," *Phys. Rev. Lett.*, vol. 67, pp. 1430–1433, 1991. DOI: 10.1103/PhysRevLett.67.1430.

[21] M. Zeybek and Y. C. Yortsos, "Parallel flow in Hele-Shaw cells," *J. Fluid Mech.*, vol. 241, pp. 421–442, 1992. DOI: 10.1017/S0022112092002106.

[22] F. Charru and J. Fabre, "Theoretical and Experimental Investigation of Periodic Interfacial Waves Between Two Viscous Fluid Layers," in *Instabilities in Multiphase Flows*, G. Gouesbet and A. Berlemont, Eds., Boston, MA: Springer US, 1993, pp. 205–217. DOI: 10.1007/978-1-4899-1594-8_17.

[23] P. Gondret and M. Rabaud, "Shear instability of two-fluid parallel flow in a Hele–Shaw cell," *Phys. Fluids*, vol. 9, pp. 3267–3274, 1997. DOI: 10.1063/1.869441.

[24] L. Meignin, P. Gondret, C. Ruyer-Quil, and M. Rabaud, "Subcritical Kelvin–Helmholtz instability in a Hele-Shaw cell," *Phys. Rev. Lett.*, vol. 90, p. 234 502, 2003. DOI: 10.1103/PhysRevLett.90.234502.

[25] F. Plouraboué and E. J. Hinch, "Kelvin–Helmholtz instability in a Hele-Shaw cell," *Phys. Fluids*, vol. 14, pp. 922–929, 2002. DOI: 10.1063/1.1446884.

[26] E. J. Hinch and F. Plouraboué, "Kelvin–Helmholtz instability in a Hele-Shaw cell: Large effect from the small region near the meniscus," *Phys. Fluids*, vol. 17, p. 052 107, 2005. DOI: 10.1063/1.1914729.

[27] S. A. Lira and J. A. Miranda, "Ferrofluid patterns in Hele-Shaw cells: Exact, stable, stationary shape solutions," *Phys. Rev. E*, vol. 93, p. 013 129, 2016. DOI: 10.1103/PhysRevE.93.013129.

[28] A. Prosperetti, "Boundary Integral Methods," in *Drop-Surface Interactions*, M. Rein, Ed., Wien: Springer-Verlag, 2002, pp. 219–235. DOI: 10.1007/978-3-7091-2594-6_7.

[29] M. J. Shelley, "A study of singularity formation in vortex-sheet motion by a spectrally accurate vortex method," *J. Fluid Mech.*, vol. 244, pp. 493–526, 1992. DOI: 10.1017/S0022112092003161.

[30] M. J. Shelley, F.-R. Tian, and K. Wlodarski, "Hele-Shaw flow and pattern formation in a time-dependent gap," *Nonlinearity*, vol. 10, pp. 1471–1495, 1997. DOI: 10.1088/0951-7715/10/6/005.

[31] A. Cebers and M. M. Maiorov, "Magnetostatic instabilities in plane layers of magnetizable fluids," *Magnetohydrodynamics*, vol. 16, pp. 21–27, 1980.

[32] A. Cebers and M. M. Maiorov, "Structures of interface a bubble and magnetic fluid in a field," *Magnetohydrodynamics*, vol. 16, pp. 231–235, 1980.

[33] S. A. Langer, R. E. Goldstein, and D. P. Jackson, "Dynamics of labyrinthine pattern formation in magnetic fluids," *Phys. Rev. A*, vol. 46, pp. 4894–4904, 1992. DOI: 10.1103/PhysRevA.46.4894.

[34] D. P. Jackson, R. E. Goldstein, and A. O. Cebers, "Hydrodynamics of fingering instabilities in dipolar fluids," *Phys. Rev. E*, vol. 50, pp. 298–307, 1994. DOI: 10.1103/PhysRevE.50.298.

[35] H. Li, C.-Y. Kao, and C.-Y. Wen, "Labyrinthine and secondary wave instabilities of a miscible magnetic fluid drop in a Hele-Shaw cell," *J. Fluid Mech.*, vol. 836, pp. 374–396, 2018. DOI: 10.1017/jfm.2017.739.

[36] R. M. Oliveira, J. A. Miranda, and E. S. G. Leandro, "Ferrofluid patterns in a radial magnetic field: Linear stability, nonlinear dynamics, and exact solutions," *Phys. Rev. E*, vol. 77, p. 016 304, 2008. DOI: 10.1103/PhysRevE.77.016304.

[37] S. A. Lira, J. A. Miranda, and R. M. Oliveira, "Stationary shapes of confined rotating magnetic liquid droplets," *Phys. Rev. E*, vol. 82, p. 036 318, 2010. DOI: 10.1103/PhysRevE.82.036318.

[38] E. O. Dias and J. A. Miranda, "Azimuthal field instability in a confined ferrofluid," *Phys. Rev. E*, vol. 91, p. 023 020, 2015. DOI: 10.1103/PhysRevE.91.023020.

[39] D. P. Jackson and J. A. Miranda, "Confined ferrofluid droplet in crossed magnetic fields," *Eur. Phys. J. E*, vol. 23, pp. 389–396, 2007. DOI: 10.1140/epje/i2007-10199-x.

[40] J. A. Miranda and M. Widom, "Parallel flow in Hele-Shaw cells with ferrofluids," *Phys. Rev. E*, vol. 61, pp. 2114–2117, 2000. DOI: 10.1103/PhysRevE.61.2114.

[41] S. A. Lira and J. A. Miranda, "Nonlinear traveling waves in confined ferrofluids," *Phys. Rev. E*, vol. 86, p. 056 301, 2012. DOI: 10.1103/PhysRevE.86.056301.

[42] T. T. Al-Housseiny, P. A. Tsai, and H. A. Stone, "Control of interfacial instabilities using flow geometry," *Nat. Phys.*, vol. 8, pp. 747–750, 2012. DOI: 10.1038/nphys2396.

[43] D. Pihler-Puzović, P. Illien, M. Heil, and A. Juel, "Suppression of complex fingerlike patterns at the interface between air and a viscous fluid by elastic membranes," *Phys. Rev. Lett.*, vol. 108, p. 074 502, 2012. DOI: 10.1103/PhysRevLett.108.074502.

[44] M. Mirzadeh and M. Z. Bazant, "Electrokinetic Control of Viscous Fingering," *Phys. Rev. Lett.*, vol. 119, p. 174 501, 2017. DOI: 10.1103/PhysRevLett.119.174501.

[45] J. A. Miranda, "Rotating Hele-Shaw cells with ferrofluids," *Phys. Rev. E*, vol. 62, pp. 2985–2988, 2000. DOI: 10.1103/PhysRevE.62.2985.

[46] S. S. S. Cardoso and A. W. Woods, "The formation of drops through viscous instability," *J. Fluid Mech.*, vol. 289, pp. 351–378, 1995. DOI: 10.1017/S0022112095001364.

[47] S. Li, J. S. Lowengrub, J. Fontana, and P. Palffy-Muhoray, "Control of Viscous Fingering Patterns in a Radial Hele-Shaw Cell," *Phys. Rev. Lett.*, vol. 102, p. 174 501, 2009. DOI: 10.1103/PhysRevLett.102.174501.

[48] Z. Zheng, H. Kim, and H. A. Stone, "Controlling viscous fingering using time-dependent strategies," *Phys. Rev. Lett.*, vol. 115, p. 174 501, 2015. DOI: 10.1103/PhysRevLett.115.174501.

[49] P. H. A. Anjos, M. Zhao, J. Lowengrub, and S. Li, "Electrically controlled self-similar evolution of viscous fingering patterns," *Phys. Rev. Fluids*, vol. 7, p. 053 903, 2022. DOI: 10.1103/PhysRevFluids.7.053903.

[50] E. Knobloch and R. Krechetnikov, "Problems on time-varying domains: Formulation, dynamics, and challenges," *Acta Appl. Math.*, vol. 137, pp. 123–157, 2015. DOI: 10.1007/s10440-014-9993-x.

[51] M. Ghadiri and R. Krechetnikov, "Pattern formation on time-dependent domains," *J. Fluid Mech.*, vol. 880, pp. 136–179, 2019. DOI: 10.1017/jfm.2019.659.

[52] E. Knobloch and R. Krechetnikov, "Stability on time-dependent domains," *J. Nonlinear Sci.*, vol. 24, pp. 493–523, 2014. DOI: 10.1007/s00332-014-9197-6.

[53] E. Hopf, "A mathematical example displaying features of turbulence," *Commun. Pure Appl. Math.*, vol. 1, pp. 303–322, 1948. DOI: 10.1002/cpa.3160010401.

[54] E. N. Lorenz, "Deterministic nonperiodic flow," *J. Atmos. Sci.*, vol. 20, pp. 130–141, 1963. DOI: 10.1175/1520-0469(1963)020<0130:DNF>2.0.CO;2.

[55] A. Franco-Gómez, A. B. Thompson, A. L. Hazel, and A. Juel, "Bubble propagation in Hele-Shaw channels with centred constrictions," *Fluid Dyn. Res.*, vol. 50, p. 021 403, 2018. DOI: 10.1088/1873-7005/aaa5cf.

[56] J. S. Keeler, A. B. Thompson, G. Lemoult, A. Juel, and A. L. Hazel, "The influence of invariant solutions on the transient behaviour of an air bubble in a Hele-Shaw channel," *Proc. R. Soc. A*, vol. 475, p. 20 190 434, 2019. DOI: 10.1098/rspa.2019.0434.

[57] J. A. Miranda and M. Widom, "Radial fingering in a Hele-Shaw cell: A weakly nonlinear analysis," *Physica D*, vol. 120, pp. 315–328, 1998. DOI: 10.1016/S0167-2789(98)00097-9.

[58] J. A. Miranda and R. M. Oliveira, "Time-dependent gap Hele-Shaw cell with a ferrofluid: Evidence for an interfacial singularity inhibition by a magnetic field," *Phys. Rev. E*, vol. 69, p. 066 312, 2004. DOI: 10.1103/PhysRevE.69.066312.

[59] P. H. A. Anjos, S. A. Lira, and J. A. Miranda, "Fingering patterns in magnetic fluids: Perturbative solutions and the stability of exact stationary shapes," *Phys. Rev. Fluids*, vol. 3, p. 044 002, 2018. DOI: 10.1103/PhysRevFluids.3.044002.

[60] M. Shliomis, "Effective viscosity of magnetic suspensions," *Sov. Phys. JETP*, vol. 34, pp. 1291–1294, 1972. [Online]. Available: http://jetp.ras.ru/cgi-bin/e/index/e/34/6/p1291?a=list.

[61] M. I. Shliomis and K. I. Morozov, "Negative viscosity of ferrofluid under alternating magnetic field," *Phys. Fluids*, vol. 6, pp. 2855–2861, 1994. DOI: 10.1063/1.868108.

[62] M. Zahn and D. R. Greer, "Ferrohydrodynamic pumping in spatially uniform sinusoidally time-varying magnetic fields," *J. Magn. Magn. Mater.*, vol. 149, pp. 165–173, 1995. DOI: 10.1016/0304-8853(95)00363-0.

[63] A. Krekhov and M. Shliomis, "Spontaneous core rotation in ferrofluid pipe flow," *Phys. Rev. Lett.*, vol. 118, p. 114 503, 2017. DOI: 10.1103/PhysRevLett.118.114503.

[64] C. Singh, A. K. Das, and P. K. Das, "Flow restrictive and shear reducing effect of magnetization relaxation in ferrofluid cavity flow," *Phys. Fluid*, vol. 28, p. 087 103, 2016. DOI: 10.1063/1.4960085.

[65] S. A. Altmeyer, "Ferrofluidic wavy Taylor vortices under alternating magnetic field," *Phil. Trans. R. Soc. A*, vol. 381, p. 20 220 121, 2023. DOI: 10.1098/rsta.2022.0121.

[66] S. Rhodes, J. Perez, S. Elborai, S.-H. Lee, and M. Zahn, "Ferrofluid spiral formations and continuous-to-discrete phase transitions under simultaneously applied DC axial and AC in-plane rotating magnetic fields," *J. Magn. Magn. Mater.*, vol. 289, pp. 353–355, 2005. DOI: 10.1016/j.jmmm.2004.11.100.

[67] R. Moskowitz and R. E. Rosensweig, "Nonmechanical torque-driven flow of a ferromagnetic fluid by an electromagnetic field," *Appl. Phys. Lett.*, vol. 11, pp. 301–303, 1967. DOI: 10.1063/1.1754952.

[68] V. Zaitsev and M. Shliomis, "Entrainment of ferromagnetic suspension by a rotating field," *J. Appl. Mech. Tech. Phys.*, vol. 10, pp. 696–700, 1969. DOI: 10.1007/BF00907424.

[69] R. Rosensweig, J. Popplewell, and R. Johnston, "Magnetic fluid motion in rotating field," *J. Magn. Magn. Mater.*, vol. 85, pp. 171–180, 1990. DOI: 10.1016/0304-8853(90)90046-S.

[70] A. Chaves, C. Rinaldi, S. Elborai, X. He, and M. Zahn, "Bulk flow in ferrofluids in a uniform rotating magnetic field," *Phys. Rev. Lett.*, vol. 96, p. 194 501, 2006. DOI: 10.1103/PhysRevLett.96.194501.

[71] M. I. Shliomis, "How a rotating magnetic field causes ferrofluid to rotate," *Phys. Rev. Fluids*, vol. 6, p. 043 701, 2021. DOI: 10.1103/PhysRevFluids.6.043701.

[72] C. Rinaldi, X. He, A. Rosenthal, T. Franklin, C. Lorenz, and M. Zahn, "Rheology and behavior of magnetic fluids in alternating/rotating magnetic fields," in *Proceedings of the ASME/JSME 2003 4th Joint Fluids Summer Engineering Conference*, vol. 2, Honolulu, Hawaii, 2003, pp. 1565–1570. DOI: 10.1115/FEDSM2003-45039.

[73] S. E. Rhodes, "Magnetic fluid flow phenomena in DC and rotating magnetic fields," Ph.D. dissertation, Massachusetts Institute of Technology, 2004. [Online]. Available: https://dspace.mit.edu/handle/1721.1/17670.

[74] S. Elborai, D.-K. Kim, X. He, S.-H. Lee, S. Rhodes, and M. Zahn, "Self-forming, quasi-two-dimensional, magnetic-fluid patterns with applied in-plane-rotating and dc-axial magnetic fields," *J. Appl. Phys.*, vol. 97, 10Q303, 2005. DOI: 10.1063/1.1851453.

[75] D. Rannacher and A. Engel, "Suppressing the Rayleigh-Taylor instability with a rotating magnetic field," *Phys. Rev. E*, vol. 75, p. 016 311, 2007. DOI: 10.1103/PhysRevE.75.016311.

[76] V. Soni, E. S. Bililign, S. Magkiriadou, *et al.*, "The odd free surface flows of a colloidal chiral fluid," *Nat. Phys.*, vol. 15, pp. 1188–1194, 2019. DOI: 10.1038/s41567-019-0603-8.

[77] D. Reynolds, G. M. Monteiro, and S. Ganeshan, "Hele-Shaw flow for parity odd three-dimensional fluids," *Phys. Rev. Fluids*, vol. 7, p. 114 201, 2022. DOI: 10.1103/PhysRevFluids.7.114201.

[78] E. Kirkinis, "Magnetic torque-induced suppression of van-der-Waals-driven thin liquid film rupture," *J. Fluid Mech.*, vol. 813, pp. 991–1006, 2017. DOI: 10.1017/jfm.2016.850.

[79] R. E. Rosensweig, M. Zahn, and R. Shumovich, "Labyrinthine instability in magnetic and dielectric fluids," *J. Magn. Magn. Mater.*, vol. 39, pp. 127–132, 1983. DOI: 10.1016/0304-8853(83)90416-X.

[80] M. Remoissenet, *Waves Called Solitons: Concepts and Experiments* (Advanced Texts in Physics). Berlin/Heidelberg: Springer, 1999. DOI: 10.1007/978-3-662-03790-4.

[81] S. Kalliadasis and U. Thiele, Eds., *Thin Films of Soft Matter* (CISM International Centre for Mechanical Sciences). Vienna: Springer, 2007, vol. 490. DOI: 10.1007/978-3-211-69808-2.

[82] C. Rinaldi and M. Zahn, "Effects of spin viscosity on ferrofluid flow profiles in alternating and rotating magnetic fields," *Phys. Fluids*, vol. 14, pp. 2847–2870, 2002. DOI: 10.1063/1.1485762.

[83] Z. Yu and I. C. Christov, "Tuning a magnetic field to generate spinning ferrofluid droplets with controllable speed via nonlinear periodic interfacial waves," *Phys. Rev. E*, vol. 103, p. 013 103, 2021. DOI: 10.1103/PhysRevE.103.013103.

[84] D. Rannacher and A. Engel, "Cylindrical Korteweg–de Vries solitons on a ferrofluid surface," *New. J. Phys.*, vol. 8, pp. 108–108, 2006. DOI: 10.1088/1367-2630/8/6/108.

[85] P. H. A. Anjos, G. D. Carvalho, S. A. Lira, and J. A. Miranda, "Wrinkling and folding patterns in a confined ferrofluid droplet with an elastic interface," *Phys. Rev. E*, vol. 99, p. 022 608, 2019. DOI: 10.1103/PhysRevE.99.022608.

[86] A. J. Roberts, "A stable and accurate numerical method to calculate the motion of a sharp interface between fluids," *IMA J. Appl. Math.*, vol. 31, pp. 13–35, 1983. DOI: 10.1093/imamat/31.1.13.

[87] P. G. Kevrekidis, D. E. Pelinovsky, and A. Saxena, "When Linear Stability Does Not Exclude Nonlinear Instability," *Phys. Rev. Lett.*, vol. 114, p. 214 101, 2015. DOI: 10.1103/PhysRevLett.114.214101.

[88] A. B. Kennedy, Q. Chen, J. T. Kirby, and R. A. Dalrymple, "Boussinesq modeling of wave transformation, breaking, and runup. I: 1D," *J. Waterw. Port. Coast.*, vol. 126, pp. 39–47, 2000. DOI: 10.1061/(ASCE)0733-950X(2000)126:1(39).

[89] T. J. Maccarone, "The biphase explained: Understanding the asymmetries in coupled Fourier components of astronomical time series," *Mon. Not. R. Astron. Soc.*, vol. 435, pp. 3547–3558, 2013. DOI: 10.1093/mnras/stt1546.

[90] N. J. Zabusky and M. D. Kruskal, "Interaction of "Solitons" in a Collisionless Plasma and the Recurrence of Initial States," *Phys. Rev. Lett.*, vol. 15, pp. 240–243, 1965. DOI: 10.1103/PhysRevLett.15.240.

[91] J. L. Bona, P. E. Souganidis, and W. A. Strauss, "Stability and instability of solitary waves of Korteweg-de Vries type," *Proc. R. Soc. Lond. A*, vol. 411, pp. 395–412, 1987. DOI: 10.1098/rspa.1987.0073.

[92] E. O. Dias and J. A. Miranda, "Control of radial fingering patterns: A weakly nonlinear approach," *Phys. Rev. E*, vol. 81, p. 016 312, 2010. DOI: 10.1103/PhysRevE.81.016312.

[93] E. S. G. Leandro, R. M. Oliveira, and J. A. Miranda, "Geometric approach to stationary shapes in rotating Hele–Shaw flows," *Physica D*, vol. 237, pp. 652–664, 2008. DOI: 10.1016/j.physd.2007.10.005.

[94] G. Birkhoff, "Taylor instability and laminar mixing," Los Alamos Scientific Laboratory, Tech. Rep. LA-1862, 1954. [Online]. Available: https://www.osti.gov/biblio/4372366-taylor-instability-laminar-mixing.

[95] T. Soomere, "Solitons Interactions," in *Encyclopedia of Complexity and Systems Science*, R. A. Meyers, Ed., New York, NY: Springer, 2009, pp. 8479–8504. DOI: 10.1007/978-0-387-30440-3_507.

[96] E. Bourdin, J.-C. Bacri, and E. Falcon, "Observation of Axisymmetric Solitary Waves on the Surface of a Ferrofluid," *Phys. Rev. Lett.*, vol. 104, p. 094 502, 2010. DOI: 10.1103/PhysRevLett.104.094502.

[97] A. R. Osborne, E. Segre, G. Boffetta, and L. Cavaleri, "Soliton basis states in shallow-water ocean surface waves," *Phys. Rev. Lett.*, vol. 67, pp. 592–595, 1991. DOI: 10.1103/PhysRevLett.67.592.

[98] E. O. Dias, S. A. Lira, and J. A. Miranda, "Interfacial patterns in magnetorheological fluids: Azimuthal field-induced structures," *Phys. Rev. E*, vol. 92, p. 023 003, 2015. DOI: 10.1103/PhysRevE.92.023003.

[99] E. Álvarez-Lacalle, J. Ortín, and J. Casademunt, "Nonlinear Saffman-Taylor instability," *Phys. Rev. Lett.*, vol. 92, p. 054 501, 2004. DOI: 10.1103/PhysRevLett.92.054501.

[100] Z. Yu and I. C. Christov, "Long-wave equation for a confined ferrofluid interface: Periodic interfacial waves as dissipative solitons," *Proc. R. Soc. A*, vol. 477, p. 20 210 550, 2021. DOI: 10.1098/rspa.2021.0550.

[101] L. Rigo, D. Biau, and X. Gloerfelt, "Flow in a weakly curved square duct: Assessment and extension of Dean's model," *Phys. Rev. Fluids*, vol. 6, p. 024 101, 2021. DOI: 10.1103/PhysRevFluids.6.024101.

[102] M. Lakshmanan and S. Rajaseekar, *Nonlinear dynamics: Integrability, Chaos and Patterns*. Berlin/Heidelberg: Springer-Verlag, 2003. DOI: 10.1007/978-3-642-55688-3.

[103] D. J. Benney, "Long Waves on Liquid Films," *J. Math. and Phys.*, vol. 45, pp. 150–155, 1966. DOI: 10.1002/sapm1966451150.

[104] R. W. Atherton and G. M. Homsy, "On the derivation of evolution equations for interfacial waves," *Chem. Eng. Commun.*, vol. 2, pp. 57–77, 1976. DOI: 10.1080/00986447608960448.

[105] G. M. Homsy, "Model Equations for Wavy Viscous Film Flow," in *Nonlinear wave motion*, ser. Lectures in Applied Mathematics, A. C. Newell, Ed., vol. 15, Providence, R.I.: American Mathematical Society, 1974, pp. 191–194.

[106] C. I. Christov and M. G. Velarde, "Dissipative solitons," *Physica D*, vol. 86, pp. 323–347, 1995. DOI: 10.1016/0167-2789(95)00111-G.

[107] B. Straughan, *The Energy Method, Stability, and Nonlinear Convection* (Applied Mathematical Sciences), 2nd ed. New York, NY: Springer-Verlag, 2004, vol. 91. DOI: 10.1007/978-0-387-21740-6.

[108] S. Venkatasubramanian and P. N. Kaloni, "Stability and uniqueness of magnetic fluid motions," *Proc. R. Soc. Lond. A*, vol. 458, pp. 1189–1204, 2002. DOI: 10.1098/rspa.2001.0911.

[109] J. Shen, T. Tang, and L.-L. Wang, *Spectral Methods: Algorithms, Analysis and Applications*. Berlin/Heidelberg: Springer-Verlag, 2011. DOI: 10.1007/978-3-540-71041-7.

[110] A.-K. Kassam and L. N. Trefethen, "Fourth-order time-stepping for stiff PDEs," *SIAM J. Sci. Comput.*, vol. 26, pp. 1214–1233, 2005. DOI: 10.1137/S1064827502410633.

[111] A. L. Bertozzi and M. C. Pugh, "Long-wave instabilities and saturation in thin film equations," *Comm. Pure Appl. Math.*, vol. 51, pp. 625–661, 1998. DOI: 10.1002/(SICI)1097-0312(199806)51:6<625::AID-CPA3>3.0.CO;2-9.

[112] J. Kevorkian and J. D. Cole, *Multiple Scale and Singular Perturbation Methods* (Applied Mathematical Sciences). New York, NY: Springer New York, 1996, vol. 114. DOI: 10.1007/978-1-4612-3968-0.

[113] D. T. Papageorgiou and Y. S. Smyrlis, "The route to chaos for the Kuramoto–Sivashinsky equation," *Theoret. Comput. Fluid Dynamics*, vol. 3, pp. 15–42, 1991. DOI: 10.1007/BF00271514.

[114] B. Barker, M. A. Johnson, P. Noble, L. M. Rodrigues, and K. Zumbrun, "Nonlinear modulational stability of periodic traveling-wave solutions of the generalized Kuramoto–Sivashinsky equation," *Physica D*, vol. 258, pp. 11–46, 2013. DOI: 10.1016/j.physd.2013.04.011.

[115] P. Cvitanović, R. L. Davidchack, and E. Siminos, "On the state space geometry of the Kuramoto–Sivashinsky flow in a periodic domain," *SIAM J. Appl. Dyn. Syst.*, vol. 9, pp. 1–33, 2010. DOI: 10.1137/070705623.

[116] A. Kalogirou, E. E. Keaveny, and D. T. Papageorgiou, "An in-depth numerical study of the two-dimensional Kuramoto–Sivashinsky equation," *Proc. R. Soc. A*, vol. 471, p. 20 140 932, 2015. DOI: 10.1098/rspa.2014.0932.

[117] G. Ahlers, D. S. Cannell, M. A. Dominguez-Lerma, and R. Heinrichs, "Wavenumber selection and Eckhaus instability in Couette–Taylor flow," *Physica D*, vol. 23, pp. 202–219, 1986. DOI: 10.1016/0167-2789(86)90129-6.

[118] L. Qiao, Z. Zheng, and M. C. Cross, "Minimum-action paths for wave-number selection in nonequilibrium systems," *Phys. Rev. E*, vol. 93, p. 042 204, 2016. DOI: 10.1103/PhysRevE.93.042204.

[119] T. Kapitula and K. Promislow, *Spectral and Dynamical Stability of Nonlinear Waves* (Applied Mathematical Sciences). Springer, 2013, vol. 457. DOI: 10.1007/978-1-4614-6995-7.

[120] A. Demirkaya, T. Kapitula, P. Kevrekidis, M. Stanislavova, and A. Stefanov, "On the spectral stability of kinks in some-symmetric variants of the classical Klein–Gordon field theories," *Stud. Appl. Math.*, vol. 133, pp. 298–317, 2014. DOI: 10.1111/sapm.12053.

[121] C. R. Harris, K. J. Millman, S. J. van der Walt, *et al.*, "Array programming with NumPy," *Nature*, vol. 585, pp. 357–362, 2020. DOI: 10.1038/s41586-020-2649-2.

[122] J. P. Boyd and S. E. Haupt, "Polycnoidal waves: Spatially periodic generalizations of multiple solitons," in *Nonlinear Topics in Ocean Physics*, A. R. Osborne, Ed., Amsterdam: Elsevier, 1991, pp. 827–856.

[123] S. E. Haupt and J. P. Boyd, "Double cnoidal waves of the Korteweg–de Vries equation: A boundary value approach," *Physica D*, vol. 50, pp. 117–134, 1991. DOI: 10.1016/0167-2789(91)90084-M.

[124] Z. Yu and I. C. Christov, "Delayed Hopf bifurcation and control of a ferrofluid interface via a time-dependent magnetic field," *Phys. Rev. E*, vol. 107, p. 055 102, 2023. DOI: 10.1103/PhysRevE.107.055102.

[125] P. Virtanen, R. Gommers, T. E. Oliphant, *et al.*, "SciPy 1.0: fundamental algorithms for scientific computing in Python," *Nat. Methods*, vol. 17, pp. 261–272, 2020. DOI: 10.1038/s41592-019-0686-2.

[126] Y. A. Kuznetsov, *Elements of Applied Bifurcation Theory* (Applied Mathematical Sciences), 3rd ed. New York, NY: Springer, 1998, vol. 112. DOI: 10.1007/978-1-4757-3978-7.

[127] S. Wiggins, *Introduction to Applied Nonlinear Dynamical Systems and Chaos* (Texts in Applied Mathematics). New York, NY: Springer, 2003, vol. 2. DOI: 10.1007/b97481.

[128] G. Tryggvason and H. Aref, "Numerical experiments on Hele Shaw flow with a sharp interface," *J. Fluid Mech.*, vol. 136, pp. 1–30, 1983. DOI: 10.1017/S0022112083002037.

[129] S. M. Baer, T. Erneux, and J. Rinzel, "The slow passage through a Hopf bifurcation: Delay, memory effects, and resonance," *SIAM J. Appl. Math.*, vol. 49, pp. 55–71, 1989. DOI: 10.1137/0149003.

[130] C. Lobry, "Dynamic bifurcations," in *Dynamic Bifurcations*, E. Benoît, Ed., Berlin, Heidelberg: Springer Berlin Heidelberg, 1991, pp. 1–13.

[131] L. D. Landau, "On the problem of turbulence," *Dokl. Akad. Nauk SSSR*, vol. 44, pp. 339–342, 1944, in Russian.

[132] E. W. Weisstein, *Erfi*, MathWorld–A Wolfram Web Resource, 2022. [Online]. Available: https://mathworld.wolfram.com/Erfi.html.

[133] G. I. Taylor, *Low Reynolds Number Flows*, National Committee for Fluid Mechanics Films, Education Development Center, Inc. Newton, MA, 1967. [Online]. Available: http://web.mit.edu/hml/ncfmf.html.

[134] J.-C. Bacri and D. Salin, "First-order transition in the instability of a magnetic fluid interface," *J. Physique Lett.*, vol. 45, pp. 559–564, 1984. DOI: 10.1051/jphyslet:019840045011055900.

[135] I. Seric, S. Afkhami, and L. Kondic, "Interfacial instability of thin ferrofluid films under a magnetic field," *J. Fluid Mech.*, vol. 755, R1, 2014. DOI: 10.1017/jfm.2014.435.

[136] J. S. Dahler, L. E. Scriven, and M. J. Lighthill, "Theory of structured continua I. General consideration of angular momentum and polarization," *Proc. R. Soc. Lond. A.*, vol. 275, pp. 504–527, 1963. DOI: 10.1098/rspa.1963.0183.

[137] H. Brenner, "Rheology of two-phase systems," *Ann. Rev. Fluid Mech.*, vol. 2, pp. 137–176, 1970. DOI: 10.1146/annurev.fl.02.010170.001033.

[138] D. W. Condiff and J. S. Dahler, "Fluid mechanical aspects of antisymmetric stress," *Phys. Fluids*, vol. 7, pp. 842–854, 1964. DOI: 10.1063/1.1711295.

[139] A. Ramachandran, "A macrotransport equation for the particle distribution in the flow of a concentrated, non-colloidal suspension through a circular tube," *J. Fluid Mech.*, vol. 734, pp. 219–252, 2013. DOI: 10.1017/jfm.2013.455.

[140] W. Yang and B. Liu, "Effects of magnetization relaxation in ferrofluid film flows under a uniform magnetic field," *Phys. Fluids*, vol. 32, p. 062 003, 2020. DOI: 10.1063/5.0011655.

[141] M. I. Shliomis, "Magnetic fluids," *Sov. Phys. Usp.*, vol. 17, pp. 153–169, 1974. DOI: 10.1070/PU1974v017n02ABEH004332.

[142] A. Oron, S. H. Davis, and S. G. Bankoff, "Long-scale evolution of thin liquid films," *Rev. Mod. Phys.*, vol. 69, pp. 931–980, 1997. DOI: 10.1103/RevModPhys.69.931.

[143] L. Kondic, "Instabilities in gravity driven flow of thin fluid films," *SIAM Rev.*, vol. 45, pp. 95–115, 2003. DOI: 10.1137/S003614450240135.

[144] D. Laroze, P. Siddheshwar, and H. Pleiner, "Chaotic convection in a ferrofluid," *Commun. Nonlinear Sci. Numer. Simulat.*, vol. 18, pp. 2436–2447, 2013. DOI: 10.1016/j.cnsns.2013.01.016.

[145] F. Boyer and E. Falcon, "Wave turbulence on the surface of a ferrofluid in a magnetic field," *Phys. Rev. Lett.*, vol. 101, p. 244 502, 2008. DOI: 10.1103/PhysRevE.83.046303.

[146] K. R. Schumacher, J. J. Riley, and B. A. Finlayson, "Turbulence in ferrofluids in channel flow with steady and oscillating magnetic fields," *Phys. Rev. E*, vol. 83, p. 016 307, 2011. DOI: 10.1103/PhysRevE.83.016307.

[147] S. Altmeyer, Y. Do, and Y.-C. Lai, "Transition to turbulence in Taylor-Couette ferrofluidic flow," *Sci. Rep.*, vol. 5, p. 10 781, 2015. DOI: 10.1038/srep10781.

[148] H. Gotoda, M. Pradas, and S. Kalliadasis, "Nonlinear forecasting of the generalized Kuramoto–Sivashinsky equation," *Int. J. Bifurcation Chaos*, vol. 25, p. 1 530 015, 2015. DOI: 10.1142/S0218127415300153.

[149] G. Cui and I. Jacobi, "Magnetic control of ferrofluid droplet adhesion in shear flow and on inclined surfaces," *Langmuir*, vol. 36, pp. 10 885–10 891, 2020. DOI: 10.1021/acs.langmuir.0c02369.

[150] D. E. Moulton and J. A. Pelesko, "Reverse draining of a magnetic soap film," *Phys. Rev. E*, vol. 81, p. 046 320, 2010. DOI: 10.1103/PhysRevE.81.046320.

[151] D. T. Conroy and O. K. Matar, "Thin viscous ferrofluid film in a magnetic field," *Phys. Fluids*, vol. 27, p. 092 102, 2015. DOI: 10.1063/1.4930010.

[152] J. R. Howse, R. A. Jones, A. J. Ryan, T. Gough, R. Vafabakhsh, and R. Golestanian, "Self-motile colloidal particles: From directed propulsion to random walk," *Phys. Rev. Lett.*, vol. 99, p. 048 102, 2007. DOI: 10.1103/PhysRevLett.99.048102.

[153] J. Palacci, C. Cottin-Bizonne, C. Ybert, and L. Bocquet, "Sedimentation and effective temperature of active colloidal suspensions," *Phys. Rev. Lett.*, vol. 105, p. 088 304, 2010. DOI: 10.1103/PhysRevLett.105.088304.

[154] H. Karani, G. E. Pradillo, and P. M. Vlahovska, "Tuning the random walk of active colloids: From individual run-and-tumble to dynamic clustering," *Phys. Rev. Lett.*, vol. 123, p. 208 002, 2019. DOI: 10.1103/PhysRevLett.123.208002.

[155] C. J. Reeves, I. S. Aranson, and P. M. Vlahovska, "Emergence of lanes and turbulent-like motion in active spinner fluid," *Commun. Phys.*, vol. 4, p. 92, 2021. DOI: 10.1038/s42005-021-00596-2.

[156] S. Zhou, A. Sokolov, O. D. Lavrentovich, and I. S. Aranson, "Living liquid crystals," *Proc. Natl Acad. Sci. USA*, vol. 111, pp. 1265–1270, 2014. DOI: 10.1073/pnas.1321926111.

[157] M. M. Genkin, A. Sokolov, O. D. Lavrentovich, and I. S. Aranson, "Topological defects in a living nematic ensnare swimming bacteria," *Phys. Rev. X*, vol. 7, p. 011 029, 2017. DOI: 10.1103/PhysRevX.7.011029.

VITA

Education

Purdue University, West Lafayette **Aug. 2017 – Aug. 2023**

Ph.D. in Mechanical Engineering

Huazhong University of Science and Technology, China **Sept. 2013 – Jun. 2017**

B.S. in Naval Architecture and Ocean Engineering

Publications resulting from this thesis

Zongxin Yu, and Ivan C. Christov. "Delayed Hopf bifurcation and control of a ferrofluid interface via a time-dependent magnetic field." *Physical Review E* 107(5) (2021) 055102, doi:10.1103/PhysRevE.107.055102.

Ivan C. Christov and **Zongxin Yu**, "Twenty-Five Years of Dissipative Solitons." Submitted to *the proceedings of the 13th Conference of the Euro-American Consortium for Promoting the Application of Mathematics in Technical and Natural Sciences* (2021). doi:10.1063/5.0100781.

Zongxin Yu, and Ivan C. Christov. "Long-wave equation for a confined ferrofluid interface: Periodic interfacial waves as dissipative solitons." *Proceedings of the Royal Society A* 477 (2021) 20210550, doi:10.1098/rspa.2021.0550.

Zongxin Yu, and Ivan C. Christov. "Tuning a magnetic field to generate spinning ferrofluid droplets with controllable speed via nonlinear periodic interfacial waves." *Physical Review E* 103(1) (2021) 013103, doi:10.1103/PhysRevE.103.013103.

Conference presentations resulting from this thesis

Zongxin Yu and Ivan C. Christov, "Delayed Hopf bifurcation and control of a ferrofluid droplet with a time-varying magnetic field." DS23, *SIAM Conference on Applications of Dynamical System* (2023).

Zongxin Yu and Ivan C. Christov, "Delayed Hopf bifurcation of a ferrofluid interface subject to a time-dependent magnetic field." The 75$^{\text{th}}$ APS Division of Fluid Dynamics Annual Meeting, *Bulletin of the American Physical Society* (2022).

Zongxin Yu and Ivan C. Christov, "Nonlinear periodic waves on ferrofluid interfaces." The 74$^{\text{th}}$ APS Division of Fluid Dynamics Annual Meeting, *Bulletin of the American Physical Society* (2021).

Zongxin Yu and Ivan C. Christov, "Nonlinear periodic waves on ferrofluid droplet and film interfaces." DS21, *SIAM Conference on Applications of Dynamical System* (2021).

Zongxin Yu and Ivan C. Christov, "Nonlinear traveling waves on the interface of a ferrofluid droplet subjected to magnetic field." APS March Meeting, *Bulletin of the American Physical Society* (2021).